Inaugural dissertation
for
obtaining the doctoral degree
of the
Combined Faculty of Mathematics, Engineering
and Natural Sciences
of the
Ruprecht - Karls - University
Heidelberg

Presented by

M.Sc. Federica Fiorentino

born in: Naples

Oral examination: 19.10.2022

Structural and biochemical analysis of the human Rea1-Rsa4 pre-ribosomal complex enables the identification of small molecule inhibitors that impair human cancer cell growth

Referees: Prof. Dr. Ed Hurt

Prof. Dr. Irmgard Sinning

NOMENCLATURE AND ABBREVIATION

CP central protuberance
Cryo-EM cryogenic electron microscopy
C-terminal carboxy-terminal
Ct prefix used to denote *Chaetomium thermophilum* origin
ETS external transcribed spacer
FLAG octapeptide epitope (DYKDDDDK) used as bait in purifications
GFP green fluorescent protein
h hour
HEK293 cell line derived from human embryonic kidney
ITS internal transcribed spacer
kDa kilo-Daltons
kb kilo-bases
LFQ label-free quantification
Mdm2 Mouse Double Minute 2 (E3 ubiquitin-protein ligase)
MS mass spectrometry
NPC nuclear pore complex
N-terminal amino terminal
OD600 optical density of a cell suspension at 600 nm wavelength
PCR polymerase chain reaction
PDB code protein data bank identification
PET polypeptide exit tunnel
Pol I Polymerase I
Pol II Polymerase II
Pol III Polymerase III
pre-60S precursor of the large 60S ribosomal subunit
pre-40S precursor of the small 40S ribosomal subunit
PTC peptidyl transferase center
rDNA ribosomal deoxyribonucleic acid
r-proteins ribosomal proteins
rRNA(s) ribosomal ribonucleic acid(s)
RT room temperature
Sc prefix used to denote *Saccharomyces cerevisiae* origin
SDS-PAGE sodium dodecyl sulfate-polyacrylamide gel electrophoresis
SEC size-exclusion chromatography
SQ-MS semi-quantitative mass spectrometry
tRNA transfer ribonucleic acid
uL5/Rpl11 universal L-protein 5 / Ribosomal Protein of the Large subunit, 11
uL18/Rpl5 universal L-protein 18 / Ribosomal Protein of the Large subunit, 5
WB Western blot
YFP yellow fluorescent protein

Summary

Ribosomes are evolutionary-conserved molecular machines consisting of the large 60S and the small 40S subunits, which follow separate assembly routes but later function together as mature 80S ribosomes during translation. During ribosome biogenesis the pre-60S subunit goes through many maturation steps that require numerous assembly factors. One of them, the AAA^+ ATPase Rea1 mediates two crucial remodelling steps in the nucleolus and the nucleoplasm, respectively, by binding via its MIDAS domain to the UBL domains of either Ytm1 (WDR12 in humans) or Rsa4 (NLE1 in humans). These interactions, which are similar to a typical integrin-ligand binding mechanism, are essential for cell growth, and their abolishment confers a lethal phenotype in yeast. Loss-of-function mutations of ribosomal proteins can lead to diseases called Ribosomopathies and growth factors and mitogenic stimuli can alter oncogenic signalling pathways by hyper-activating the tightly regulated ribosome biogenesis process, which, recently, has become a cancer therapy target. Therefore, analyzing the human ribosome assembly pathway might help find small chemical compounds impairing ribosome synthesis at specific maturation stages, which could be exploited for analytical and therapeutic purposes.

During my PhD, I could reconstitute the interaction between human homologs of Rea1-MIDAS and Rsa4-UBL domains *in vitro* and crystallize this heterodimer. Using a dominant-negative rsa4 mutant, mapping the amino acid 85 of the UBL domain, I could impair this interaction, which allowed me to evaluate the effects of the loss of Rea1-MIDAS-Rsa4-UBL binding *in vitro* and human culture cells. I successfully crystallized the complex, obtaining the atomic model of the MIDAS-UBL interaction, a central finding supporting the search for small chemical compounds impairing the human Rea1-MIDAS-Rsa4-UBL interaction. Eventually, we could find one inhibitor, which I tested *in vitro* and human cancer cells. In addition, using the dominant-negative phenotype generated by the rsa4-UBL mutant in human cells, we successfully isolated a human pre-60S ribosomal particle and visualized it by cryo-electron microscopy.

Thus, my thesis provided structural and functional insights into the Rea1-MIDAS–Rsa4-UBL interaction in the human system, confirming its importance for human pre-60S ribosome assembly and cell viability. These findings may allow further optimization of small chemical compounds to efficiently inhibit human ribosome biogenesis in cancer cells, alone or in combination with other known cancer drugs.

ZUSAMMENFASSUNG

Ribosomen sind evolutionär konservierte molekulare Maschinen, die aus der großen 60S- und der kleinen 40S-Untereinheit bestehen und separate Reifungsprozesse durchlaufen. Die reifen Untereinheiten bilden im Zellplasma die 80S-Ribosomen, die für die Translation benötigt werden. Für die Reifung der 60S-Untereinheit sind viele Reifungs- und Umbauprozesse notwendig, die zahlreiche Biogenesefaktoren erfordern. Die AAA+ ATPase Rea1 ist dabei für zwei entscheidende Umbauschritte im Nukleolus bzw. im Nukleoplasma notwendig, wo sie mit ihrer MIDAS-Domäne an die UBL-Domäne von Ytm1 (WDR12 beim Menschen) bzw. an die UBL-Domäne von Rsa4 (NLE1 beim Menschen) bindet. Diese Wechselwirkungen, die einer typischen Integrin-Liganden-Bindung ähneln, sind für das Zellwachstum entscheidend, wie sich anhand eines lethalen Phänotyps beobachten lässt wenn diese Interaktionen gestört werden. Da die Ribosomenbiogenese ein streng regulierter Prozess ist, können Wachstumsfaktoren und mitogene Stimuli onkogene Signalwege verändern und die Ribosomenbiogenese hyperaktivieren. Deshalb ist die Ribosomenbiogenese zu einem Ziel der Krebstherapie geworden. Die Analyse der Ribosomenbiogenese beim Menschen könnte helfen kleine chemische Verbindungen zu finden, die die Ribosomenbildung in bestimmten Reifungsstadien beeinträchtigen und für analytische und therapeutische Zwecke eingesetzt werden könnten.

Während meiner Promotion habe ich die Interaktion zwischen den humanen Biogenesefaktoren Rea1 (MIDAS) und Rsa4 (UBL) in vitro rekonstituiert und den Heterodimer kristallisiert. Unter Verwendung einer dominant-negativen Rsa4-Mutante, in welcher die Aminosäure 85 der UBL-Domäne mutiert wurde, konnte ich diese Wechselwirkung beeinträchtigen. Dadurch konnte ich die Auswirkungen einer fehlenden Interaktion zwischen Rea1-MIDAS und Rsa4-UBL in vitro und in Säugetierzellkulturen bewerten. Die erfolgreiche Kristallisation des Komplexes, die das atomare Modell der MIDAS-UBL-Wechselwirkung zeigt, war eine zentrale Erkenntnis für die Suche nach kleinen chemischen Verbindungen, die den menschlichen Rea1-MIDAS-Rsa4-UBL-Komplex beeinträchtigen. Mit Hilfe des Modells konnten wir einen Inhibitor finden, den ich in vitro und in menschlichen Krebszellen getestet habe. Darüber hinaus konnten wir unter Verwendung des dominanten Phänotyps, der von der Rsa4-UBL-Mutante in menschlichen Zellen erzeugt wurde, menschliche prä-60S-ribosomale Partikel isolieren und deren Strukturen mittels Cryo-EM lösen.

Somit lieferte meine Dissertation strukturelle und funktionelle Einblicke in die Funktionsweise der Rea1-MIDAS - Rsa4-UBL-Wechselwirkung im menschlichen System und bestätigte ihre Bedeutung für die menschliche 60S-Ribosomenbiogenese sowie für die Lebensfähigkeit

menschlicher Zellen. Die gewonnenen Erkenntnisse könnten zur weiteren Optimierung von chemischen Verbindungen herangezogen werden, die für die Unterdrückung von Krebszellen im Menschen eingesetzt werden könnten

1 Introduction

1.1 The mature eukaryotic ribosome: an intricate nanomachine

Ribosomes are essential cellular nanomachines made of proteins and RNAs and are found across all kingdoms of life. Ribosomes mediate the protein synthesis by decoding the messenger RNA (mRNA) and catalyzing the peptide bond formation between amino acids, which are specified by the triplet codons in sequential order, thus leading to the synthesis of polypeptide chains. This process, known as translation, is well-regulated and occurs with an error rate of only one codon out of 1000–10,000. This very high translation fidelity is required to sustain life (*Parker, 1989; Ogle and Ramakrishnan, 2005*).

The first pioneering works on determining the three-dimensional structures of ribosomes were carried out by A. Yonath, T.A. Steitz, and V. Ramakrishnan, which were awarded the Nobel prize in 2009 for their characterization of the bacterial ribosomes *(Ban et al., 2000) (Schluenzen et al., 2000; Wimberly et al., 2000)*. Those studies opened the door for future structural characterizations of ribosomes in other organisms, indeed, later, in 2011, the x-ray structure of the mature ribosome (80S) of *Saccharomyces cerevisiae* was determined at 3.0-Å resolution (**Fig. 1**, PDB code: 4V88) (*Ben-Shem et al., 2011*).

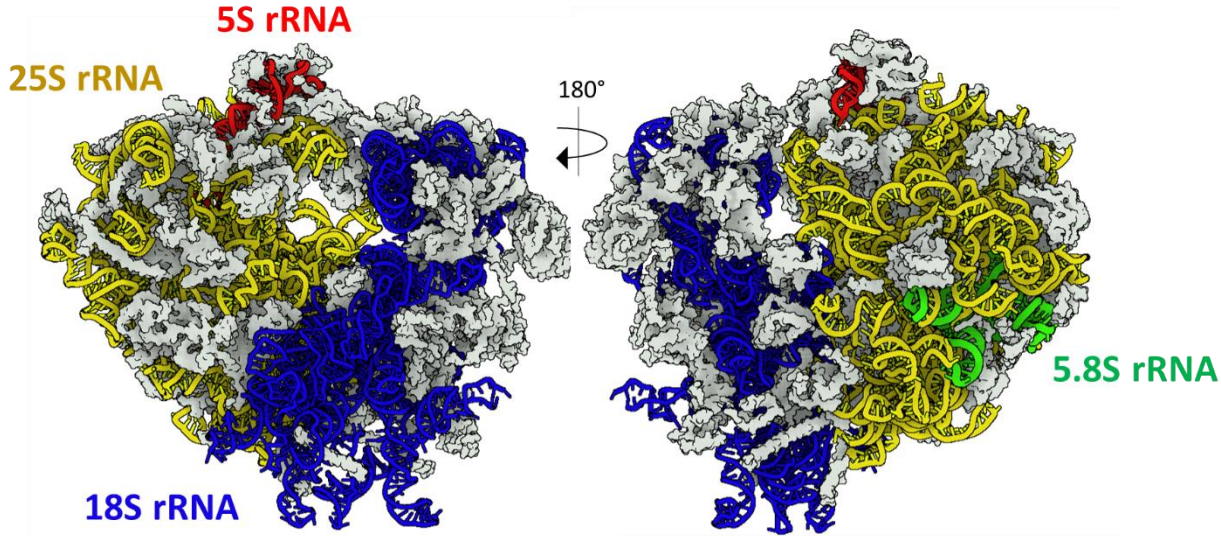

Figure 1. Crystal structure of the 80S mature ribosome of *S. cerevisiae.*
Front and back views of the 80S ribosome structure from *S. cerevisiae* with ribosomal proteins in grey, 25S rRNA in yellow, 18S rRNA in blue, 5S rRNA in red, and 5.8S rRNA in green. PDB code: 4V88.

The x-ray structures and cryogenic electron microscopy (cryo-EM) of the yeast ribosome and of different organisms *(Yusupov et al., 2001 ; Armache et al., 2010; Shem et al.,2011; Anger et al., 2013; Ben- Khatter et al., 2015*) have provided details on the structural organization of the ribosomal RNAs (rRNAs) and ribosomal proteins (RPs) within the ribosomes. Moreover, these studies also shed light on the structure of the conserved functional sites necessary for the synthesis of polypeptides **(Fig. 2),** such as the A-site, allocating the tRNAs that are loaded with the corresponding amino acid (aminoacyl-tRNAs), the P-site binding to the tRNAs attached to the growing polypeptide chain, and the E-site, from which the unloaded tRNAs are released.

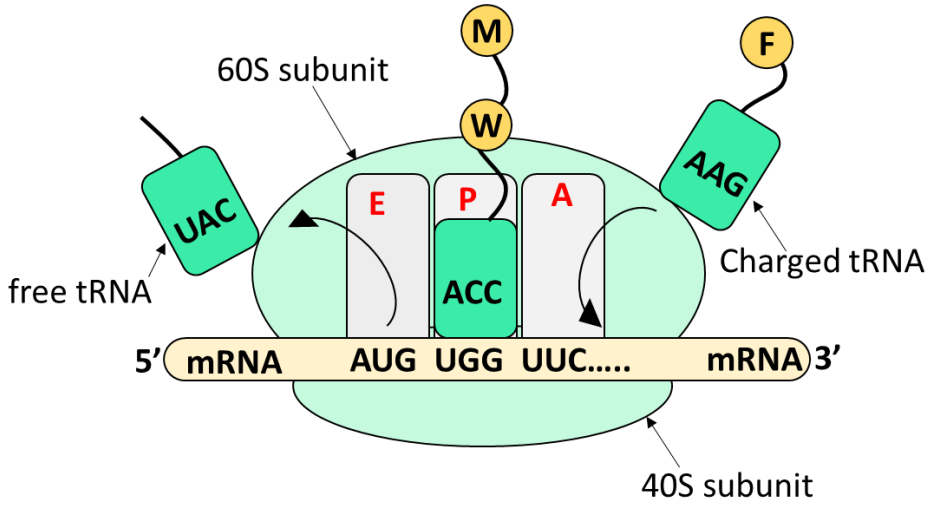

Figure 2. Schematic representation of the ribosomal functional sites (A-P and E).
The A site binds an amino acid-charged tRNA bearing the anticodon corresponding to the correct mRNA codon, the P site binds a charged tRNA still carrying the amino acid that has formed a peptide bond with the growing polypeptide chain, and the E site releases free tRNAs. The ribosome shifts one codon at a time and with each step, a charged tRNA enters the complex, the polypeptide becomes one amino acid longer, and an uncharged tRNA leaves the ribosome.

The mature eukaryotic ribosome (80S) is composed of two unequal subunits, the small 40S subunit and the large 60S subunit, differing in RNAs and protein composition. The 40S subunit consists of the 18S rRNA and 33 ribosomal proteins and shows distinctive structural features known as the body, platform, head, beak, and shoulder **(Fig. 3A)**. The 40S binds the mRNA and contains the decoding center, where the codon and the tRNA anticodon are paired (*Melnikov et al., 2012; Yusupova and Yusupov, 2014)*. The yeast 60S subunit contains the 25S, 5.8S, 5S rRNAs, and 46 ribosomal proteins (28S, 5.8S, 5S rRNA, and 47 ribosomal proteins in humans) and is characterized by distinctive structural features, such as the central protuberance (CP), L1-stalk, and the P-stalk (or acidic stalk) (**Fig. 3B**). It further contains the peptidyl transferase center

(PTC), which catalyzes the peptide bond formation among amino acids, and the polypeptide exit tunnel (PET), through which the nascent polypeptide chain exits the ribosome (**Fig. 3B**) (*Bashan and Yonath, 2008; Melnikov et al., 2012; Yusupova and Yusupov, 2014*).

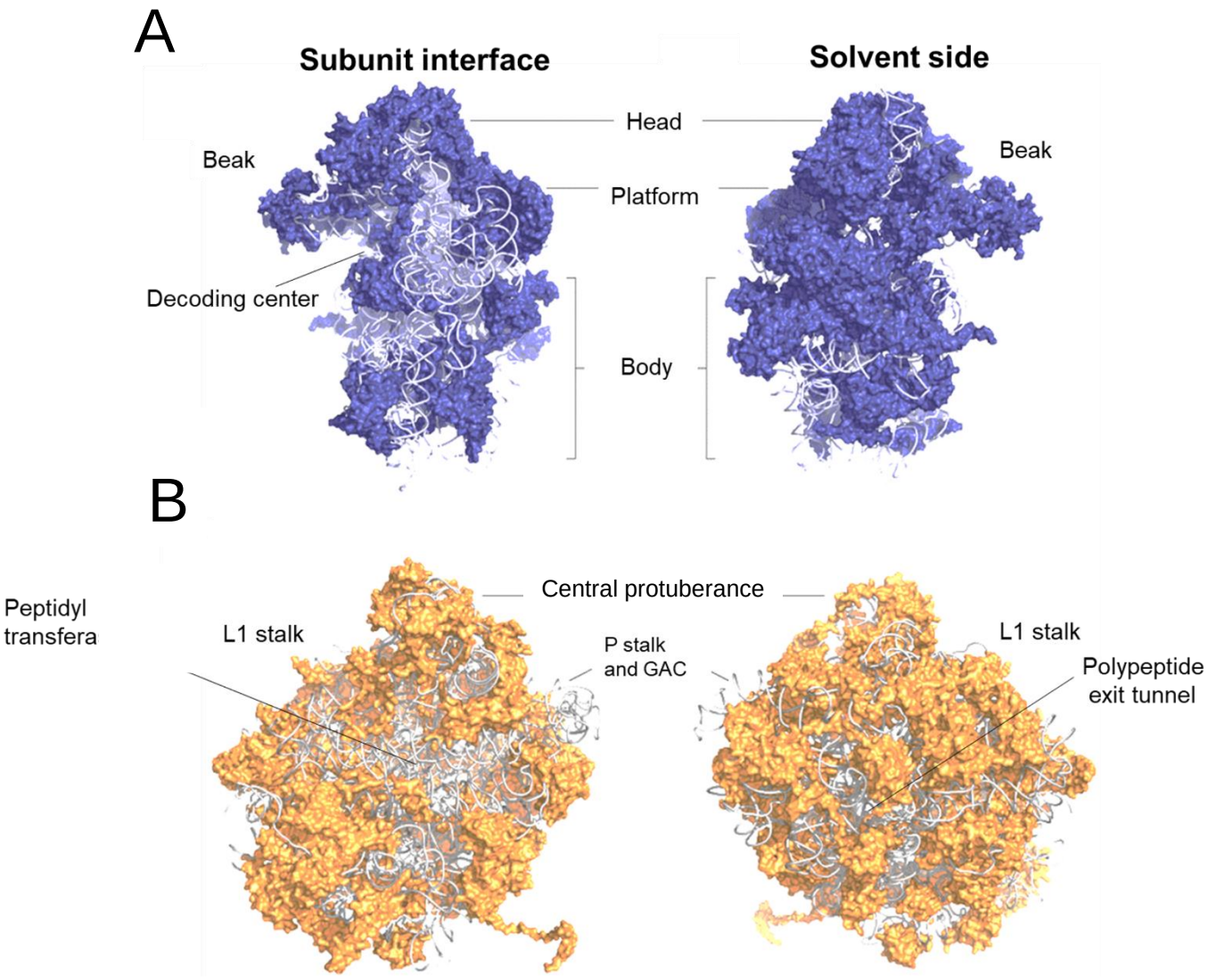

Figure 3. Structural representation of the small 40S and large 60 subunits of the eukaryotic ribosome. A) Two opposite views of the of the 40S subunit: on the left is shown the subunit interface, which is the side of the 40S that interacts with the 60S subunit in the mature ribosome, and on the right is shown the solvent side, that makes contacts with the solvent. The 40S subunit contains rRNA in grey and ribosomal proteins in dark blue. The beak, body, head, platform, and shoulder are indicated as distinctive structural features of the 40S subunit. The decoding center is located on the subunit interface, as specified. **B**) Two opposite views of the 60S subunit: on the left the subunit interface and on the right the solvent side of the 60S subunit are shown. The 60S subunit contains rRNAs depicted in light grey and ribosomal proteins in orange. The distinctive structural features of the 60S subunit, such as the L1 stalk, the central protuberance (CP), the acidic stalk or P stalk together with the GAC (GTPase-Associated Center) are labelled. The peptidyl transferase center (PTC) are indicated at the interface side of the 60S subunit, while the polypeptide exit tunnel (PET) is located at the solvent side PDB code: 4V88. Figure adapted from *de la Cruz et al., 2015*.

1.2 The assembly pathway of the eukaryotic ribosome

Ribosome biogenesis is one of the most energy-consuming pathways and is essential to maintaining cell growth. Indeed, in *S. cerevisiae*, more than 2000 ribosomes are generated every minute, a process that needs impressive amounts of resources and the activity of all three RNA polymerases (Pol I, II, III) (*Warner, 1999*). Ribosome assembly relies on the synthesis and maturation of the rRNAs, the removal of assembly factors and the hierarchical recruitment of the ribosomal proteins (r-proteins) occurring within a series of precursor ribosomal particles, or pre-ribosomes within the nucleolus, nucleoplasm and cytoplasm **(Fig. 4)**. A plethora of assembly factors, more than 200 orchestrate this process, and among them are several energy-consuming enzymes, like endonucleases, exonucleases, methyltransferases, six GTPases, three AAA^+ ATPases, nineteen DExD/H-Box ATP-dependent RNA helicases, three kinases, and two ABC proteins. By contrast, other additional factors have no enzymatic activity but have other domains that allow them to bind rRNA providing a protein-protein interaction platform to chaperone the ribosome assembly (*Fromont-Racine et al., 2003; Henras et al., 2008; Kressler et al., 2010*).

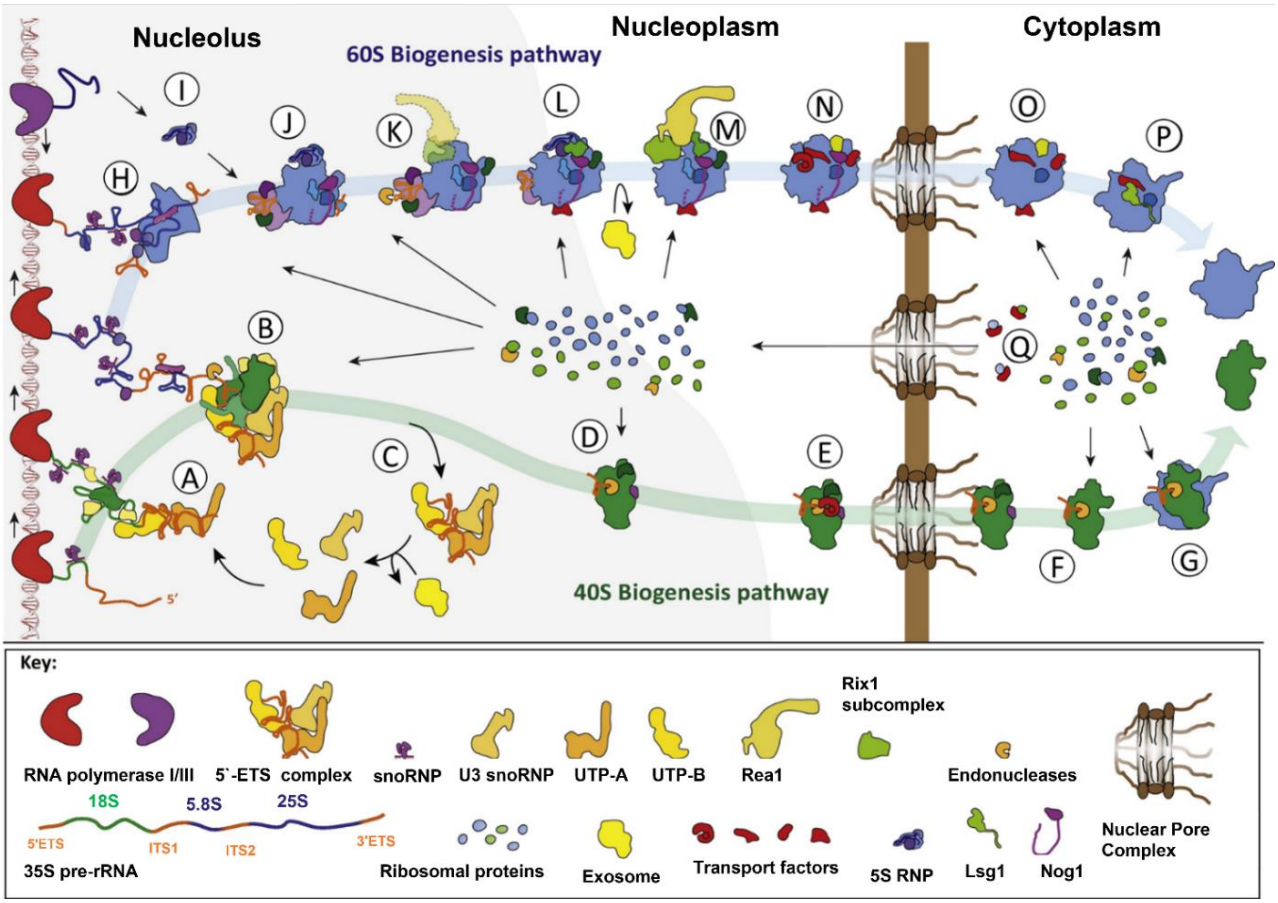

Figure 4. Overview of the major steps in the 40S and 60S ribosome biogenesis pathways in yeast. Ribosome biogenesis starts in the nucleolus with the transcription of the 35S unique transcript, which is performed by the RNA polymerase I (on the left side, in red). Note that the 5S is transcribed separately by the RNA polymerase III (on the left side, in violet). Ribosome biogenesis is a multicompartment process whose intermediates transit from the nucleolus to the nucleus, and then are exported through the nuclear pore complex into the cytoplasm, where finally the 40S and 60S subunits reach their mature configurations. The lower pathway in green leads to the maturation of the 40S subunit and its intermediates. The upper pathway in blue leads to the maturation of the 60S subunit and its intermediates from H to P are indicated. The ribosomal proteins and assembly factors that are synthesized in the cytoplasm and imported in the nucleus are indicated (Q). Figure adapted from Kressler et al., 2017.

1.2.1 Ribosome biogenesis starts in the nucleolus with the synthesis of ribosomal RNAs

The initial phase of ribosome assembly occurs in the nucleolus, where the RNA polymerase I transcribes the head-to-tail tandem repeats that contain the ribosomal genes and are present within the ribosomal DNA (rDNA) (*Mélèse and Xue, 1995*). The transcription of ribosomal genes by the RNA polymerase I occurs at a rate of 40-60 nucleotides per second (*French et al., 2003*; *Koš and Tollervey, 2010*) and produces a primary polycistronic rRNA transcript called 35S pre-rRNA in yeast (or 47S in humans), which is the precursor of the mature 18S, 5.8S and 25S rRNAs in yeast (or 18S, 5.8S and 28S in humans). Within the polycistronic rRNA transcript, the 18S, 5.8S, and 25S rRNA sequences are separated by the internal transcribed spacers 1 (ITS1) and 2 (ITS2) and flanked by the 5′ and 3′ external transcribed spacers (5′-ETS and 3′-ETS) **(Fig. 5)**. The sequential removal of externally and internally transcribed spacer sequences, mediated by endonucleases and exonucleases, ensure the final maturation of 35S pre-rRNA (*Henras et al., 2015*). A distinct gene in the rDNA repeat encodes for the 5S rRNA, transcribed by the RNA polymerase III in the reverse direction from the opposite ribosomal DNA strand **(Fig. 5)**. While rRNAs are transcribed by RNA polymerase I or III, ribosomal proteins and assembly factors are transcribed by the RNA polymerase II, synthesized in the cytoplasm, and imported into the nucleolus, where they are hierarchically incorporated into the maturating ribosomes during the ribosome assembly process (*Warner, 1999; Velculescu et al., 1997*).

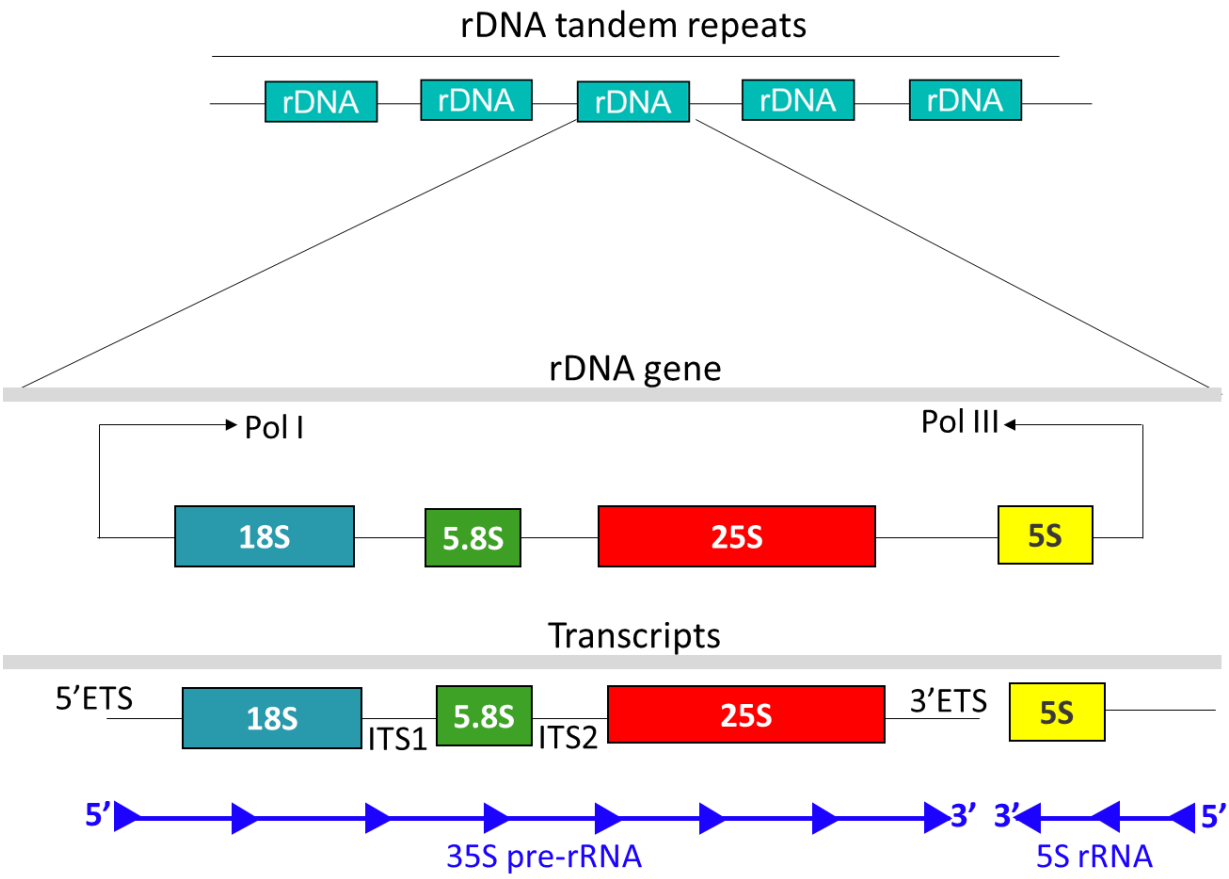

Figure 5. Schematic representation of the transcription from rDNA repeats in yeast.
rDNA genes are arranged in tandem repetitive units (~200 repeated units). Each rDNA repeat bears four rRNAs sequences encoding for the 18S, 5.8S, 25S rRNAs, and 5S. The RNA polymerase I transcribes a single polycistronic transcript (35S pre-rRNA) containing the 18S, 5.8S and 25S, while the RNA polymerase III transcribes the 5S rRNA, as indicated below. Note that the blue lines specify transcription direction.

1.2.2 The assembly pathway of the 40S subunit

The assembly process of the 40S and 60S subunits (reviewed in *Kressler et al., 2017; Klinge and Woolford, 2019*) starts in the nucleolus. While the 5' end of the polycistronic 35S transcript emerges, the first ribosomal proteins and assembly factors are co-transcriptionally recruited and assembled into the initial 5'-ETS particle **(Fig. 4** step **A)** *(Chaker-Margot et al., 2015*; *Zhang et al., 2016)*. This 5'-ETS particle is formed upon the association with the emerging 5'ETS RNA of the sub-complexes or modules **(Fig. 4** step **C)** UTP-A (Utp4, Utp5, Utp8, Utp9, Utp10, Utp15, and Utp17) (*Gallagher et al., 2004; Pérez-Fernández et al., 2007; Pöll et al., 2014*), UTP-B (Utp1, Utp6, Utp12, Utp13, Utp18, and Utp21) (*Kornprobst et al., 2016; Pérez-Fernández et al., 2007; Pöll*

et al., 2014), and the U3 small nuclear ribonucleoprotein complex (U3 snoRNA, Nop1, Snu13, Nop56, Nop58, and Rrp9) (*Chaker-Margot et al., 2017; Kornprobst et al., 2016; Sun et al., 2017*). The further incorporation of the Mpp10 complex (Mpp10, Imp3, and Imp4 and Sas10) *(Lee et al., 1999; Kornprobst et al., 2016)* and individual assembly factors stabilize the 5'-ETS particle. This particle constitutes an initial architectural scaffold (*Barandun et al., 2018*) on which the first biochemically stable assembly intermediate, termed the small subunit (SSU) processome *(Dragon et al., 2002)* or 90S pre-ribosome *(Grandi et al., 2002*) is then assembled with the further transcription of the 18S RNA and association of other assembly factors **(Fig. 4** step **B)** (*Chaker-Margot et al., 2017*). Among the assembly factors that get incorporated into the 90S particles are the Bms1 module (Bms1 and Rcl1), the Kre33 module (Kre33, Enp2, Brf2, and Lcp5), the UTP-C, (Utp22-Rrp7, Cka1, Cka2, Ckb1, and Ckb2) the Noc4-Nop14 complex, the architectural protein Utp20, the endonuclease Utp24 and several other factors exerting structural and/or enzymatic roles *(Krogan et al., 2004; Perez-Fernandez et al., 2011; Zhang et al., 2016; Kornprobst et al.,2016*)

Eventually, within the 90S pre-ribosome occurs the key co-transcriptional cleavage at the A_1 site, possibly performed by Utp24 (*Wells et al., 2016)*, which separates the 5'-ETS from the 18S rRNA. The 5'-ETS RNA is thought to be degraded by the RNA nuclear exosome, a major 3'-5' exoribonuclease complex (*Thoms et al., 2015; Lau et al., 2021*). Another pivotal cleavage, which can be mainly co-transcriptional (*Koš and Tollervey, 2010; Osheim et al., 2004)*, occurs at the A_2 site that is located within the ITS1 and is crucial to separate the pre-60S and pre-40S assembly pathways **(Fig. 6)** (*Udem and Warner, 1972*).

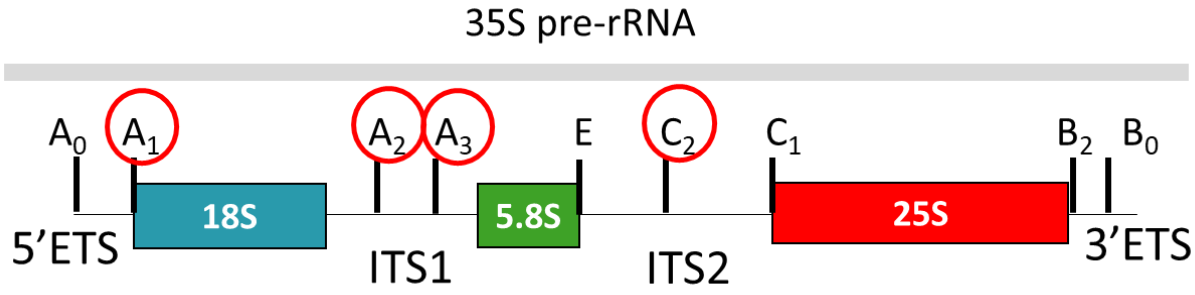

Figure 6. Scheme showing the cleavage sites within the 35S pre-rRNA.
With red circles are indicated the clevage sites that are described in the main text, such as the A_1 site within the 5' ETS (paragraph 1.2.2), A_2 and A_3 sites (paragraph 1.2.3.1) within the ITS1, and C_2 within the ITS2 (paragraph 1.2.3).

The 90S pre-ribosomes, following the degradation of the 5'-ETS RNA and the associated modules (UTP-A and UTP-B) **(Fig. 4** step **C),** evolve to the primordial pre-40S, an early pre-40S intermediate that still contains assembly factors typical of the 90S, among which the RNA helicase Dhr1 that is thought to probably remove the U3 snoRNA (*Cheng et al., 2020*). The small subunit continues to develop in the nucleus **(Fig. 4** steps **D-E)** until exported into the cytoplasm **(Fig. 4** steps **F)**. Among the assembly factors that enable the maturation of the emerging 40S subunit are Ltv1 and Enp1, which bind at the region of the beak, Rrp12, Rio2, Dim1, and Tsr1, which bind at the subunit interface, and Nob1, which binds at the platform (reviewed in *de la Cruz et al. 2015; Schäfer et al. 2003; Strunk et al. 2011*). Additionally, ribosomal proteins such as Rps3 (uS3), Rps15 (uS19), Rps18 (uS13), and Rps19 (eS19) bind the pre-40S at the head-like region. The formation of a head-like structure is required to efficiently export the pre-40S pre-ribosome to the cytoplasm by functioning as a docking domain for the export machinery or shielding the hydrophilic rRNA from the hydrophobic environment of the nuclear pore complex (NPC) channel (*Ferreira-Cerca et al. 2007*). The pre-40S particles exported into the cytoplasm have already acquired some of the typical structural features of the mature 40S, such as the head, body, and platform, and are ready for the last maturation steps.

In the cytoplasm, three major maturation events occur: the beak formation, the translation-like cycle, and the 20S pre-RNA final processing. Enp1 and Ltv1, which are associated with the beak region, form with Rps3 a salt-stable complex blocking the opening of the mRNA entry channel *(Ghalei et al., 2015*). This complex gets at first phosphorylated by the Hrr25 kinase (*Schäfer et al. 2006*), allowing its release from the pre-40S particles (*Ghalei et al., 2015*), while the subsequent dephosphorylation of Rps3 promotes its stable re-incorporation into the pre-40S particles and the formation of the beak region (*Schäfer et al., 2006; Mitterer et al., 2016; B. Pertschy., 2017*). During the very late steps of pre-40S assembly occur a test-driving of its function that is mediated by a GTPase, the eukaryotic translation initiation factor 5B (eIF5B), and the ATPase Fap7. These factors promote the joining of the pre-40S subunit with the 60S subunit, thus forming an 80S-like particle which is used to functionally proofread the pre-40S particle and may get eventually disassembled by the termination factor Rli1 ATPase *(Strunk et al., 2012*) **(Fig. 4** step **G and Fig. 7)**.

The translation-like cycle triggers, within the 80S-like particle, the final processing of the 20S pre-rRNA in 18S rRNA upon cleavage at site D, which is performed by the endonuclease Nob1 (*Lamanna and Karbstein, 2009; Pertschy et al., 2009*) and is probably stimulated by the kinase Rio1 (*Turowski et al., 2014*). After processing of the 20S pre-rRNA in mature 18S rRNA, all the ribosomal proteins have been incorporated and the late assembly factors Nob1 and Pno1 have been removed; thus, the emerging small subunit is ready for translation.

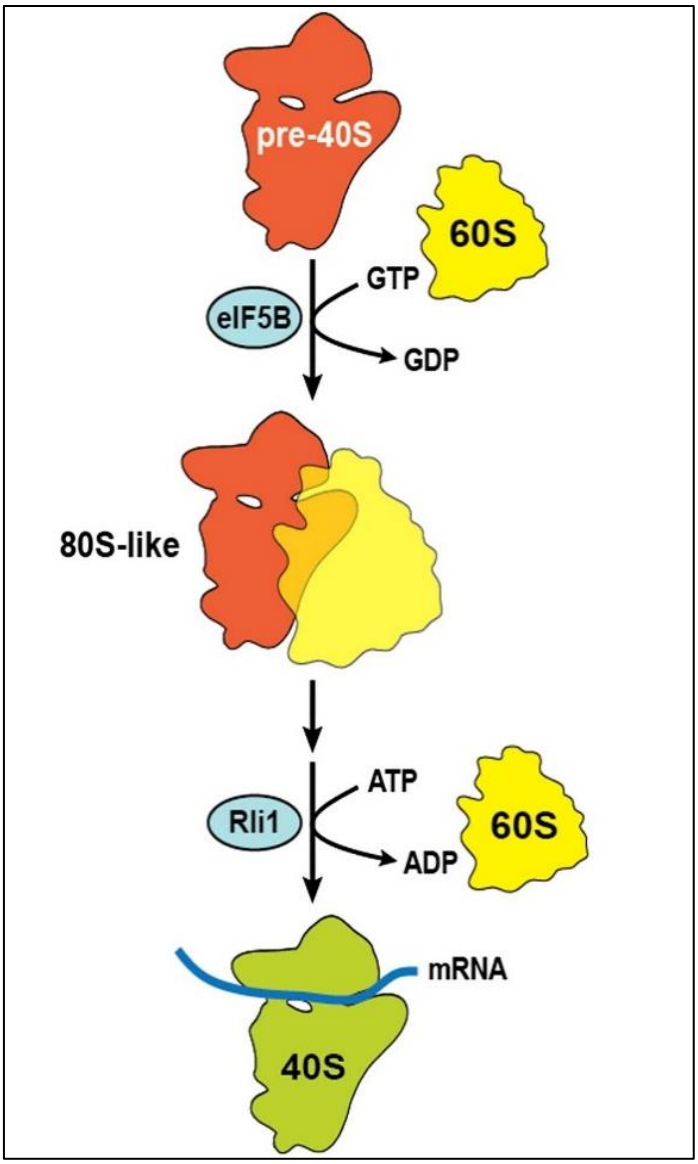

Figure 7. The translation-like cycle is a quality control for the 40S maturing subunit.
The pre-40S maturation involves a translation-like cycle where the translation factor eIF5B, a GTPase, facilitates the coupling of the pre-40S to the 60S subunit, generating the 80S-like particle that performs a translation-like cycle. The 80S-like particle does not contain mRNA or the initiator tRNA during the cycle. Indeed, the translation-like cycle is a final quality control step that serves to assess the ability of the pre-40S subunit to bind to the 60S subunit and translation factors. The termination factor Rli1, an ATPase, finally disassembles the 80S-like particle (*Strunk et al., 2012*).

1.2.3 The assembly pathway of the 60S subunit

1.2.3.1 The nucleolar and nucleoplasmic stages of the 60S ribosome assembly

The small and large subunit biogenesis pathways get separated when the nascent pre-rRNA is cleaved within ITS1 (*Udem and Warner, 1972*). However, the co-transcriptional A_2 cleavage within the ITS1 does not occur right after the transcription of the ITS1 but is delayed until the 5.8S rRNA, ITS2, and the first ~1000 nucleotides of the 25S rRNA) have been transcribed (*Osheim et al., 2004; Koš and Tollervey, 2010; Axt et al., 2014*). Upon A_2 cleavage, a process that may be coordinated by Rrp5 (*Lebaron et al., 2013*), a bridging factor between the small and large pre-ribosome, occurs the formation of the $27SA_2$ pre-rRNA. Meanwhile, the protein Rrp5 detaches from the 90S and stays bound to the early pre-60S, forming a stable subcomplex, i.e.: the Rrp5 Module (Rrp5, Noc1, Noc2) (*Hierlmeier et al., 2013*). These assembly factors, together with the Urb1 module (Urb1, Urb2, Nop8, Dbp6, Rsa3), the $27SA_2$ pre-rRNA, and a series of early acting small nucleolar RNAs (snoRNAs) have been recently identified as distinguishing components of the primordial pre-60S, the so-far earliest known intermediate of the pre-60S assembly pathway *(Ismail et al., 2022).* The $27SA_2$ pre-rRNA is later cleaved at the A_3 site within the ITS1 **(Fig. 6)** by the MRP RNase (*Lindahl et al., 1992; Schmitt and Clayton,1993; Chu et al., 1994; Lygerou et al., 1996;*), and then the exonucleases Rat1, Rrp17 and Xrn1 process the residual sequence of the ITS1 to generate the 27SBS pre-rRNA (*Henry et al., 1994; Oeffinger et al., 2009*). Concomitantly, the rRNA domains are shaped into the developing 60S core in a consecutive order, a hierarchical process which was visualized by cryo-electron microscopy (cryo-EM) *(Kater et al., 2017 Sanghai et al., 2018; Zhou et al., 2019a).* According to the model depicted in **Fig. 8** (*Kater et al., 2017)* the assembly of the pre-60S subunit starts with the formation of the solvent-exposed side that is constructed upon compaction of the 5.8S rRNA, ITS2, and the domains I and II of the 25S rRNA to obtain a stable scaffold for additional assembly. Then, domain VI of the 25S rRNA is also incorporated to form a compact ring-like structure with domains I and II. Further integration of the domains III, IV, and V of the 25S rRNA is then completed in the

nucleus **(Fig. 8).**

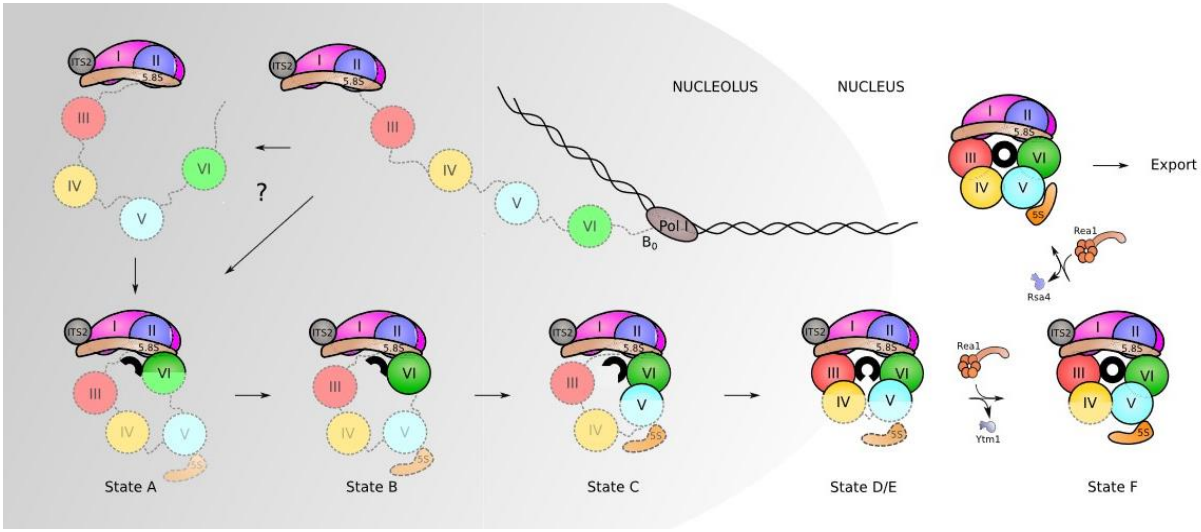

Figure 8. Model showing the sequential integration and compaction of the 60S subunit pre-rRNA domains. The early assembly of the 60S subunit into a growing particle is carried out in a hierarchical fashion, with the consecutive circularization of the pre-rRNA domains to form a tightly packed ring-like structure. The first step in the circularization of the pre-rRNA to form a rigid core structure, is the partial binding of domain VI of the 25S rRNA to the compact scaffold composed of the 5.8S rRNA, the ITS2, and domains I and II of the 25S rRNA (**state A**). Furthermore, domain VI is stably incorporated forming a closed ring-like structure (**state B**), while the domains III to V remain flexible and will be only later assembled (**state F**). The formation of the polypeptide exit tunnel (PET), which is displayed as a black arch or circle, starts with the ring-like structure circularization and it is completed when domain V is fully folded as observed in state F *(Kater et al., 2017*).

The stabilization of the rRNA domains in these nucleolar intermediates is enabled by tight cooperation between ribosome assembly factors and ribosomal proteins. One of many examples is the stabilization of the ITS2 rRNA, which is mediated by the assembly factors Nsa3, Nop7, Erb1, Rlp7, and Nop15. The ITS2 rRNA forms with its associated assembly factors one of the first regions to stably fold into the pre-60S particle (*Kater et al., 2017; Sanghai et al., 2018; Zhou et al., 2019a)*, which is a structural landmark named foot *(Bradatsch et al., 2012)*. Besides being part of the foot, Erb1 contacts, via its long N-terminal tail, additional assembly factors, such as Nop16, the helicase Has1, and the Brx1–Ebp2 heterodimer *(Kater et al., 2017*). In addition, Erb1 stably interacts, via its C-terminal β-propeller domain, with Ytm1 (*Thoms et al., 2016*), which is the substrate of the first of two essential release reactions performed by the AAA^+ ATPase Rea1 (*Baßler et al.,2010)* (see paragraph 1.3 for more details)**.** In the nucleolus, Rea1 binds Ytm1 and hydrolyzes ATP to induce the release of Ytm1-Erb1-Nop7 subcomplex from the pre-ribosome (*Baßler et al.,2010)*. Since Erb1 contacts many assembly factors, it can be considered an “interaction hub” whose

removal is essential to trigger the exit of its associated factors. The AAA+ ATPase Rea1-mediate removal of Ytm1-Erb1-Nop7 coincides with another remodelling event, such as the ITS2 processing. In more detail, at the transition from the nucleus to the nucleoplasm, the prominent foot structure is removed **(Fig. 4** steps **K-L)** through the ITS2 processing **(Fig. 9)**, mediated by Las1-complex (Las1, Grc3, Rai1, and Rat1) which cleaves at C_2 site of the 27SB pre-rRNA, and separates the 7S from the 26S pre-rRNAs (*Gasse et al.,2015)*. Subsequently, the 5'-3' exonuclease Rat1-Rai1 trims the 5'-end of the 26S pre-rRNA to yield the 25S rRNA (*Gasse et al.,2015, Fromm et al., 2017*). Meanwhile, Nop53, which has previously replaced Erb1 on the maturing pre-ribosome, recruits to the 7S pre-rRNA the RNA nuclear exosome, a major 3'-5' exoribonuclease complex (*Thoms et al., 2015*). The RNA nuclear exosome degrades the extra nucleotides of the 3'-end of the 7S to generate the 6S (*Mitchell et al., 1997; Schuller et al., 2018*)**.** The 7S pre-rRNA processing enables the dissociation of ITS2-associated factors, mainly Cic1, Rlp7, and only partially Nop53 and Nop7 **(Fig. 9).** Later in the cytoplasm, the non-essential cytoplasmic exonucleases, Ngl2, Rex1, Rex2, and Rex3, further process the 6S pre-rRNA to produce the mature 5.8S rRNA (*Tomecki et al., 2017)*.

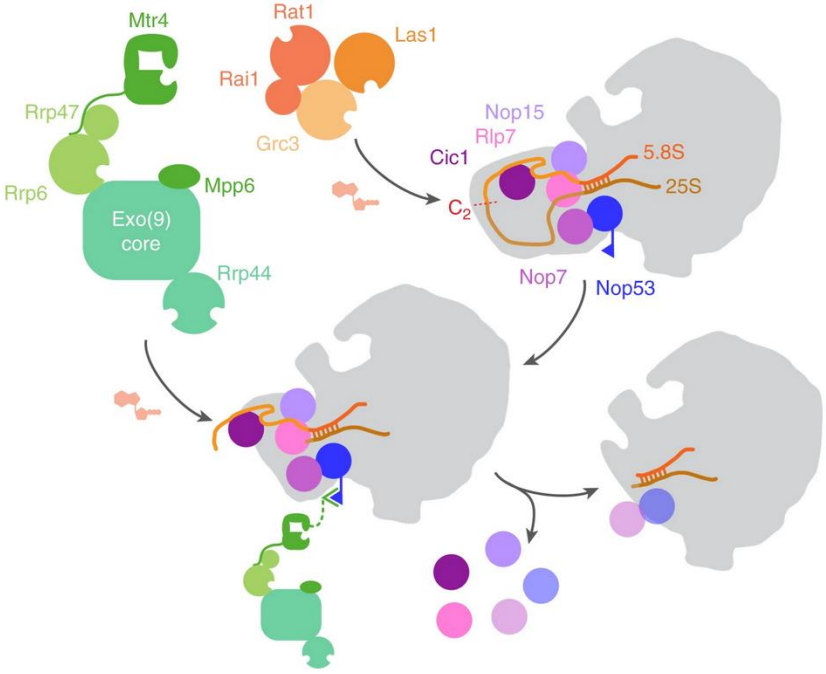

Figure 9. Scheme of *in vitro* reconstitution of ITS2 removal pathway from pre-60S particles. The Las1 complex initiates the ITS2 processing by cleaving at the C_2 site and then degrades the resulting 26S pre-rRNA to 25S pre-rRNA, which facilitates the processing of the 7S pre-rRNA to 5.8S by RNA nuclear exosome. The RNA nuclear exosome is recruited by Nop53, which interacts with the helicase Mtr4 bound to Rp47 and Rrp6. Final processing of 7S pre-rRNA efficiently releases the ITS2-associated factors Cic1 and Rlp7, and only partially Nop53 and Nop7. Adapted from *Fromm, 2017.*

During the early steps of the biogenesis, in the nucleolus, the 5S rRNA, transcribed by the RNA polymerase III, forms upon binding to Rpl5 (uL18) and Rpl11 (uL5), the 5S RNP complex, which is then incorporated into pre-60S particles *(Zhang et al., 2007)*. The 5S RNP incorporation is chaperoned by the Rpf2-Rrs1 heterodimer, which is necessary for its recruitment and stabilization on the pre-60S particle into an unrotated state, in which the 5S RNP is twisted of 180° compared to its position in the mature 60S subunit (*Leidig et al., 2014; Wu et al., 2016; Thoms et al., 2018*). At a later nuclear step, the maturation of the pre-60S pre-ribosome involves the 180° rotational movement of the 5S RNP with consequent maturation of the central protuberance **(Fig. 10).** How the 5S RNP rotation and central protuberance reorganization occurs is still unclear. However, it could depend on the dissociation of the Rpf2-Rrs1 heterodimer and be coupled with the crucial structural rearrangements mediated by the AAA^+ ATPase Rea1 **(Fig. 4** step **M)**.

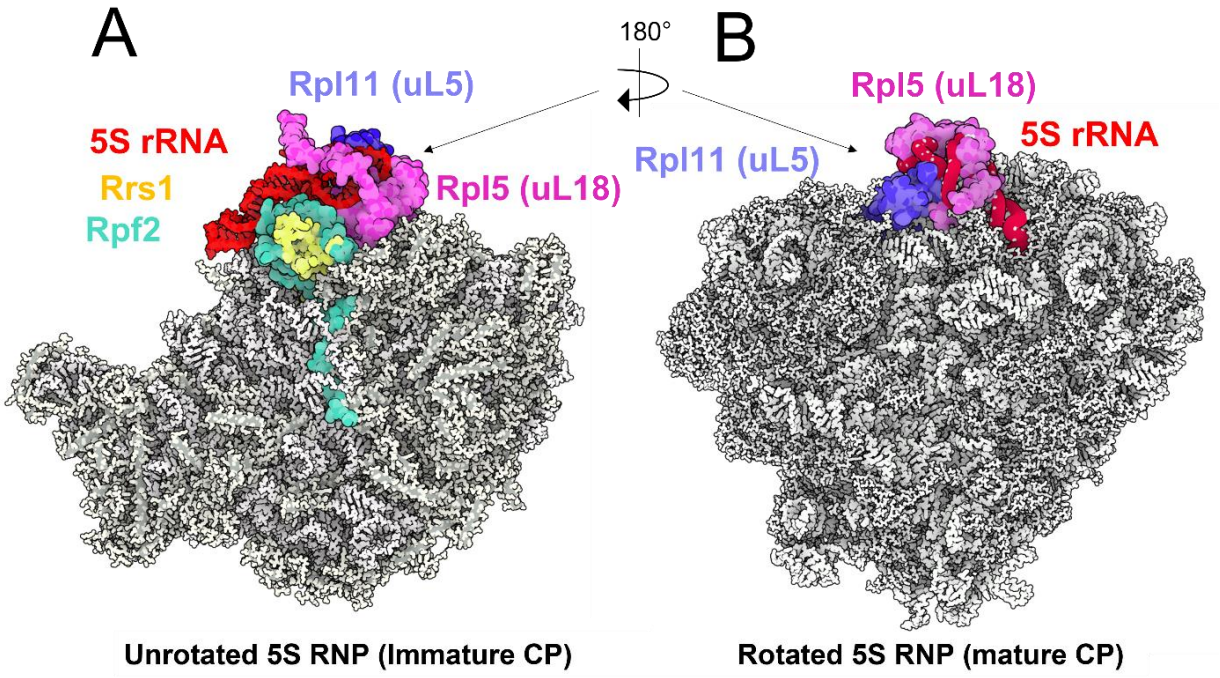

Figure 10. Representation of the 5S RNP in its unrotated and rotated state.
A) The structural model of the Nog2-containing particle shows an intermediate where the 5S RNP is in its untrotated position and the central protuberance is in its immature conformation (PDB codes: 3JCT). **B)** The structural model of the mature ribosome (PDB code: 4V88) is depicted and displays the rotated 5S RNP and mature conformation of central protuberance. Proteins and rRNA are shown in grey. The members of the 5S RNP and the Rrs1 and Rpf2 chaperones are are shown in color: the 5S rRNA is shown in red, Rrs1 in yellow, Rpf2 in cyan, Rpl5 (ul18) in pink, Rpl11 (ul5) in violet.

Precisely, the AAA^+ ATPase Rea1 binds Rsa4, which is located in the proximity of the central protuberance, and triggers Rsa4 removal from the pre-60S particles (see paragraph 1.3 for more details). It is suggested that this remodelling step may produce a conformational change within the pre-60S particle that could stimulate a following further step, such as the K^+-dependent GTPase activity of Nog2 (*Matsuo et al., 2014)*. Nog2, together with Nog1, covers the nascent PTC; hence the release of Nog2 has as a consequence the structural rearrangement of the PTC in a close-to-mature conformation. The PTC maturation upon Nog2 release is essential to recruit the leucine-rich nuclear export signal (LR-NES)-containing export adaptor Nmd3, which plays a critical role during the export of the maturing pre-60S particles from the nucleus to the cytoplasm (*Ma et al., 2017; Matsuo et al., 2014).*

The export of the pre-60S particles takes place through the nuclear pore complex (NPCs), which is embedded within the double bi-layered nuclear envelope and whose channel is filled with the Phenylalanine-Glycine (FG)-rich repeats of the nucleoporins forming a hydrophobic hydrogel sieve (*Frey et al., 2006*). The small GTPase Ran (Gsp1 and Gsp2 in yeast) provides the directionality for this transport system. In the nucleoplasm, Ran-GTP promotes the formation of complexes between export receptors, such as Ndm3 and exportin Crm1/Xpo1, a member of the karyopherin β family. More in detail, Crm1/Xpo1 recognizes the leucine-rich nuclear export signals (LR-NES) present on Nmd3, allowing an active transport of the pre-60S subunit through the NPC. Following the transport, these complexes dissociate in the cytoplasm when GTP is hydrolyzed. Moreover, additional factors have been suggested to take part in the export of the pre-60S particles together with Nmd3, such as Arx1 (*Bradatsch et al., 2007*) and Mex67-Mtr2 (*Yao et al., 2007*). These export factors are distributed all over the surface of the pre-60S particles (*Bradatsch* et al., 2012, *Greber et al., 2012*) and interact directly with the FG-rich repeats of the nucleoporins, suggesting that they could shield the pre-ribosome from the hydrophobic surroundings of the NPC channel, thus allowing their passage (*Ho et al., 2000; Gadal et al., 200).*

1.2.3.2 The cytosolic steps of the pre-60S subunit maturation

The pre-60S particles, upon export into the cytoplasm, are still inactive and require a few additional steps to gain translational competence (*Karbstein, 2013*), such as the final processing of the 6S into the 5.8S rRNA (*Thomson et al., 2010*), the releases of the assembly factors Nog1, Mrt4, Tif6, and the release of the export adaptors Rlp24, Mex67-Mtr2, Arx1, Bud20 and Nmd3 (*Lo et al., 2010*), most of which were shown to be energy-dependent events and involve ATPase or GTPase activities. In addition, in the cytoplasm occurs the incorporation of the last ribosomal proteins such as Rpl10, Rpl24, Rpl29, Rpl40, Rpl42, Rpp0, P1, and P2 (reviewed in *de la Cruz et al., 2015*)

As already mentioned, (paragraph 1.2.3) the 6S pre-rRNA is finally trimmed generating, in the cytoplasm, the 5.8S rRNA, a processing event that is mediated by the exonuclease Ngl2 (*Thomson et al., 2010*).
Furthermore, the AAA^+ ATPase Drg1 is recruited and activated by Rlp24 to catalyze the removal of Rlp24 itself. Rlp24 and the ribosomal protein Rpl24 share high sequence similarity with the first protein being a placeholder for the second one. Therefore, the Rlp24 removal enables the recruitment of Rlp24 on the pre-60S subunit (*Saveanu et al., 2003*). This step may be prerequisite for following events occurring during the pre-60S cytoplasmic maturation, such as the release of two GTPases (Nog1 and Nug1), the assembly factors Nsa2, the subunit anti-association factor Tif6, the ribosomal-like protein Mrt4 and the export factors Mex67-Mtr2, Bud20, Arx1, and Nmd3, which are then recycled back to the nucleus *(Loibl et al., 2014; Zisser et al., 2018)*. More in detail, Drg1-mediated release of Rlp24 may enable the activation of Rei1 that together with the ATPase Ssa1/2 (Hsp70) and its cofactor Jjj1 releases the export adaptor Arx1 and its binding partner Alb1 from the region proximal to the polypeptide exit tunnel (PET) *(Demoinet et al., 2007; Lo et al., 2010)*. Furthermore, the Nog1 removal from the pre-60S permits the maturation of the peptidyl transferase center and may allow phosphatase Yvh1 to mediate the release of the placeholder Mrt4 (*Klingauf-Nerurkar et al., 2020*) which is now replaced by its paralog the ribosomal protein Rpp0 (uL10) (*Kemmler et al., 2009)*. This step contributes to the formation of the P-stalk, a pentameric complex that is composed of Rpp0 and two copies of the heterodimer P1-P2 and is involved in translation (*Lo et al., 2009*).

The last events, such as the incorporation of the ribosomal protein Rpl10 and the removals of Nmd3 and Tif6, contribute to the functional site proofreading (*Hedges et al., 2005*; *West et al., 2005*). In early cytoplasmatic intermediates *(Kargas et al., 2019; Zhou et al., 2019b)* Nmd3 was shown to contact Tif6 and to occupy the A, P, and E sites of the tRNA channel, preventing the association of tRNAs to these sites (*Patchett et al., 2017*).

The GTPase Lsg1 binds and removes Nmd3, allowing the accommodation of Rpl10 at the PTC. Rpl10 senses the occurrence of the correct assembly of the PTC and, only then, activates the GTPase Efl1 that, together with the co-factor Sdo1 causes the release of the anti-association factor Tif6. Indeed, Tif6 is an assembly factor that sterically blocks the premature coupling of the 40S and 60S subunits *(Gartmann et al., 2010; Bussiere et al., 2012)*; hence, Efl1 might couple proofreading activity with the removal of factors that prevent nascent 60S subunit from interacting with 40S subunits. Thereafter, new 60S subunits can enter the pool of functioning subunits (reviewed in *Panse and Johnson, 2010*).

1.3 The AAA$^+$ ATPase Rea1 fulfils an essential role in ribosome assembly

1.3.1 Structural and functional insights into the Rea1 protein

During the ribosome assembly the AAA$^+$ ATPases (ATPases Associated with various cellular Activities) mediate structural rearrangements and/or substrate release by converting the chemical energy of the ATP hydrolysis into mechanical force (*Ogura and Wilkinson, 2001*). The AAA$^+$ ATPase Rea1 is the largest protein in *S. cerevisiae,* composed of 4910 amino acids (540 KDa), and is conserved from yeast to humans (*Prattes et al., 2019*). Rea1 is an essential protein, indeed, its genetic depletion or specific mutations in yeast (*Galani et al., 2004 Ulbrich et al., 2009)*, or knock-down in humans *(Raman et al., 2016*) are either lethal or have strong effects on cell growth. Rea1 is composed of five distinct domains: the N-terminal domain (NTD), AAA$^+$ ATPase ring (or ring domain) containing six tandem AAA$^+$ protomers (from AAA1 to AAA6), the linker domain, aspartate/glutamate (D/E)-rich domain, and carboxy-terminal MIDAS (Metal Ion-Dependent Adhesion Site) domain (G*arbarino and*

Gibbons) **(Fig. 11A**). The Rea1 protein was for the first time identified as a ribosome biogenesis factor in 2001, in a study where it was found that a conserved and essential protein encoded by the ORF YLR106c (systematic name of the REA1 gene) was co-purified with late nucleolar Nug1-containing pre-60S particles *(Baßler et al., 2001*). Next, it was also observed that Rea1 was enriched in nucleoplasmic Rix1-containing particles *(Nissan et al., 2004)*. The co-purification of Rea1 with pre-ribosomes allowed a first structural characterization via negative staining electron microscopy *(Nissan et al., 2004; Ulbrich et al., 2009)*. In these studies, it was shown that Rea1 makes contacts with the pre-ribosome through its ring domain while its flexible tail protrudes, thus giving the pre-ribosome a distinctive 'tadpole-like' appearance. The head of the "tadpole" is the pre-ribosome and the tail is Rea1 *(Nissan et al., 2004)*. Furthermore, it was also revealed that the Rea1 tail can oscillate from its tail-protruding conformation to a conformation where the tail is folded back onto the pre-ribosome and nearby the ring (*Ulbrich et al., 2009)*, possibly bringing the MIDAS domain close to Rea1 substrates placed on the pre-60S particles (*Ulbrich et al., 2009)*. Further structural characterization of *S. cerevisiae (Sosnowski et al., 2018)* **(Fig. 11B)** and *S. pombe* Rea1 (*Chen et al., 2018)* was also obtained via cryo-EM. These cryo-EM reconstructions offered interesting insights into the architecture of the protomers of the ring domain and the regulation of the ATPase activity of this essential molecular machine *(Sosnowski et al., 2018)*

The six AAA^+ protomers composing the ring of Rea1 show differences in length and conservation, suggesting that they evolved independently to exert distinct roles. Indeed, protomers from AAA2 to AAA5 contain a Walker-A motif binding to the ATP, an arginine-rich motif promoting ATP hydrolysis, and a Walker-B motif that hydrolyzes the ATP γ-phosphate. Notably, in both AAA1 and AAA6 protomers the consensus sequence of the Walker-B motifs is not conserved; thus they cannot hydrolyze ATP at their sites *(Sosnowski et al., 2018).*

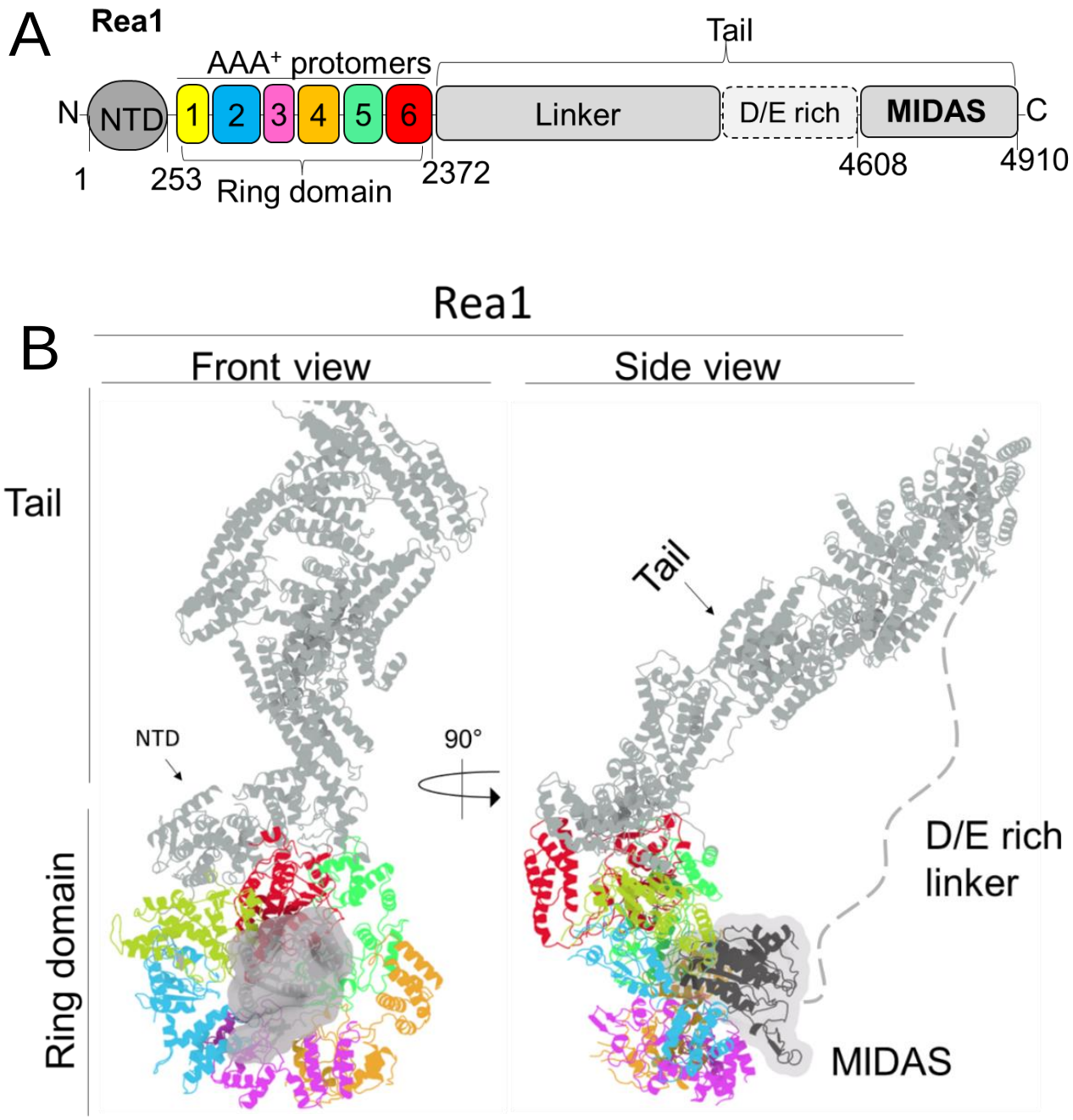

Figure 11. Domain organization and cryo-EM reconstruction of the AAA⁺ ATPase Rea1.
A) Rea1 consists of five domains. From left to right are indicated the N-terminal domain (NTD), the ring domain that is composed of six tandem ATPase protomers (AAA⁺ protomers) depicted in yellow (AAA1), cyan (AAA2), pink (AAA3), orange (AAA4), green (AAA5), and red (AAA6). The ring domain is followed by the tail, which is composed of a long α-helical linker, an unstructured aspartate/glutamate (D/E) rich region, and a C-terminal MIDAS domain, which is involved with the binding to the substrate. The AAA⁺ protomers are shown in unequal sizes reflecting the difference in sequence length. The D/E rich domain is shown with a dashed border because it is unstructured. **B)** Two opposite views (front and side view) of the Rea1 structure from *S. cerevisiae* are displayed. The N-terminal domain (NTD) and the flexible tail are depicted in dark grey. The flexible and unstructured aspartate and glutamate (D/E) rich liker is represented with a dashed line. The MIDAS domain is shown in light grey and as a surface representation of the Cryo-EM density map and is docked into the central pore of the ring domain. The AAA⁺ protomers are colored in yellow (AAA1), cyan (AAA2), pink (AAA3), orange (AAA4), green (AAA5), and red (AAA6) (PDB code: 6YLH) according to the amino acidic sequence reported in uniprot (UniProtKB - Q12019).

The protomers from AAA1-AAA5 consist of an α/β large domain (AAAL) made up of five α-helices and five β-strands (H0-H4, S1-S5), and a small domain (AAAS) consisting of an α-helical bundle. The AAA6 protomer consists of only the large domain, thus lacking the small domain **(Fig. 12)**. All large domains, (AAALs) have a β-sheet insert within H2 and another β-sheet insert between H4 and S3. Each β-sheet insert within H2 in the large domains of AAA2, AAA4, and AAA6 is extended by an α-helical bundles (H2α) (*Sosnowski et al., 2018; Chen et al., 2018)* **(Fig. 12).**

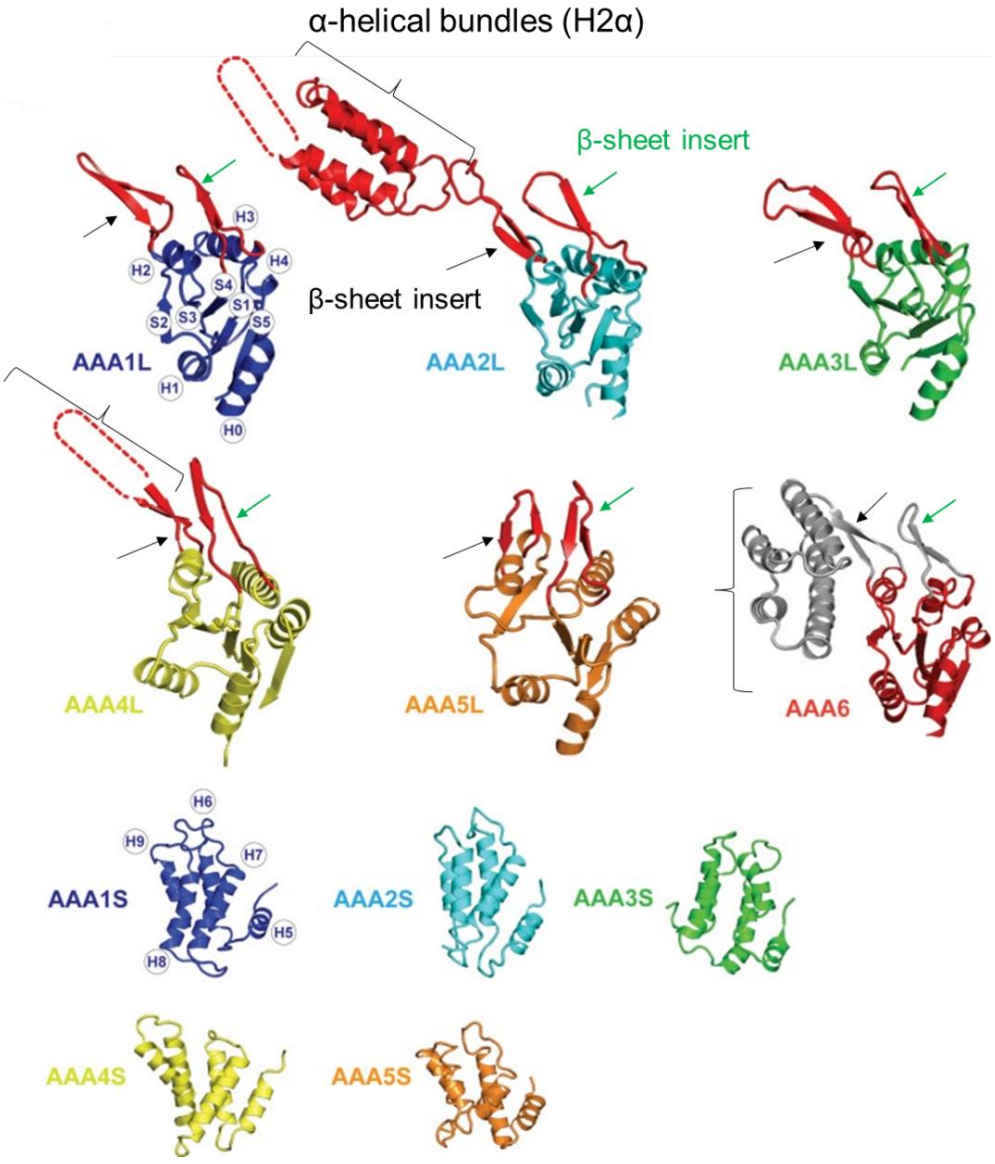

Figure 12. Structure of AAA⁺ protomers of the ring domain of Rea1.
The protomers from AAA1-AAA5 are composed of an α/β large domain (AAAL) containing five α-helices and five β-strands (H0-H4, S1-S5), and a small domain (AAAS), which is indicated below consisting of α-helical bundle (H5-H9). Only AAA6 does not contain a small domain. All the large domain contain a β-sheet inserts within H2 and between H4 and S3, while only protomers AAA2L, depicted in light blue, AAA4L, depicted in yellow, and AAA6L, depicted in red contain an additional α-helical bundles, which in the case of AAA2L has higher dimension than the other and has a functional role.

Notably, in the cryo-EM structure of Rea1 in absence of pre-60S particles, it is shown that the AAA2 α-helical bundle (H2α) partially occupies the ring domain pore **(Fig. 13A)**, thus impairing the docking of the MIDAS domain into it (*Sosnowski et al., 2018)***.** Remarkably, in the cryo-EM structure of Rea1 associated with Rix1-containing pre-ribosomes, it is shown that Rea1 binds to the pre-ribosomes, while the AAA2 α-helical bundle (H2α) makes contacts with the Rix1-subcomplex (*Barrio-Garcia et al., 2016*) (see the model in **Fig. 13B**). This interaction is suggested to keep the AAA2 α-helical bundle (H2α) away from the ring domain pore and favour the docking of the MIDAS domain onto the ring. In this new position, the MIDAS domain may now interact with its direct substrates (*Sosnowski et al., 2018)* **(Fig. 13B)**.

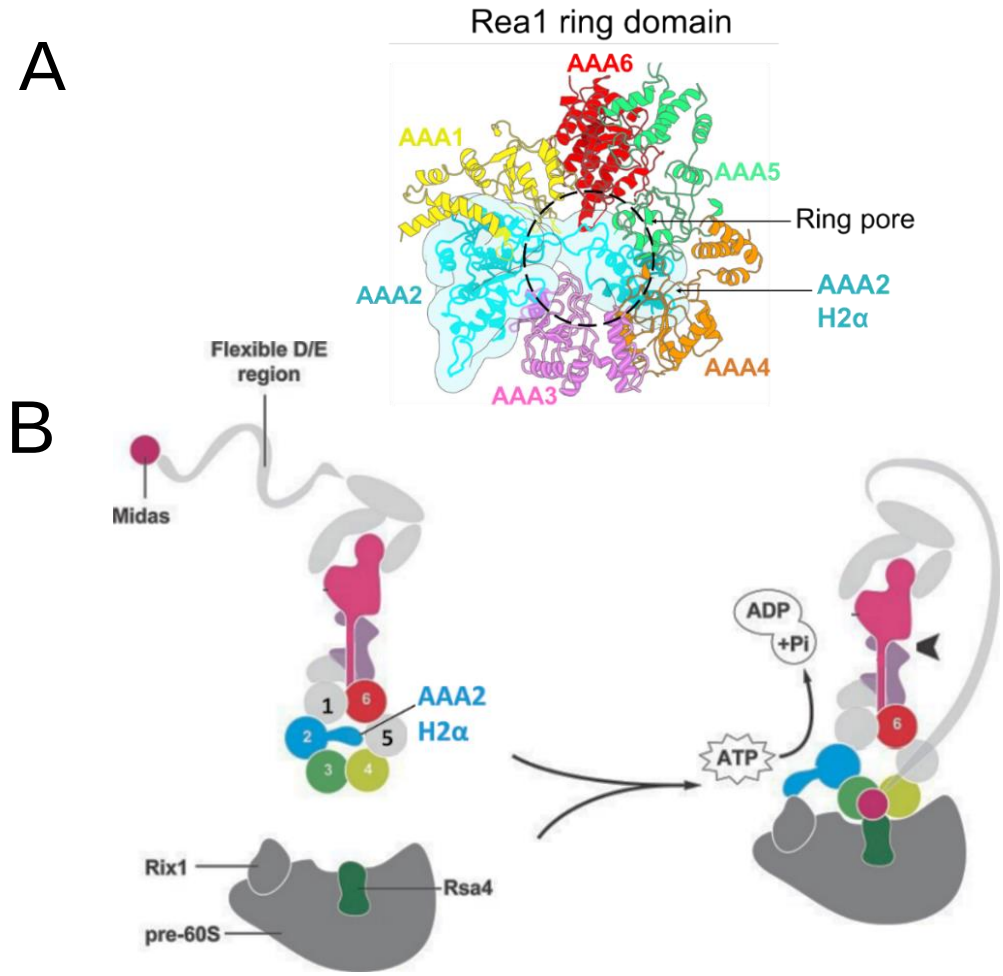

Figure 13. Displacement of the α-helical bundle of the AAA2 allows the docking of the MIDAS domain into the ring and the binding to the substrate.
A) Model of the Rea1 ring domain, in which the AAA$^+$ protomers are specified. Protomer AAA2 is represented both as ribbon diagram and as surface representation. Note that AAA2 α-helical bundle is inserted into the ring pore, trapping the ring domain in a open conformation (PDB CODE: 6YLH). **B)** Simplified cartoon showing a model for the displacement of the AAA2 α-helical bundle from the ring pore upon binding to the Rix1 subcomplex. The displacement of the AAA2 α-helical bundle stimulates the ATP hydrolysis, the docking of the MIDAS domain onto the ring domain, and the binding of MIDAS to the Rsa4 substrate. Adapted from *Sosnowki et al., 2018*.

1.3.2 The MIDAS domain of Rea1 interacts with the UBL domains of Ytm1 and Rsa4

The first identified Rea1 substrate was the 60S assembly factor Rsa4 (*Ulbrich et al.,2009*). Shortly after that, additional genetic and biochemical analyses revealed that another 60S assembly factor, Ytm1, also interacts with Rea1 (*Baßler et al., 2010*). Ytm1 and Rsa4 are two essential ribosome biogenesis factors associated with the pre-60S subunit at different maturation steps. Ytm1 associates early with pre-60S intermediates in the nucleolus, whereas Rsa4 associates later with nucleoplasmic pre-60S particles (*Baßler et al. 2010; Ulbrich et al. 2009*). *In vitro* release assays showed that upon ATP treatment Rea1 releases its direct substrates, Ytm1 and Rsa4, and additional assembly factors from purified pre-ribosomes *(Baßler et al. 2010, Ulbrich et al., 2009)*. Therefore, it was proposed that Rea1 hydrolyzes ATP within its ring domain and converts the chemical energy into a mechanical force that extracts its direct substrates from pre-60S pre-ribosome **(Fig.14)** *(Baßler et al. 2010, Ulbrich et al., 2009).*

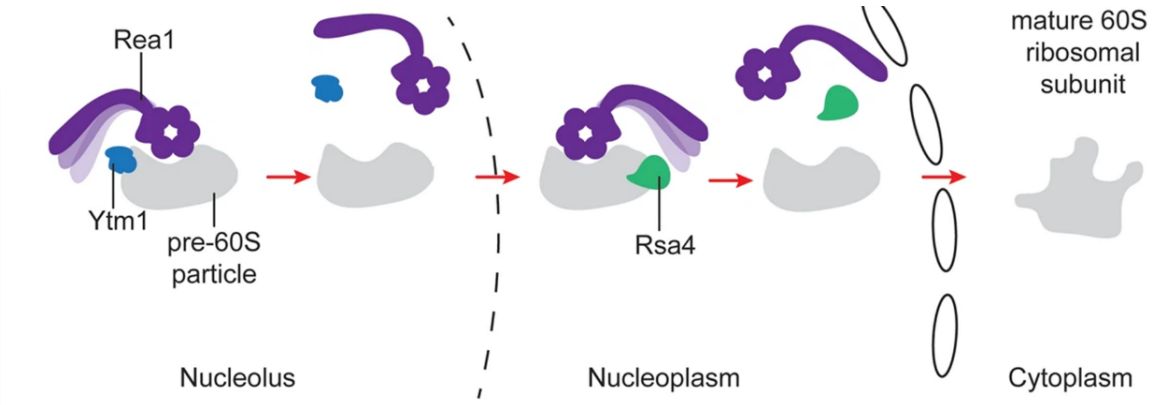

Figure 14. Model of the Rea1-mediated removals of Ytm1 and Rsa4 during the 60S subunit biogenesis. Rea1 binds to Ytm1 and Rsa4 enabling their removals in the nucleolus and nucleoplasm, respectively. Rea1 is depicted in violet, Ytm1 in blue, Rsa4 in green. Pre-60S particles are depicted in grey. Nucleolus, nucleoplasm, and cytoplasm are indicated. From *Sosnowki et al., 2018*.

The domain organization of Ytm1 and Rsa4 is very similar. Both proteins are composed of an N-terminal UBL domain, which is responsible for the interaction with the MIDAS domain of Rea1, and a C-terminal WD40 repeat β-propeller. A recent X-ray crystallography study has shed light on the Rea1-MIDAS domain and how the

interaction with its ligands is established **(Fig. 15A)** (*Ahmed et al., 2019*). Indeed**,** the MIDAS domain of Rea1 turned out to be structurally similar to α-I domain of integrins and to the A1 domain of the von Willebrand factor (note that the α-I domain of integrins and the A1 domain of the von Willebrand factor are highly homologues) *(Lee et al., 1995).* In the integrins, the MIDAS domain forms five coordination bonds with the central Mg^{2+} ion within the consensus motif ($DXSXSX_{70}TX_{30}D$), while the sixth coordination bond is provided by highly conserved acidic residues of the ligand. Similarly, the Rea1 MIDAS domain forms five coordination bonds with a central Mg^{2+} ion accordingly to the above-mentioned integrin consensus motif, while the sixth coordination bond is provided by a highly-conserved acidic residue within the UBL domain of the binding partners, such as E114 of Rsa4 and E80 of Ytm1 in *S.cerevisiae* (*Baßler et al., 2010*; *Romes et al., 2016)* and E117 of Rsa4 **(Fig. 15B)** and E88 of Ytm1 and in *C. thermophilum* (*Ahmed et al., 2019*). These interactions are essential. Indeed, the abrogation of the Rea1-Ytm1 or Rea1-Rsa4 interaction via the point mutation E80A within the Ytm1-UBL domain or E114D/A within the UBL domain of Rsa4 impairs further progression of the ribosome assembly, conferring to yeast cells a lethal and dominant-negative phenotype.

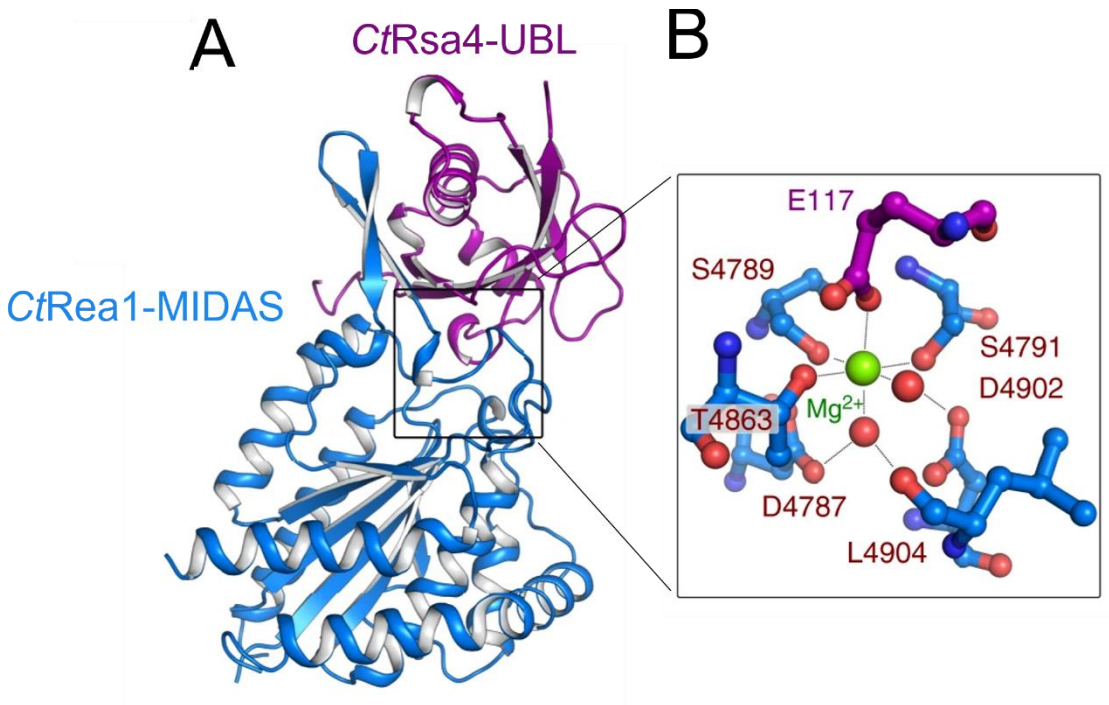

Figure 15. Crystal structure of *Ct*Rea1-MIDAS domain in complex with the *Ct*Rsa4-UBL.
A) The crystal structure of Rea1-MIDAS – Rsa4-UBL complex from *Chaetomium thermophilum* is shown. The Rea1 MIDAS domain ∆loop is depicted in blue and the Rsa4 UBL domain in violet. **B)** The magnification shows in blue the five consensus residues (D4787, S4789, S4791, T4863, D4902) within the Rea1-MIDAS domain forming five coordination bonds with the Mg^{2+}. In addition, the sixth coordination bond is provided by the Rsa4-UBL domain via the glutamate E117, which is depicted in violet. From *Ahmed et al., 2019*.

In addition to the structural similarity of the Rea1-MIDAS domain with the integrin A1 domain **(Fig. 16A)**, it was also suggested that the Rea1-MIDAS domain contains additional motifs that are not found within the integrin α-I domain and confer to Rea1-MIDAS domain its specific function in ribosome biogenesis. Two of those unique motifs are a long α-helix (element I) wrapping the MIDAS domain itself **(Fig. 16B in blue)** and an essential loop **(Fig. 16B in yellow)**, which forms a β-hairpin (element III) only upon interaction with the UBL domain and provides an additional binding site for the UBL domain itself **(Fig.17)** (*Ahmed et al., 2019*). A third additional feature is an essential extended loop (element II or MIDAS loop) projected from the MIDAS domain **(Fig. 16B in red)** and bearing a highly conserved proline-tyrosine-nuclear localization sequence (PY-NLS) (*Ahmed et al., 2019*).

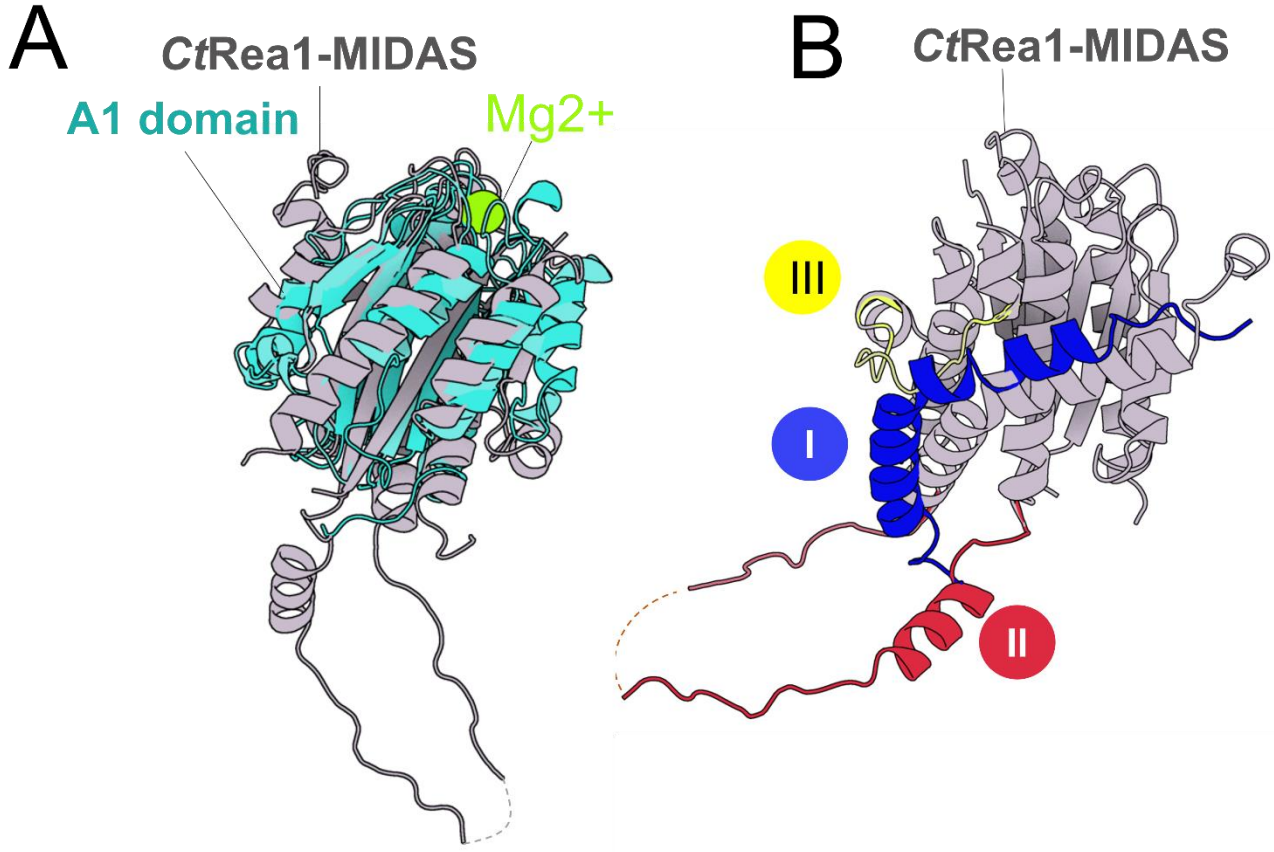

Figure 16. Rea1-MIDAS is structurally related to the α-I domain of integrins but contains additional structural features.
A) Superimposition of the crystal structures of the *Ct*Rea1-MIDAS domain, which is depicted in grey (PDB code: 6QT8) and the A1 domain of von Willebrand factor, which is highly homologous to the integrin α-I domain and is depicted in cyan (PDB ID: 1SQ0). **B)** The *Ct*Rea1-MIDAS structure with the specific features enabling its function during ribosome assembly. In blue is shown the long α-helix (element I), in red is shown the extended loop, and in yellow the loop forming the β-hairpin upon binding to the ligand.

When the MIDAS loop is deleted, the import of Rea1-Δloop into the nucleus is impaired but no dominant-negative phenotype is observed (*Ahmed et al., 2019*). However, after inserting PY-NLS sequences from other unrelated nuclear proteins in the Rea1-Δloop, Rea1-Δloop import is restored, but causing a dominant-negative phenotype, suggesting that this loop might exert additional pivotal functions during the 60S subunit assembly (*Ahmed et al., 2019*). Accordingly, *in vitro* reconstitution assays clearly show that the MIDAS loop deletion impairs the ATP-dependent release of Rsa4 from pre-60S particles and the association of the MIDAS domain to the ring domain (*Ahmed et al., 2019*). Hence, the MIDAS loop is essential for the correct functioning of Rea1.

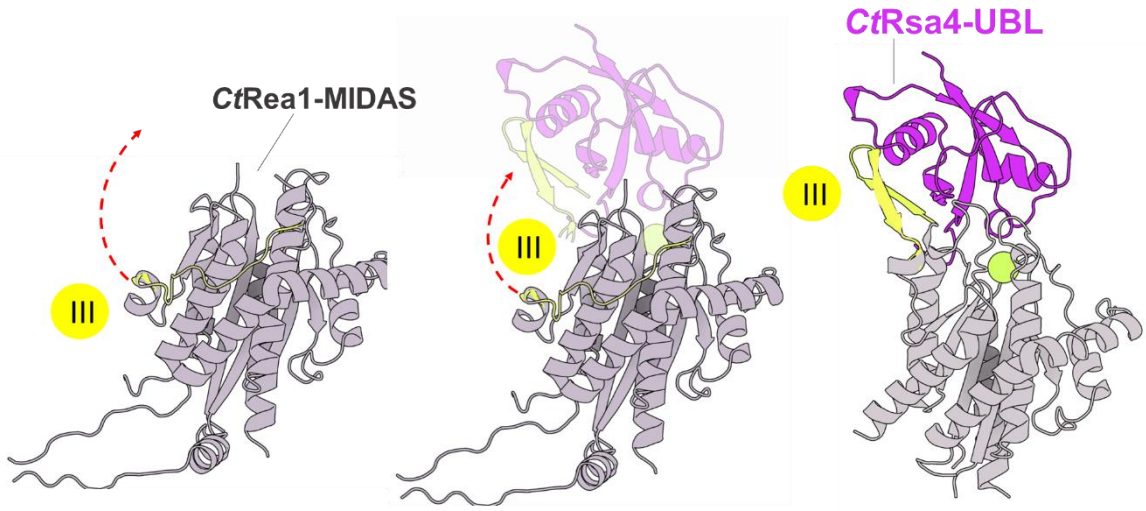

Figure 17. Model of the formation of the β-hairpin (element III) upon binding to Rsa4.
In the Rea1-MIDAS apostructure, in which the MIDAS domain is not interacting with the UBL domain of the either Ytm1 or Rsa4, the element III forms a loop, depicted in yellow. However, upon binding of Rea1-MIDAS to the ligands, the loop folds into a β-hairpin, which creates an additional surface contact for the binding of the UBL domain of the binding partner.

1.3.3 Integrins are promising therapeutical targets

Integrins are cell surface receptors that are involved in cell-to-cell and cell-matrix anchorage and, upon binding to extracellular ligands, mediate intracellular signalling cascades resulting in cell growth, proliferation, migration, adhesion, apoptosis, cytokine release and hence, play critical physiological roles during inflammation, coagulation, tissue repair, and angiogenesis (*Bachmann et al., 2019; Mezu-Ndubuisi*

and Maheshwari, 2021). These receptors are composed of two non-covalently associated transmembrane glycoprotein subunits termed α and β. While the α subunit determines the specificity of the integrin for the ligand, the β subunit is connected to the cytoskeleton and modulates the downstream signalling pathways *(Sökeland and Schumacher, 2019*). In vertebrates, there are eighteen α and eight ß subunits that can be combined into 24 heterodimers (*Takada et al., 2007)*. Nine of the eighteen α chains contain an α-I domain, which is approximately 190 amino acids long and is located at the N-terminus of the α subunit (*Larson et al., 1989*). The α-I domain is homologous to the A1-domain of the von Willebrand factor and is the ligand-binding domain in all the α-I domain-containing integrins *(Diamond et al., 1993; Michishita et al., 1993)*.
Structural studies have shown that the integrin α-I domain, similarly to the Rea1-MIDAS domain, is characterized by the typical tertiary structures termed α/β Rossmann fold, a series of alternating beta-stranded (β) and alpha-helical (α) elements **(Fig. 18A)** (*Luo et al., 2007)*, with a metal ion-binding site (MIDAS) that coordinates a central Mg^{2+} ion via five amino acidic residues D, S, S, T, and D, according to the consensus sequence $DXSXSX_{70}TX_{30}D$ *(Tozer et al., 1996)*. In addition, similarly to the Rea1-MIDAS domain, the sixth coordination bond is provided by an acidic residue (E or D) within the integrin ligands *(Shimaoka et al., 2003; Song et al., 2005; Luo et al., 2007)* **(Fig. 18B).**

Integrins are also linked to various pathological conditions such as infection, skin diseases, liver fibrosis, atherosclerosis, and cancer (*Bachmann et al., 2019*); therefore, they have emerged as promising therapeutical targets (*Slack et al., 2021*). Many integrin extracellular ligands, like adhesion molecules, matrix, and blood proteins, contain the Arg-Gly-Asp (RGD) attachment site that is recognized by nearly half of the known integrins. The Arg-Gly-Asp (RGD) attachment site, constituting the primary recognition system for cell adhesion, has been extensively exploited to develop integrin inhibitors (*Ruoslahti and biology, 1996*). Indeed, integrin function can be inhibited at various levels, such as impairing the formation of the integrin-ligand complex by using RGD-ligand mimetic inhibitors (*Slack et al., 2021*), targeting signalling effectors that act downstream to the integrins, or delivering a cytotoxic RGD-conjugated drug to the cells of interest expressing integrins on their surface (*Chen and Chen, 2011*). Remarkably, most integrin drug discovery initiatives mainly target the formation of the

integrin-ligand complex, generating several currently-used drugs (*Slack et al., 2021*). The first drugs to be developed were RGD-ligand mimetic inhibitors specific for the integrin αIIbβ3. Among those integrin antagonists are the chemical compounds tirofiban (Aggrastat) and eptifibatide (Integrilin), alongside the antibody abciximab (ReoPro). These drugs have been used for acute coronary syndrome and the treatment of thrombotic events (*McClellan and Goa, 1998; Goa and Noble, 1999).* Curiously, peptides that contain the RGD attachment site and function as integrin antagonists are also available in nature. These natural antagonists are commonly known as disintegrins. Two of them, called Jarastatin and Jararacin, are purified from the venom of the snake *Bothrops jararaca* and bind with high affinity to the αIIbβ3 integrin, which is involved in platelet adhesion and aggregation. Indeed, Jarastatin and Jararacin have been successfully used as platelet aggregation inhibitors *in vitro* (*Wermelinger et al., 2009*).

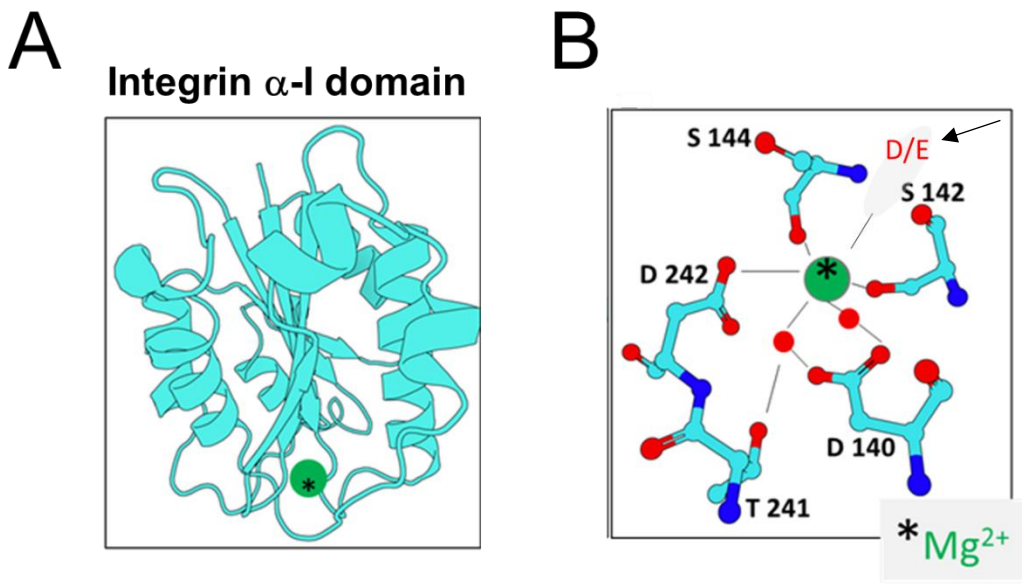

Figure 18. **Structure of the α-I domain of the integrin complement receptor 3 (CR3)**. **A**) The α-I domain of the integrin has a typical α/β Rossmann fold and coordinates the Mg^{2+} ion, depicted as green sphere and indicated with and asterisk. **B**) The magnification shows in cyan the five consensus residues (D140, S142, S144, T241, D242) within the α-I domain of Integrin CR3 forming five coordination bonds with the Mg^{2+}. In addition, the sixth coordination bond is provided by the ligand via a conserved acidic residue, aspartate (D) or glutamate (E), which is indicated with a black arrow. PDB code: 1IDO.

1.4 The role of ribosome biogenesis in human diseases

1.4.1 A defective ribosome biogenesis causes diseases named ribosomopathies

An increasing number of studies have shown that mutations within human ribosome assembly factors, ribosomal proteins or RNA polymerase I can lead to defects within ribosome biogenesis and overall lower translation efficiency, causing inherited human diseases termed ribosomopathies (reviewed in *Kampen et al., 2020*; *Venturi and Montanaro, 2020*), among which the most known are Diamond-Blackfan anemia (DBA), the Schwachman-Diamond syndrome (SDS), the X-linked dyskeratosis congenita (DC) and the cartilage hair hypoplasia (CHH) *(Kampen et al., 2020*). In patients affected by Diamond-Blackfan anemia (DBA) a disease leading to a selective decrease in erythroid precursors and anemia *(Gustavsson et al., 1997)* occur mutations within the RPS9 gene, encoding for a cytoplasmic ribosomal protein associated with the small 40S subunit *(Ellis and Gleizes, 2011)*. In the Schwachman-Diamond syndrome occur loss-of-function mutations of the gene SBDS gene (SDO1 in yeast), which promotes the release of the anti-dissociation factor eIF6 (Tif6 in yeast) from pre-60S subunits *(Burroughs et al., 2009*), thus blocking the ribosome subunit coupling during the final steps of cytoplasmic maturation.
The cartilage hair hypoplasia (CHH) is a disorder affecting the connective tissue with consequently reduced bone growth. CHH is linked to mutations within the RMRP gene (Nme1 in yeast) encoding for the RNA component of the mitochondrial RNA processing (MRP) endoribonuclease, which mediates cleavage and processing of the pre-rRNA within the ITS1, thus leading to reduced levels of mature 18S and 5.8S rRNAs (S*ulima et al., 2014*).
Although ribosomes are necessary to every cell of the body, one interesting aspect of ribosomopathies is that the disease-associated phenotype in ribosomopathy patients is restricted to specific tissues. One of them is the hematopoietic system, since the bone marrow function relies heavily on cell division, which has to be supported by correct number of functional ribosomes *(Mills and Green, 2017).* Rarely, also cartilagineous and bone tissues can be affected since chondrocytes and osteoblasts secrete the organic matrix and therefore require high protein synthesis, which can be

compromised by ribosome mutations (*Matsui et al., 2013*). Another curious aspect of ribosomopathies is that patients, due to the lack of functioning ribosomes, experience at first hypo-proliferative clinical symptoms, such as anemia or bone marrow failure. However, during the disease progression some compensatory mutations may occur that eventually result in cellular hyperproliferation (S*ulima et al., 2014*). This compensation mechanisms leads to a paradoxical evolution from hypo- to hyper-proliferative symptoms with consequent increased incidence of solid tumors (*De Keersmaecker et al., 2015*).

Intense research efforts over the last decades have tried to shed light on the mechanisms behind the hypo-proliferative phase of ribosomopathies, suggesting that it might occur due to the oncosuppressor p53 and the activation, in the nucleus, of a checkpoint mechanism directing cells with defective ribosome assembly to apoptosis (for more details see the next paragraph 1.4.2) *(Šulić et al., 2005; Deisenroth and Zhang, 2010;)*.

1.4.2 The 5S RNP connects ribosome biogenesis defects with p53 homeostasis

Cell growth and cell division require a high amount of protein synthesis, hence fully-functional ribosome biogenesis is a prerequisite to support these processes. For this reason, high eukaryotes have evolved a mechanism to block the cell cycle in case of impaired ribosome biogenesis, causing the hypo-proliferative symptoms occurring in ribosomopathies *(Turi et al., 2019).* The main player involved in the block of the cell cycle is the tumor suppressor protein p53 *(Golomb et al., 2014*). Under normal conditions, the p53 levels are kept low because of the oncoprotein murine double minute 2 (Mdm2), an E3 ubiquitin ligase that mediates the ubiquitylation of p53 and targets it to degradation via the 26S proteasome *(Haupt, 1997; Honda et al., 1997; Hock and Vousden, 2014*). Despite the deep knowledge regarding the p53/Mdm2 axis and its fine modulation of cell growth and apoptosis *(Momand et al., 1992; Finlay et al.,1993; Chen et al., 1996; Moll and Petrenko, 2003*), only recently became clear that the activation of p53 in the context of impaired ribosome biogenesis is linked to the 5S RNP free pool homeostasis. The 5S RNP is a ribonucleoprotein (RNP) complex consisting of the 5S rRNA and the ribosomal proteins Rpl5 (uL18) and Rpl11 (uL5) that

pre-assembles before the incorporation into the ribosome biogenesis pathway. In the presence of ribosome biogenesis defects due to loss-of-function mutations in ribosomal proteins, drug-dependent inhibition of ribosomal RNA synthesis or deprivation of nutrients

(Warner, 1977; Bursać et al., 2012), the 5S RNP accumulates and is re-directed from the ribosome biogenesis to the p53/Mdm2 pathway **(Fig. 19)** by binding and sequestering Mdm2 with consequent inhibition of the Mdm2-mediated ubiquitination of p53 and stabilization of p53 levels (*Bursać et al., 2012; Donati et al., 2013; Zheng et al., 2015*)**.** Remarkably, the assembly of Rpl5, Rpl11, and 5S rRNA into the 5S RNP complex continues even when ribosome biogenesis is impaired, suggesting that the formation of this pre-ribosomal particle and its accumulation upon ribosome biogenesis defects is essential to exert a fine-tuned regulation between cell proliferation and apoptosis, via its role into the MDM2/p53 pathway (*Chakraborty et al., 2011; Ajore et al., 2017).*

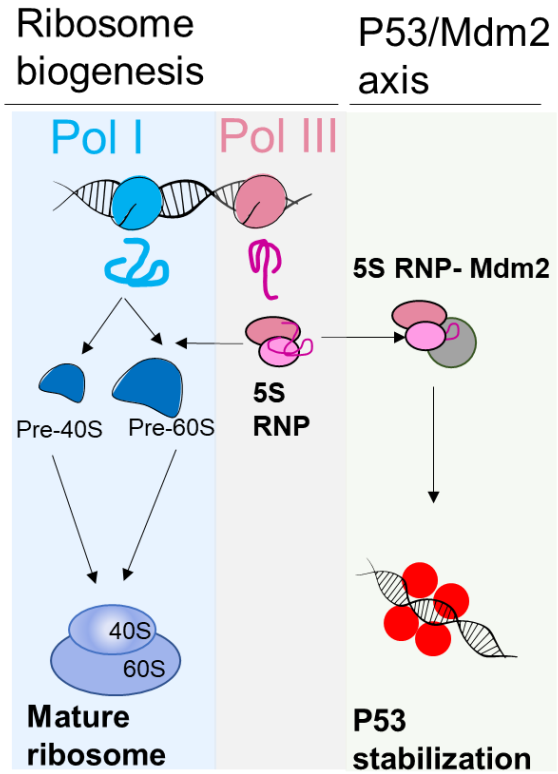

Figure 19. Model representing the 5S RNP deviating from the ribosome biogenesis to the P53/Mdm2 axis.
The 5S RNP exerts a fine tuning between cell proliferation and apoptosis. Upon defects in ribosome biogenesis, as consequence of mutations, impaired rRNA synthesis or nutrient deprivation, 5S RNP accumulates and binds to Mdm2, thus inhibiting its ubiquitin ligase activity and stabilizing p53.

1.4.3 Ribosome biogenesis is a promising target for cancer therapy

For more than 50 years, there have been only a few established treatment options for cancer patients, namely surgery, radiation therapy, and chemotherapy (*Burger et al., 2010*). In particular, chemotherapeutic agents are frequently used to kill tumour cells because of their cytotoxicity and their ability to damage DNA (genotoxicity), triggering arrest of the cell cycle and apoptosis (*Swift and Golsteyn, 2014*). However, these therapies were also found to generate elevated levels of DNA damage in healthy tissue, causing mutation and genome instability in cancer patients with consequent development of secondary therapy-induced malignancies (*Debela et al., 2021*). Fortunately, during the last decades, the knowledge regarding the pathways involved in cancer progression has dramatically increased, thus opening the door to the development of novel targeted-cancer therapies that attack, directly or indirectly, a specific genetic biomarker or pathway specific for a given cancer (*Smith and Prasad, 2021*). Among many of them, one of the targets that has been explored is the ribosome biogenesis (*Catez et al., 2019*). Notably, three are the cornerstones supporting the benefits of using ribosome biogenesis as a target for cancer therapy *(Zisi et al., 2022*). First, as extensively described above, impairing ribosome biogenesis can lead cells to p53-mediated apoptosis via the accumulation of the 5S RNP. Second, ribosome biogenesis is often increased in cancer cells, as fast-dividing cells require increased global protein synthesis *(Derenzini et al., 2017; Pelletier et al., 2018; Penzo et al., 2019*). Third, several currently used chemotherapeutic drugs, namely alkylating and intercalating agents, antimetabolites, and topoisomerase inhibitors, do not apply their broad cytotoxic effects on cancer cells only through their ability to cause DNA damage but also through the inhibition of ribosome biogenesis at different levels, such as rRNA transcription and rRNA processing *(Burger et al., 2010*; *Burger and Eick, 2013*).

For these three main reasons, efforts have been made to develop new drugs targeting ribosome biogenesis without the genotoxic effects of standard chemotherapeutic agents. In this context, since most of the mitotic signaling pathways supporting cancer cell proliferation converge on the RNA polymerase I to enable the rRNA synthesis, a rate-limiting step for ribosome biogenesis, selective molecules inhibitors of RNA polymerase I have been developed. Among them, CX-5461, CX-3543, have already entered clinical trials and may represent a novel tool for cancer therapy. Indeed, CX-

5461 is the first RNA polymerase I transcription inhibitor used for treating haematological cancer (*Khot et al., 2019*) and impairs specifically the formation of the initiation complex on the rDNA promoter (*Drygin et al., 2011*). Similarly, CX-3543 selectively disrupts nucleolin/rDNA G-quadruplex complexes that favor RNA polymerase I-mediated ribosomal DNA transcription, thereby inducing apoptosis in cancer cells (*Drygin et al., 2009*). At last, BMH-21, a small molecule that intercalates into GC-rich sequences in rDNA genes, represses RNA polymerase I transcription, and was also shown to have a potent antitumorigenic activity both *in vitro* and *in vivo (Peltonen et al., 2014; Colis et al., 2014)*. However, during the last couple of years it was suggested that these molecules may not be specific only for their primary target (*Bruno et al., 2020*). For this reason, it might be useful identifying novel compounds inhibiting additional and more specific steps of ribosome biogenesis. My work presented in this doctoral dissertation may offer an attempt to meet this demand.

2 Aim of the dissertation

During the past 20-30 years, the ribosome assembly machinery has been intensively studied in yeast, and nowadays, less is known regarding the human ribosome biogenesis pathway. Prompted by this lack of knowledge, I wanted to study the interaction of two pre-60S assembly factors, the human Rea1 and Rsa4, which is essential for the assembly of the large ribosomal subunit and have been well-characterized in yeast, with the final goal of exploiting this knowledge for the development of specific small chemical inhibitor compounds.

Prompted by that, I aimed to reconstitute the human Rea1-MIDAS-Rsa4-UBL complex and perform a thorough in vitro biochemical analysis of this interaction using a Rsa4-UBL WT and a dominant-negative rsa4-UBL mutant, already known to impair the formation of the yeast complex. Next, to understand whether the loss of this interaction upon rsa4-UBL mutant would also affect human ribosome biogenesis and cell growth, I planned to move my studies from *in vitro* to human cell cultures. Meanwhile, to find inhibitors to impair the Rea1-Rsa4 interaction specifically, I aimed to obtain a high-resolution crystal structure of this complex to be used as a base for molecular docking of small chemical compounds, which I finally intended to test in cancer cells to assess their ability to impair ribosome biogenesis and cell growth. Finally, exploiting the availability of the dominant-negative mutation in human cells, I also intended to isolate and visualize pre-60S intermediates, thus gaining novel structural information on the overall architecture of the human nucleoplasmic pre-60S.

Results

3.1 *In vitro* reconstitution of the human Rea1-MIDAS—Rsa4-UBL complex

To gain insight into the interaction between the human pre-60S factors Rea1 and Rsa4, which have been studied so far in yeast, I started my PhD work by reconstituting a minimal human (*Hs*) Rea1-MIDAS-Rsa4-UBL complex. I overexpressed and purified from *E. coli* a $(His)_6$-tagged version of the *Hs*Rea1-MIDAS domain (residues from 5287 to 5596), in which the MIDAS loop (residues from 5337 to 5381), which *in vivo,* in the case of yeast, is dispensable for the MIDAS–UBL interaction, was replaced by a short Gly-Ser-Gly linker. The other partner, the human UBL domain of Rsa4 (residues from 1 to 104), was GST-tagged to facilitate efficient purification of the complex **(Fig. 20A)**. First, I cultured, harvested, and lysed *E. coli* cells overexpressing *Hs*Rea1-MIDAS-$(His)_6$ or GST-*Hs*Rsa4-UBL, and I further centrifuged the cell lysate to separate the soluble fraction (supernatant) from the insoluble material (pellet). Next, I incubated the supernatant with Ni-NTA beads for the *Hs*Rea1-MIDAS-$(His)_6$ and Glutathione-Agarose beads for GST-*Hs*Rsa4-UBL purification, followed by extensive washing of unspecific contaminants. Next, I eluted the proteins from the beads with elution buffer, containing either 30 mM glutathione and 150 mM NaCl for the GST-*Hs*Rsa4-UBL protein or 400 mM Imidazole and 500 mM of NaCl for *Hs*Rea1-MIDAS-$(His)_6$ and further processed the samples by using size exclusion chromatography. Finally, I incubated the purified *Hs*Rea1-MIDAS-$(His)_6$ with GST-*Hs*Rsa4-UBL on glutathione-agarose beads to perform a GST-pull down assay and reconstitute the *Hs*Rea1-MIDAS-$(His)_6$-GST-*Hs*Rsa4-UBL complex on these beads. After washing the beads, I eluted the *Hs*Rea1-MIDAS$(His)_6$-GST-*Hs*Rsa4-UBL complex from the beads using glutathione elution buffer. The reconstituted *Hs*Rea1-MIDAS–*Hs*Rsa4-UBL complex was analyzed by SDS-PAGE and Coomassie staining, which revealed a 1:1 complex, according to the intensity Rea1-MIDAS and Rsa4-UBL bands **(Fig. 20B)**. Therefore, I could obtain a sufficient amount of human complex with a good degree of purity, which opened the door for subsequent structural studies and small molecule screening for chemical compounds that potentially impair the Rea1-Rsa4 complex formation

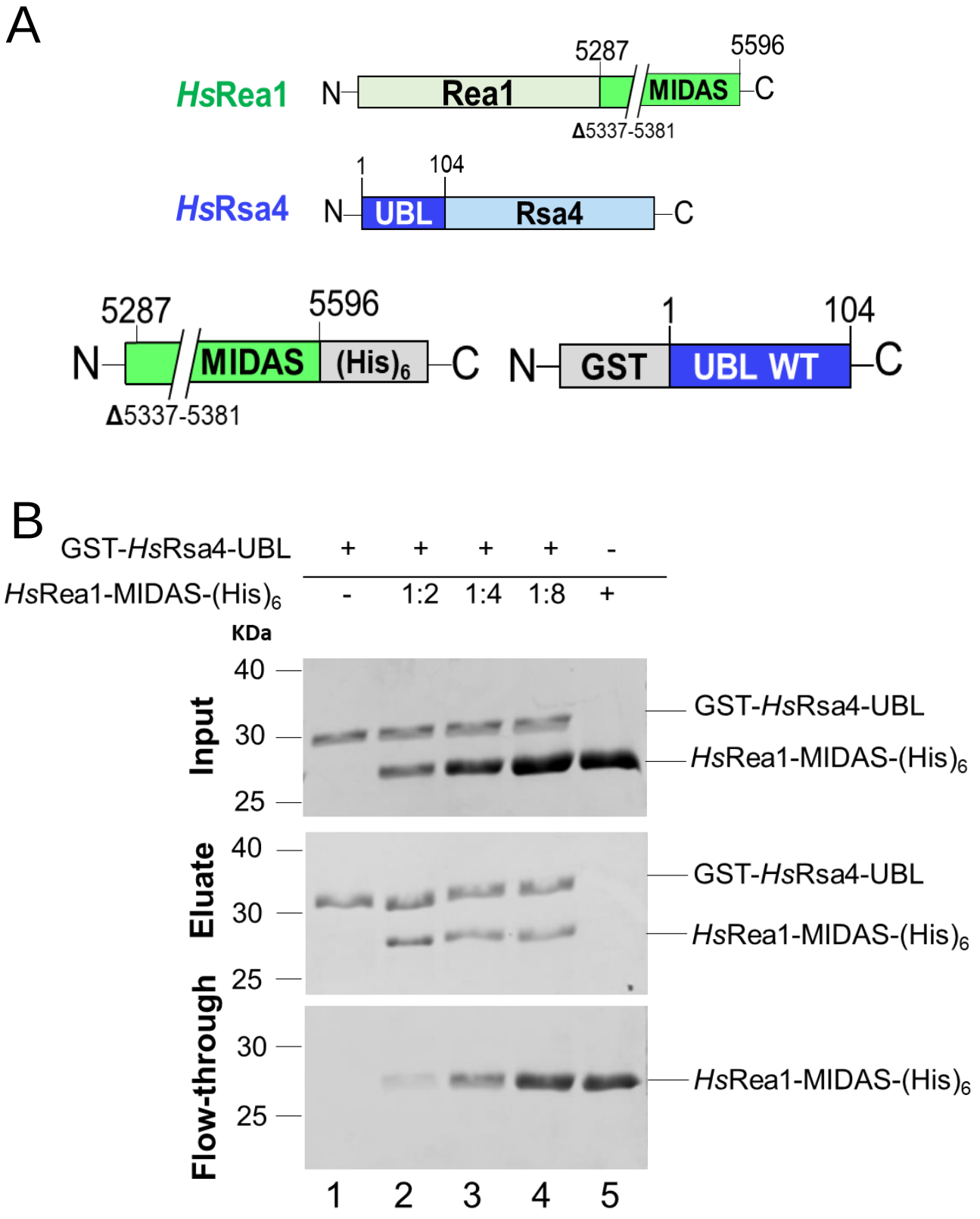

Figure 20. *In vitro* reconstitution of the Rea1-MIDAS–Rsa4-UBL complex.
A) Schematic drawing of the *Hs*Rea1-MIDAS—*Hs*Rsa4-UBL constructs used in this work. The MIDAS domain Δ loop (simply named MIDAS domain in this work) of Rea1 is shown in green and carries a C-terminal $(His)_6$ tag, which is displayed in grey; the UBL domain of Rsa4 is shown in blue and carries a N-terminal GST tag, which is displayed in grey. **B**) GST-*Hs*Rsa4-UBL was incubated on GSH-agarose beads at final concentration of 1 µM with increasing concentration of *Hs*Rea1-MIDAS-$(His)_6$ (2 µM, 4 µM and 8 µM final concentration). After incubation, the bait protein GST-*Hs*Rsa4-UBL was eluted with buffer containing glutathione, and the bound proteins were analysed by SDS-PAGE and Coomassie staining. As control both *Hs*Rea1-MIDAS-$(His)_6$ and GST-*Hs*Rsa4-UBL were incubated with beads only, in lane 1 and 5, respectively.

3.2 The human Rea1-MIDAS–Rsa4-UBL complex is displaced by an excess of untagged Rsa4-UBL

The successful reconstitution of the human *Hs*Rea1-MIDAS–*Hs*Rsa4-UBL complex *in vitro* allowed the development of further biochemical studies. Next, I tested whether it is possible to compete for the formation of *Hs*Rea1-MIDAS-$(His)_6$–*Hs*GST-Rsa4-UBL complex by adding untagged *Hs*Rsa4-UBL as a competitor ligand. Establishing this competition assay may facilitate the screening for small chemical compounds that could inhibit this interaction. For this reason, I used the same settings of the GST pull-down assay described above, but I incubated the *Hs*Rea1-MIDAS-$(His)_6$–GST-*Hs*Rsa4-UBL complex with an increasing amount of untagged competitor *Hs*Rsa4-UBL **(Fig. 21A)**.

After SDS-PAGE, followed by Coomassie-staining, I could observe a reduction in the amount of *Hs*Rea1-MIDAS-$(His)_6$ eluting with GST-*Hs*Rsa4-UBL (lanes 4-5-6) when increasing molar ratios of untagged soluble *Hs*Rsa4-UBL were added during the *in vitro* binding reaction **(Fig. 21B)**. The competition observed between GST-Rsa4-UBL and the increasing amounts of Rsa4-UBL unlabelled competitor is a good indicator that, in principle, the *Hs*Rea1-MIDAS–*Hs*Rsa4-UBL complex can be dissociated by a high-affinity inhibitor. Moreover, since the GST pull-down assay proved to be an efficient method to display the loss of *Hs*Rea1-MIDAS-$(His)_6$–*Hs*GST-Rsa4-UBL interaction, I continued to exploit it in my doctoral thesis for the further analysis of the *Hs*Rea1-MIDAS–*Hs*Rsa4-UBL complex *in vitro*.

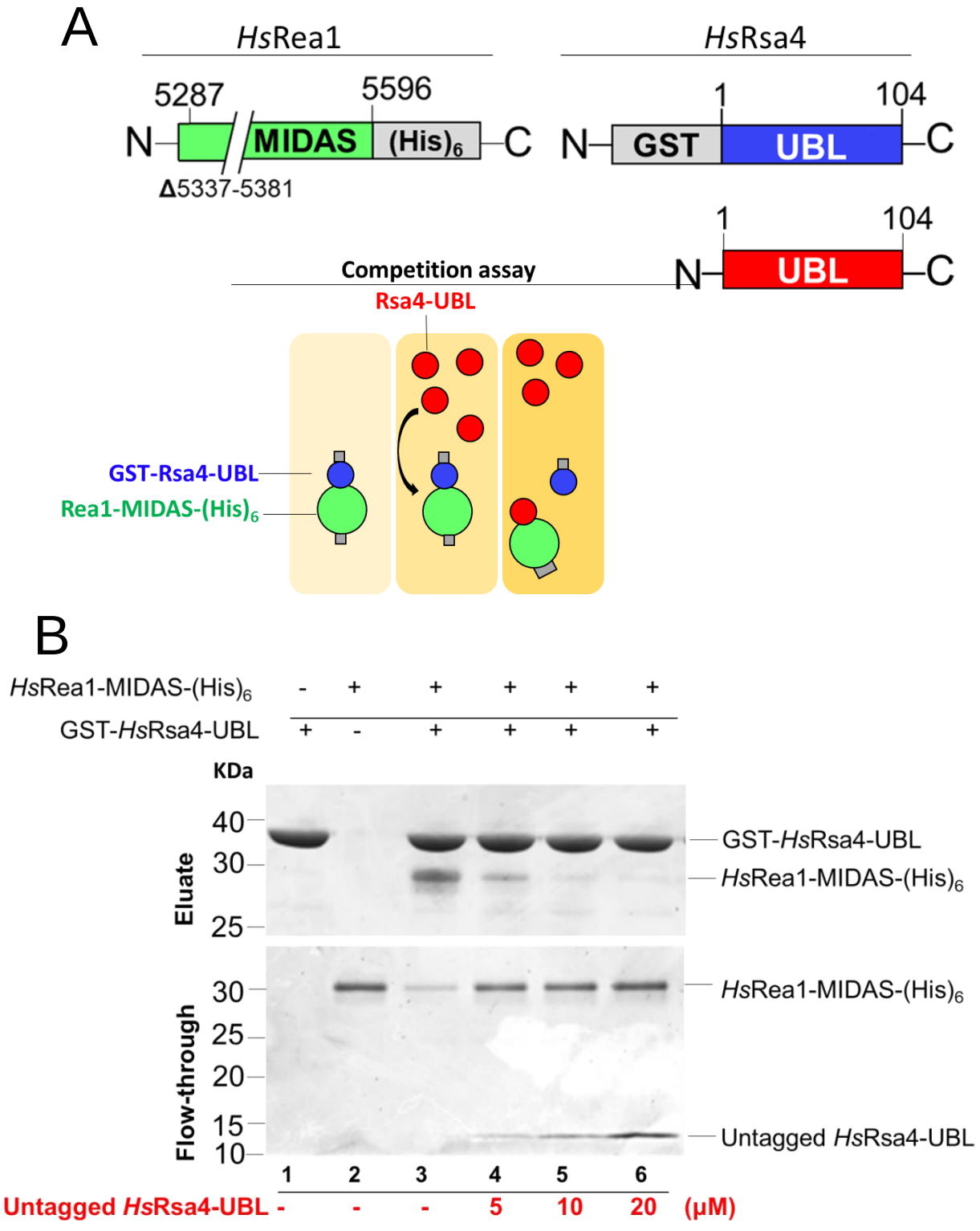

Figure 21. *Hs*Rea1-MIDAS–*Hs*Rsa4-UBL complex is competed by excess of untagged *Hs*Rsa4-UBL.
A) Schematic drawing of the constructs used in this assay and simplified scheme of the competition assay performed with the $(His)_6$-tagged MIDAS domain of Rea1, depicted in green and the GST-tagged UBL domain of Rsa4, depicted in blue, by adding excess of untagged Rsa4-UBL, shown in red. **B)** Coomassie staining of GST pull-down assay, in which glutathione agarose beads were incubated with Rea1-MIDAS-$(His)_6$ and GST-Rsa4-UBL having a final molar concentration of 1μM each, and together with increasing molar concentrations of untagged Rsa4-UBL (5 μM, 10 μM, 20 μM). After incubation, the bait protein GST-*Hs*Rsa4-UBL was eluted with buffer containing glutathione and the bound proteins were analysed by SDS-PAGE and Coomassie staining. The SDS-PAGE shows the displacement of the *Hs*Rea1-MIDAS-$(His)_6$–GST-*Hs*Rsa4-UBL complex upon titration of increasing molar ratio of untagged *Hs*Rsa4-UBL, in lane 4-5-6. Sample without the competitor was used as control, in lane 3. As control Rea1-MIDAS-$(His)_6$ and GST-Rsa4-UBL were incubated with beads only, in lane 1 and 2, respectively

3.3 Crystallization of the human Rea1-MIDAS–Rsa4-UBL complex

To facilitate the discovery of compounds impairing the human Rea1-MIDAS–Rsa4-UBL interaction, we aimed to use *in silico* structure-based methods, such as molecular modelling. As structure-based methods rely on the knowledge of the 3D structure of the protein of interest, I started several crystallization trials to solve the structure of the human Rea1-MIDAS–Rsa4-UBL interacting domains in collaboration with Prof. Sinning and her co-workers (BZH-Heidelberg University), and Dr. Kopp (Protein crystallization platform, BZH). For the crystallization trials, I used the previous *Hs*Rea1-MIDAS-$(His)_6$ construct but developed a slightly smaller new construct, a $(His)_6$-tagged version of the UBL domain of Rsa4, ranging from residue 11 to 104. To reconstitute the MIDAS–UBL complex for crystallization, I separately overexpressed and purified *Hs*Rea1-MIDAS-$(His)_6$ and $(His)_6$*Hs*Rsa4-UBL in *E.coli*, followed by mixing them in a 1:1 ratio to reconstitute the complex and then using size exclusion chromatography (SEC) as a final step to purify the complex **(Fig. 22A)**. Next, the input and the gel filtration fractions were loaded on SDS-PAGE to assess the optimal formation and quality of the complex before proceeding further **(Fig. 22B)**. The human Rea1-MIDAS–Rsa4-UBL complex was stable in gel filtration, allowing its purification in a sufficient amount and concentration (9 mg/mL) for the subsequent crystallization trials.

The initial crystallization screenings showed the formation of protein crystals whose quality was still insufficient to ensure an X-ray data collection of sufficient quality. Therefore, I carried out an optimization screening to improve some of the chemical parameters that influence the crystallization process, such as pH, ionic strength, protein concentration, and temperature. After identifying the correct buffer conditions (PEG 300 18.18%, NaAc pH 4.6, $AmSO_4$ and NH_4Cl 3.5%), crystals started to grow after 10 days and were collected after 30 days **(Fig. 22C)**.

Those high-quality crystals allowed us to solve the structure by molecular replacement using the respective *C. thermophilum* (*Ct*) complex (PDB code: 6QTA) at 2.3 Å resolution in collaboration with Dr. Klemens Wild (Sinning group).

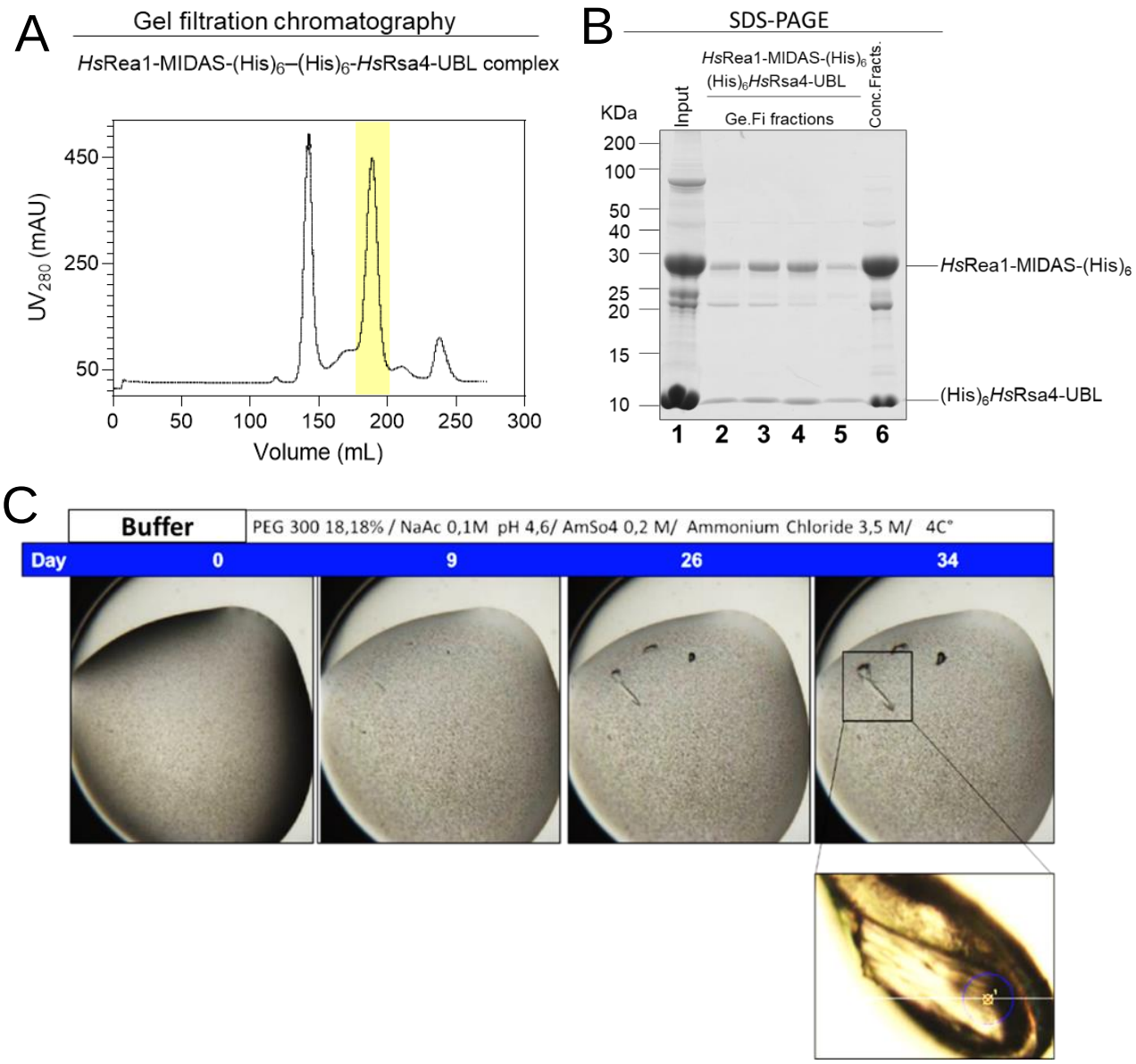

Figure 22. Crystallization process of the human Rea1-MIDAS–Rsa4-UBL complex.
A) Size-exclusion chromatography profile of *Hs*Rea1-MIDAS-$(His)_6$ and $(His)_6$*Hs*Rsa4-UBL complex. The absorbance at 280 nm (mAU) was plotted against the elution volume (mL). Absorbance peak corresponding to the fractions containing the complex are highlighted in yellow. **B)** Coomassie staining of fractions containing the *Hs*Rea1-MIDAS-$(His)_6$ and $(His)_6$*Hs*Rsa4-UBL complex. In lane 1 is loaded the gel filtration input, in lane 2-3-4-5 are loaded the gel filtration fractions containing the complex and corresponding to the absorbance peak highlighted in yellow in A, in lane 6 is loaded the reconstituted complex following concentration up to 9 mg/mL. **C**) The protein complex successfully crystallized in buffer composed of PEG 300 18.18%, NaAc pH 4.6, $AmSO_4$ and NH_4Cl 3.5% at 4 C° and images of the droplets set for crystallization screening were taken at set intervals to follow the growth of the crystals for over a month In C is also displayed a magnification of the crystal used to solve the structure of the human Rea1-MIDAS–Rsa4-UBL.

Solving the crystal structure provided the atomic details of the human Rea1-MIDAS and Rsa4-UBL domains and their interacting surface **(Fig. 23A)**. The human Rea1-MIDAS shows high structural similarity to the α-I domain of the integrins and to the Rea1-MIDAS domain of *C. thermophilum.* Indeed, similarly, the human Rea1-MIDAS domain is also characterized by the classical alpha/beta (α/β) Rossmann fold and forms, within its MIDAS consensus motif (D5391, S5393, S4795, T5465, D5495) five coordination bonds with a central Mg^{2+} ion, with the sixth coordination bond provided by the glutamate E85 of Rsa4-UBL **(Fig. 23B)**.

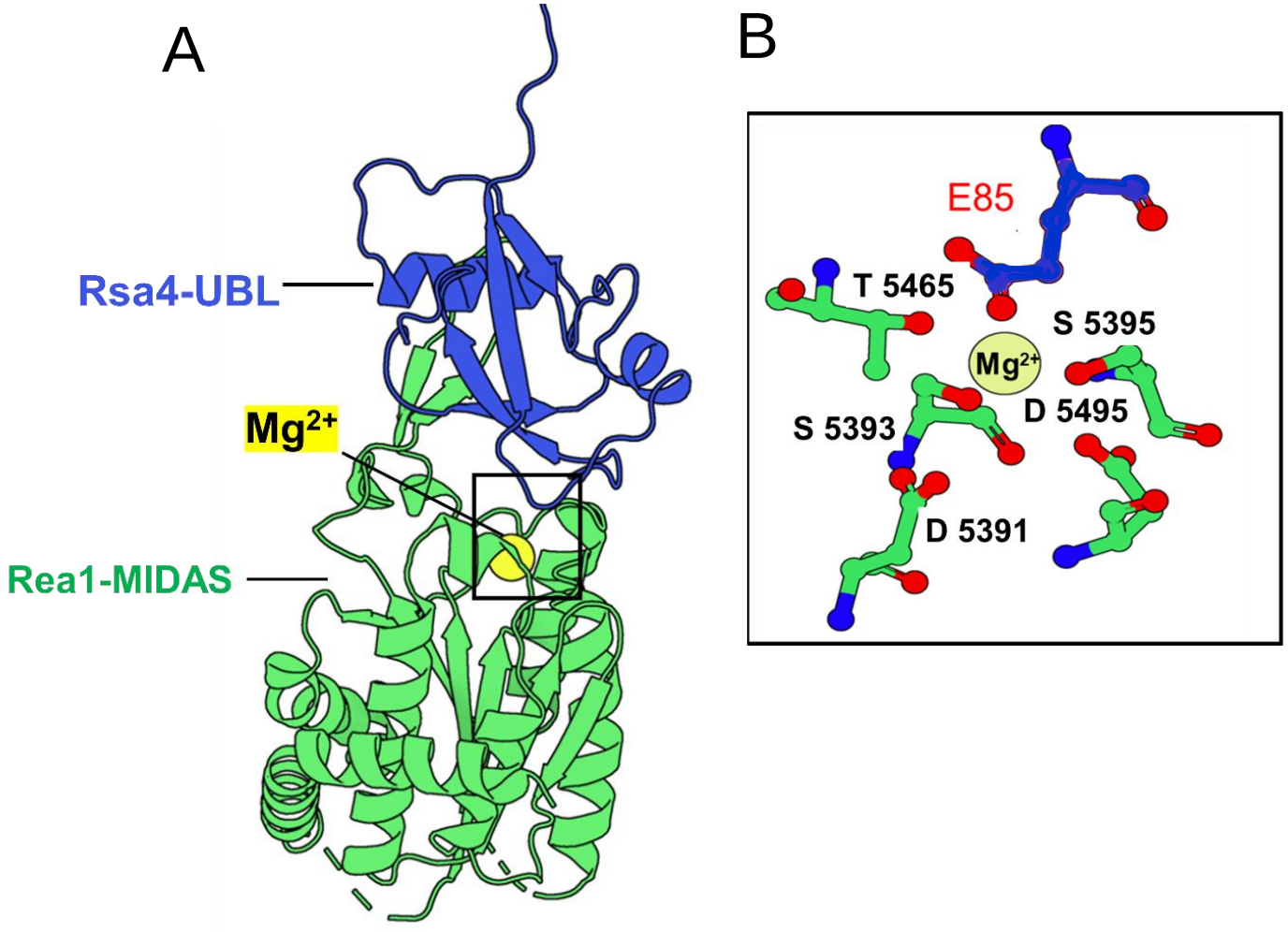

Figure 23. Crystal structure of the human Rea1-MIDAS-Rsa4-UBL complex.
A) A cartoon (or ribbon) representation of the crystal structure of the *Hs*Rea1-MIDAS domain, depicted in green in complex with the UBL domain of *Hs*Rsa4, displayed in blue. The central Mg^{2+} ion is shown in yellow. **B)** The magnification shows in green the five consensus residues (D5391, S5393, S4795, T5465, D5495) within the Rea1-MIDAS domain forming five coordination bonds with the Mg^{2+}ion. In addition, the sixth coordination bond is provided by the Rsa4-UBL domain via the glutamate E85, which is depicted in blue.

3.4 Analysis and structural comparison between the human and the *C. thermophilum* Rea1-MIDAS–Rsa4-UBL complex

In collaboration with Dr. Klemens Wild, I carried out a detailed analysis of the human Rea1-MIDAS–Rsa4-UBL complex and compared it with the structure previously solved from *C. thermophilum* (*Ahmed et al., 2019)*. Superimposition of *Hs*Rea1-MIDAS with the *Ct*Rea1-MIDAS **(Fig. 24A)** and of *Hs*Rsa4-UBL with *Ct*Rsa4-UBL **(Fig. 24B)** shows a root-mean-square deviation (RMSD) of the alpha carbon atomic coordinate (Cα) of 1.54 Å and 2.0 Å, respectively. The root mean square deviation (RMSD) is the measure of the average distance between the atoms of superimposed protein structures and is commonly used as measure of structural similarity. The smaller the RMSD is, the more similar are two structures (*Maiorov and Crippen, 1994).* Therefore, this analysis indicates that the *Hs*Rsa4-UBL and *Ct*Rsa4-UBL domains share a lower structural similarity than the MIDAS domains.

Furthermore, the superimposition could reveal interesting differences between the human and *C. thermophilum* structures. Indeed, I observed that within the *Ct*Rea1-MIDAS domain, two insertions **(Fig. 24C)** are present, which are missing in the *Hs*Rea1-MIDAS. Moreover, I also identified a significant difference in the UBL domains. Indeed, in *Ct*Rsa4-UBL the residue E117 providing the sixth coordination bond to the Mg^{2+} ion is located at the end of a half helical turn, which is missing in the human structure **(Fig. 24D**).

Further exploration of macromolecular interfaces between the MIDAS and UBL domains was carried out with the software PDBe PISA (Protein Interfaces, Surfaces and Assemblies) and revealed the measure of the area of the Rea1-MIDAS–Rsa4-UBL interaction interface and ΔG (free energy of binding) emitted upon protein-protein interaction. Upon analysis, I identified, for the human complex, an interaction area of 1200 $Å^2$, with a ΔG of -13.7 Kcal/mol, while for the *C. thermophilum* complex I obtained a value of 1071$Å^2$ interaction area with a ΔG of -9.1 Kcal/mol. Interestingly, these data suggest that the human complex may be more stable than the *C. thermophilum* one. Finally, we also carried out, both for *Hs*Rea1-MIDAS and *Hs*Rsa4-UBL, an analysis of the surface potential with PyMol **(Fig. 25)**, displaying the hydrophobic, negative and positive charged regions of the surface. Interestingly, both proteins present negative

charges within the interacting surface, which would generally create repulsive forces between the MIDAS and UBL domains. However, the presence of the Mg^{2+} ion within the MIDAS domain can neutralize the repulsive forces and create a positively charged area within the Rea1-MIDAS domain, hence attracting the negatively charged area of Rsa4-UBL.

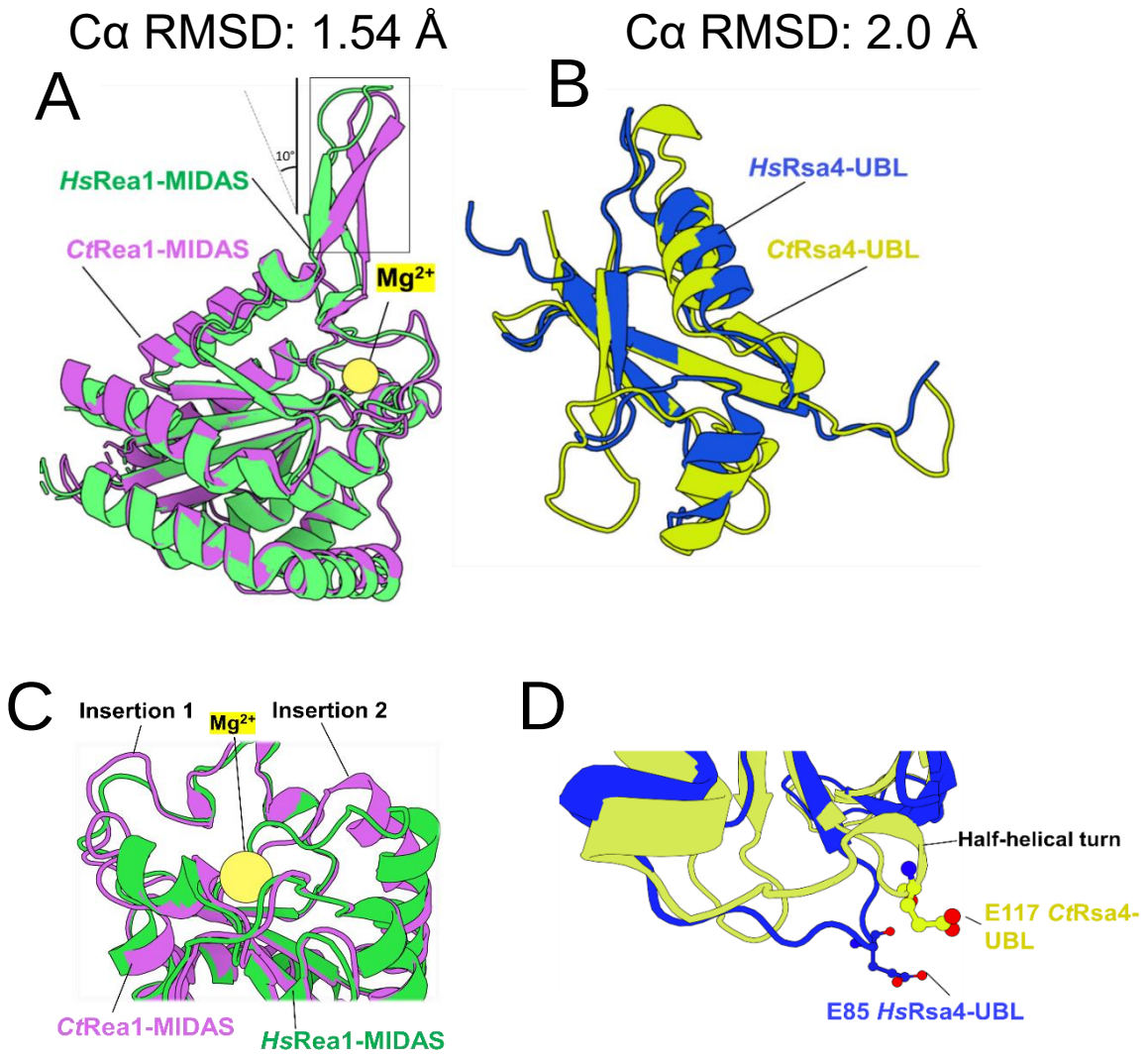

Figure 24. Superimposition and structural comparison between the human and *C. thermophilum Rea1*-MIDAS and *Rsa4*-UBL domains.
A) The *Hs*Rea1-MIDAS structure that was solved in this work is shown in green and the *Ct*Rea1-MIDAS structure (PDB code: 6QTA) is shown in violet. The two MIDAS domains superimpose well with a calculated RMSD of 1.54 Å. Interestingly, in the *Hs*Rea1-MIDAS the β-hairpine (element III, see paragraph 1.3.2 of the introduction) is rotated of 10° to the left, compared to its position in the *Ct*Rea1-MIDAS structure. **B**) The *Hs*Rsa4-UBL structure, solved in this work is shown in blue and *Ct*Rea1-MIDAS structure (PDB code: 6QTA) is shown in violet. The two UBL domains share a lower degree of structural similarity compared to the Rea1-MIDAs domains, with a calculated RMSD of 2.0 Å. **C)** Additional insertions (insertion 1 and 2) contained in the *Ct*Rea1-MIDAS and indicated with black arrows are not found in *Hs*Rea1-MIDAS. **D)** The conserved glutamate E117 coordinating the sixth bond with the Mg^{2+} ion in *C. thermophilum* is located at the similar position of the human Rsa4-UBL, but positioned after one half helical turn, not present in the human structure.

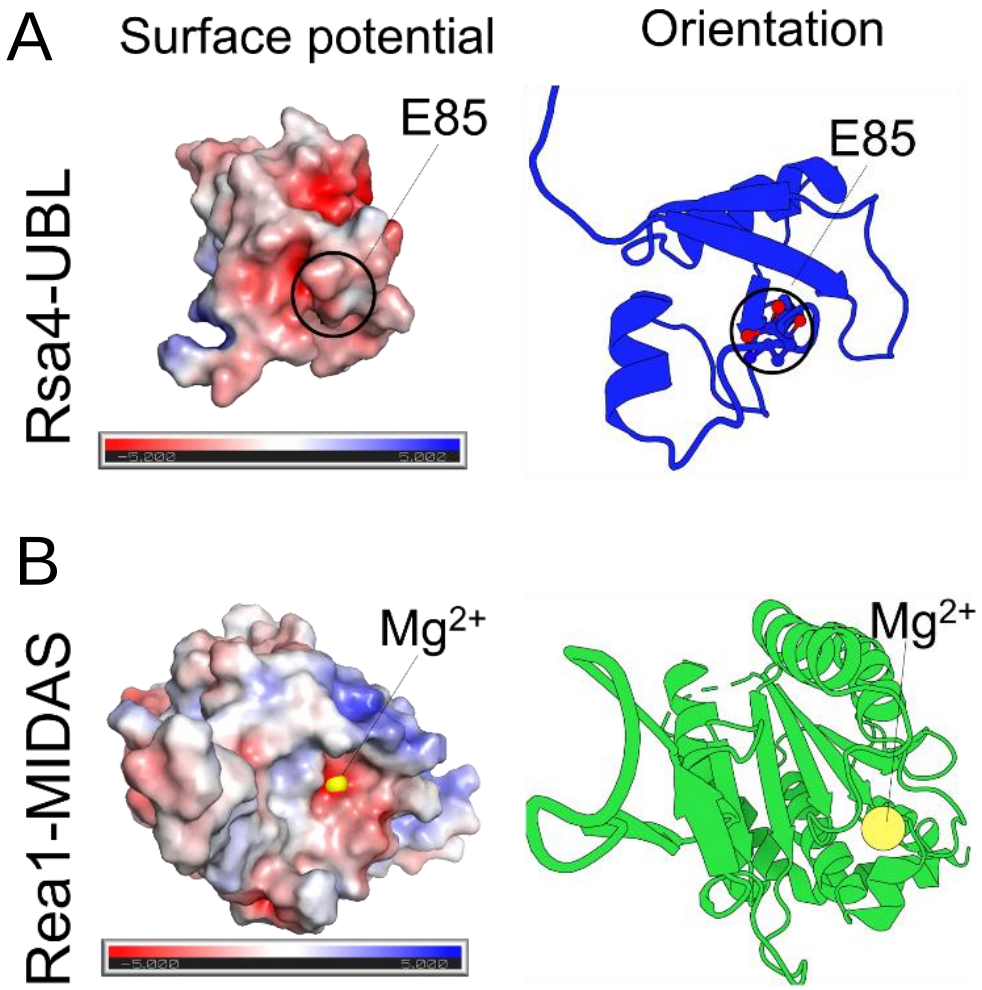

Figure 25. Electrostatic surface potential of human Rea1-MIDAS and Rsa4-UBL.
A) The analysis of the surface potential, which was carried out with PyMol −5.0 kT/e (red) to +5 kT.0 kT/e (blue), indicates the negative potential in red and the positive potential in blue. The analysis shows well defined negative charges in the Rsa4-UBL domain, in proximity of the glutamate E85 residue, coherently with its role in the coordination of the Mg^{2+} ion. **B)** The electrostatic surface potential of Rea1-MIDAS shows a larger variation, with a large positive area, in blue and a negative area, in red, which is located within the interface interacting with Rsa4-UBL. This negative area is necessary to establish the coordination bonds with the Mg^{2+} which is shown in yellow.

3.5 The E85 residue in *Hs*Rsa4-UBL is essential for the interaction with the *Hs*Rea1-MIDAS domain

Alignment of the UBL domains of Rsa4 among different species **(Fig. 26)**, showed that the residue E85 is highly conserved during evolution and corresponds to the residue E114 in *Saccharomyces cerevisiae,* which, if mutated, impairs Rea1-MIDAS–Rsa4-UBL interaction, conferring a dominant-lethal phenotype to yeast cells (*Ulbrich et al., 2009*).

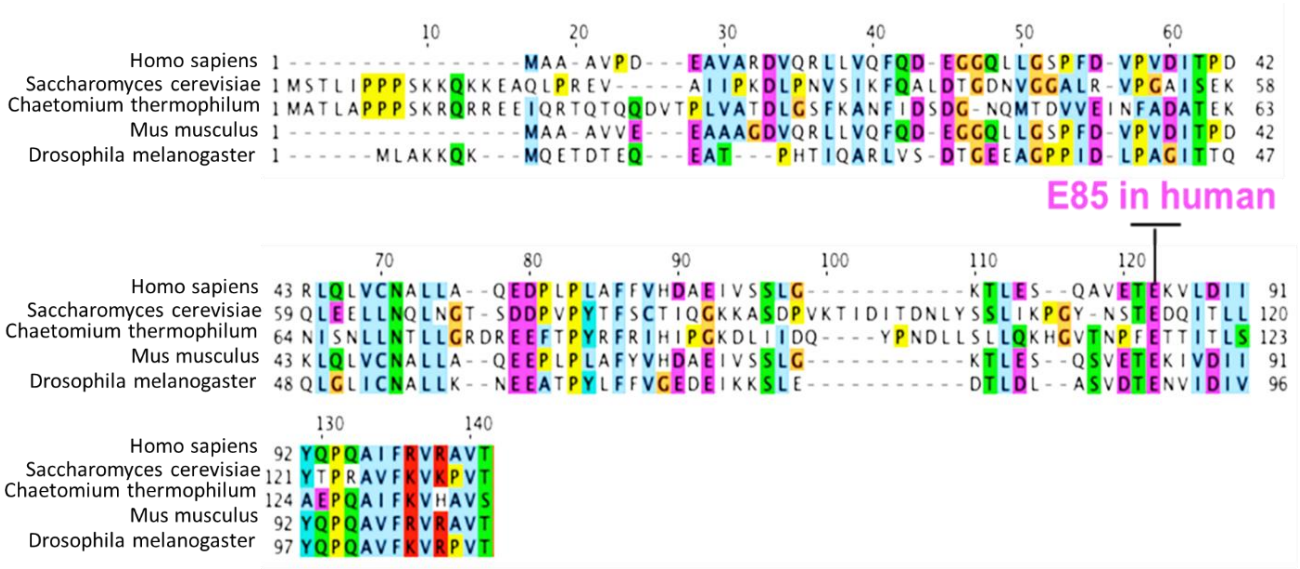

Figure 26. The acidic residue E within the UBL domain is conserved among the species. Sequences of the UBL domain of Rsa4 of *Homo sapiens*, *Saccharomyces cerevisiae*, *Chaetomium thermophilum*, *Mus musculus*, and *Drosophila melanogaster* were aligned with Clustal Omega and visualized by Jalview. The alignment shows the conservation among the species of the glutamate in position 85 (E85) of the human UBL sequence (violet).

To prove whether the mutation of the E85 residue would also disrupt the human Rea1-MIDAS–Rsa4-UBL interaction, I overexpressed and purified a new construct, a GST tagged *Hs*Rsa4-UBL, in which I mutated the E85 residue, replacing it with a lysine (E85K). First, I performed the above described *in vitro* binding assay between *Hs*Rea1-MIDAS-$(His)_6$ and GST-*Hs*Rsa4-UBL WT and E85K, respectively **(Fig. 27A)**. As expected, I observed that while the *Hs*Rea1-MIDAS was efficiently binding to GST-*Hs*Rsa4-UBL WT **(Fig. 27B,** lane **4)**, the replacement of the glutamate with a lysine (E85K) of the UBL domain of *Hs*Rsa4 abolished the complex formation **(Fig. 27B,** lane **5)**.

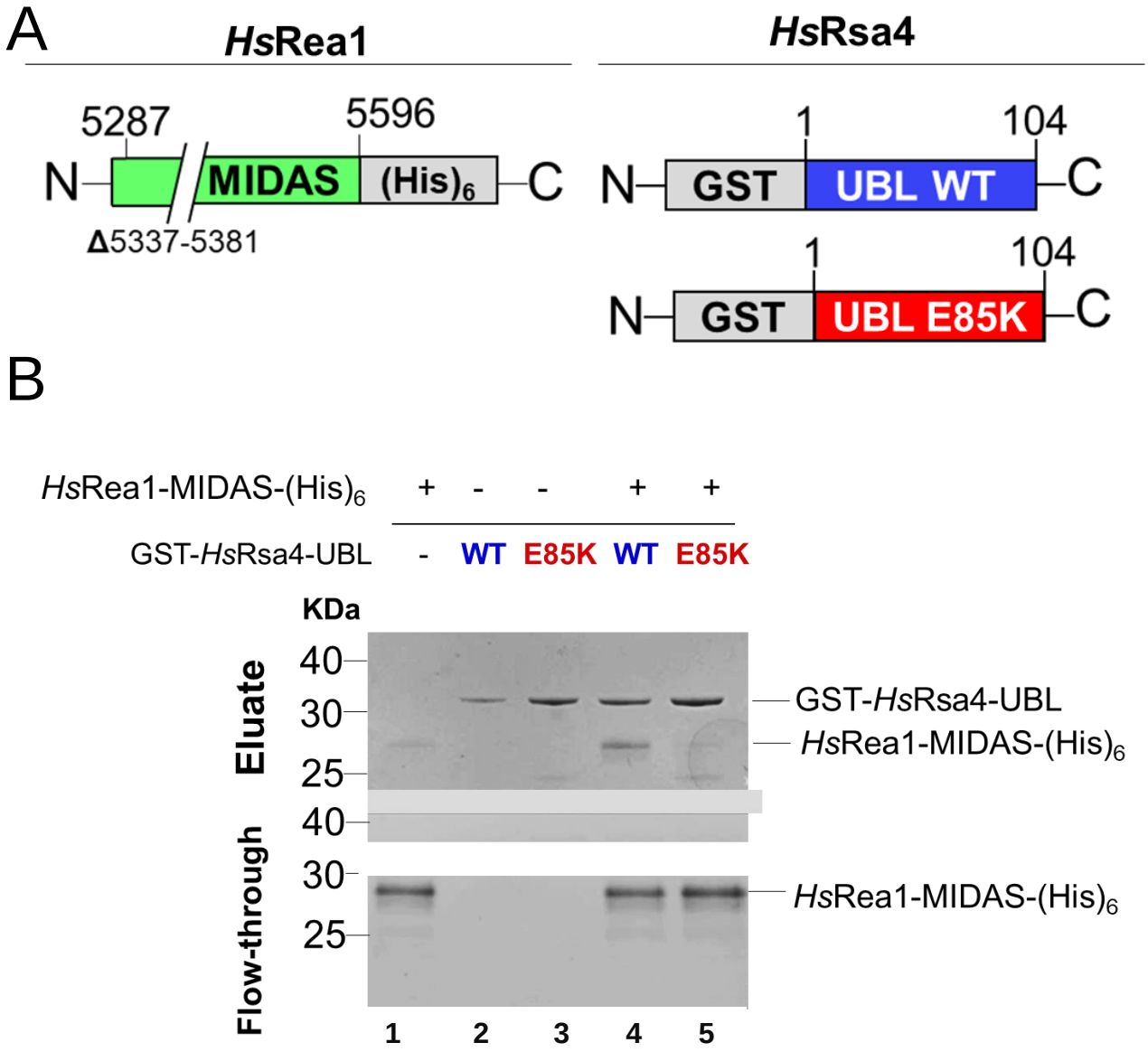

Figure 27. Mutation of the conserved residue E85 (E>K) impairs the binding between human Rea1-MIDAS and Rsa4-UBL.
A) Schematic drawing of the constructs used in this assay. *Hs*Rea1-MIDAS-$(His)_6$ is depicted in green, GST-Rsa4-UBL WT is in blue, and GST-rsa4-UBL E85K is shown in red. **B**) GST pull-down assay in which *Hs*Rea1-MIDAS-$(His)_6$ was incubated on glutathione agarose beads at 2 µM final concentration with either GST-*Hs*Rsa4-UBL WT (1 µM final concentration) in lane 4 or GST-*Hs*rsa4-UBL E85K (1 µM final concentration) in lane 5. After incubation, the bait proteins GST-*Hs*Rsa4-UBL WT and E85K were eluted with buffer containing glutathione and bound proteins were analysed by SDS-PAGE followed by Coomassie staining. As control *Hs*Rea1-MIDAS-$(His)_6$, GST-*Hs*Rsa4-UBL WT, and GST-*Hs*Rsa4-UBL E85K were incubated with beads only and loaded in lanes 1,2, and 3, respectively.

To obtain quantitative data on the binding constant between *Hs*Rea1-MIDAS and *Hs*Rsa4-UBL of either WT or mutant conditions, I used an isothermal titration calorimetry assay (ITC), in which I titrated increasing amounts of *Hs*Rsa4-UBL WT or E85K mutant with a fixed concentration of *Hs*Rea1-MIDAS. The ITC revealed that *Hs*Rsa4-UBL WT binds *Hs*Rea1-MIDAS with high affinity, with a dissociation constant (K_D) value in the low nanomolar ranges (~5 nM) **(Fig. 28A)**; by contrast and in agreement with the previous result, the ability of the *Hs*rsa4-UBL E85K to bind *Hs*Rea1-MIDAS was strongly impaired, so that a K_D value could not be obtained **(Fig. 28B).**

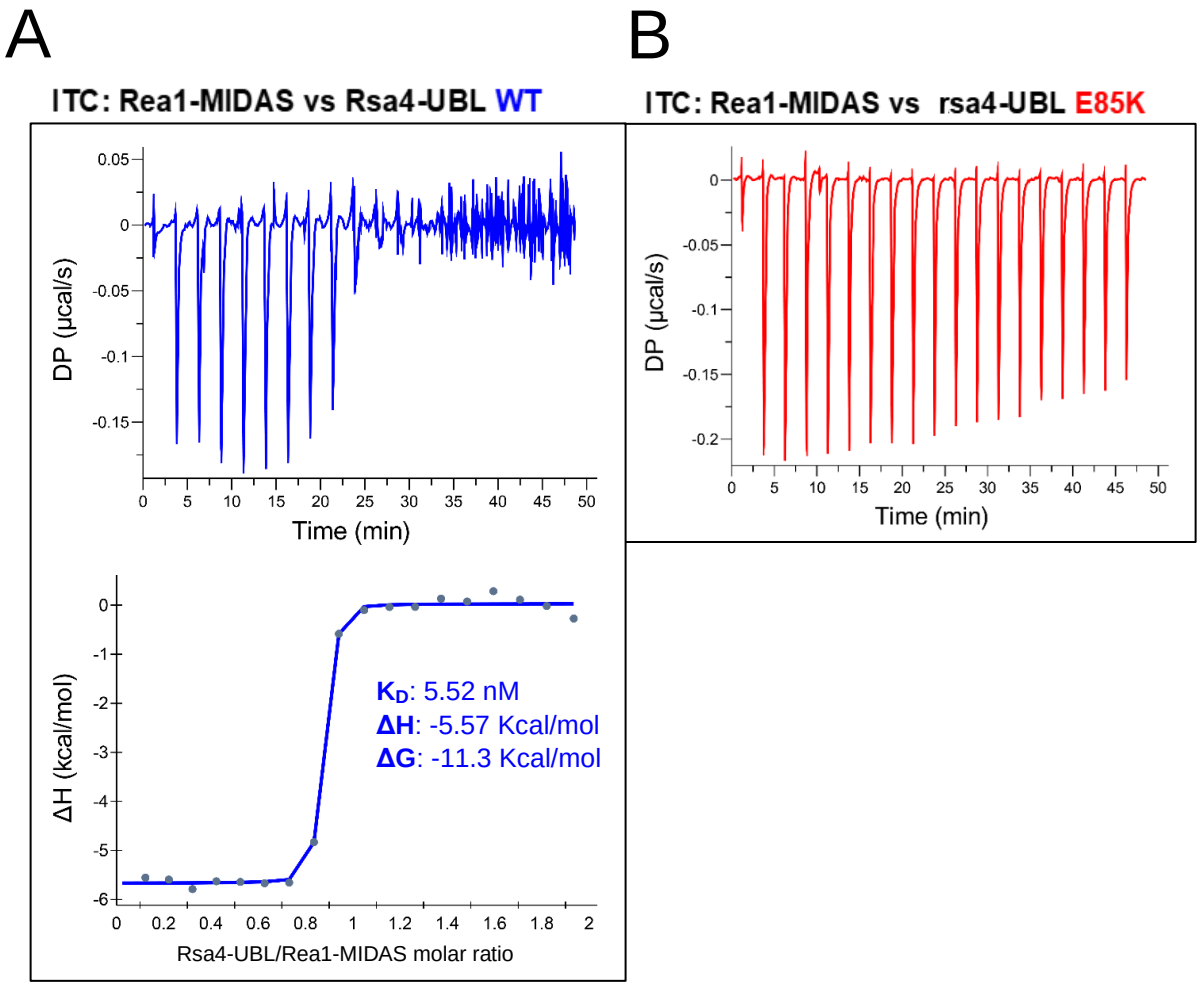

Figure 28. The human Rea1-MIDAS–Rsa4-UBL is a high affinity protein-protein interaction.
A) ITC measurement of Rea1-MIDAS with Rsa4-UBL WT. The left-upper panel shows the heat released over time upon titration of Rea1-MIDAS with increasing amount Rsa4-UBL WT. During the reaction Rea1-MIDAS binding sites are getting saturated, with consequent reduction of the heat released, shown in blue. The heat released over time is then plotted as binding curve, displayed in blue in the left-bottom panel. The binding curve allows the determination of binding stoichiometry, the K_D (the dissociation constant), the ΔG (Gibbs energy) and ΔH (enthalpy). The graph in figure is representative of three experiments. **B**) Representation of the heat released during titration of Rea1-MIDAS with increasing amount of rsa4-UBL E85K. The mutant rsa4-UBL E85K does not saturate Rea1-MIDAS binding sites, therefore it was not possible to obtain any binding curve.

3.6 Abrogation of the Rea1-MIDAS–Rsa4-UBL interaction impairs human cell growth

Having shown that the human Rea1-MIDAS–Rsa4-UBL interaction can be disturbed *in vitro* by mutating the critical residue E85>K within Rsa4-UBL, I wanted to analyze now this effect in human cells. To this end, HEK293 cells stably expressing full-length Rsa4 protein WT or E85A mutant and carrying a 3x FLAG tag at the N-terminus were cloned under the control of the TET-On promoter (established in collaboration with the Beckmann lab, Gene Center Munich).

In a first test, I wanted to investigate the ability of these cells to proliferate upon overexpression of the rsa4-UBL E85A mutant. To do so, I performed an analysis of cell confluence in which I cultured rsa4-UBL E85A cells and Rsa4-UBL WT cells for 5 days in a medium with or without doxycycline to induce the overexpression of the constructs. Next, I stained the cells with crystal violet, which enabled the visualization of cell colonies by staining the nuclei with a purple color. As expected, in cells induced with doxycycline and overexpressing Rsa4-UBL WT, I did not observe any difference in cell number compared to cells with uninduced expression Rsa4-UBL WT **(Fig. 29A)**. By contrast, cells overexpressing rsa4-UBL E85A mutant displayed a significant impairment of cell growth compared to cells with uninduced rsa4-UBL E85A, or cells overexpressing Rsa4-UBL WT **(Fig. 29B)**. These data suggest that mutation of the key residue E85 within the UBL domain of Rsa4, which *in vitro* inhibits the binding to Rea1-MIDAS (see paragraph 3.5), exerts a dominant-negative effect on human cells growth.

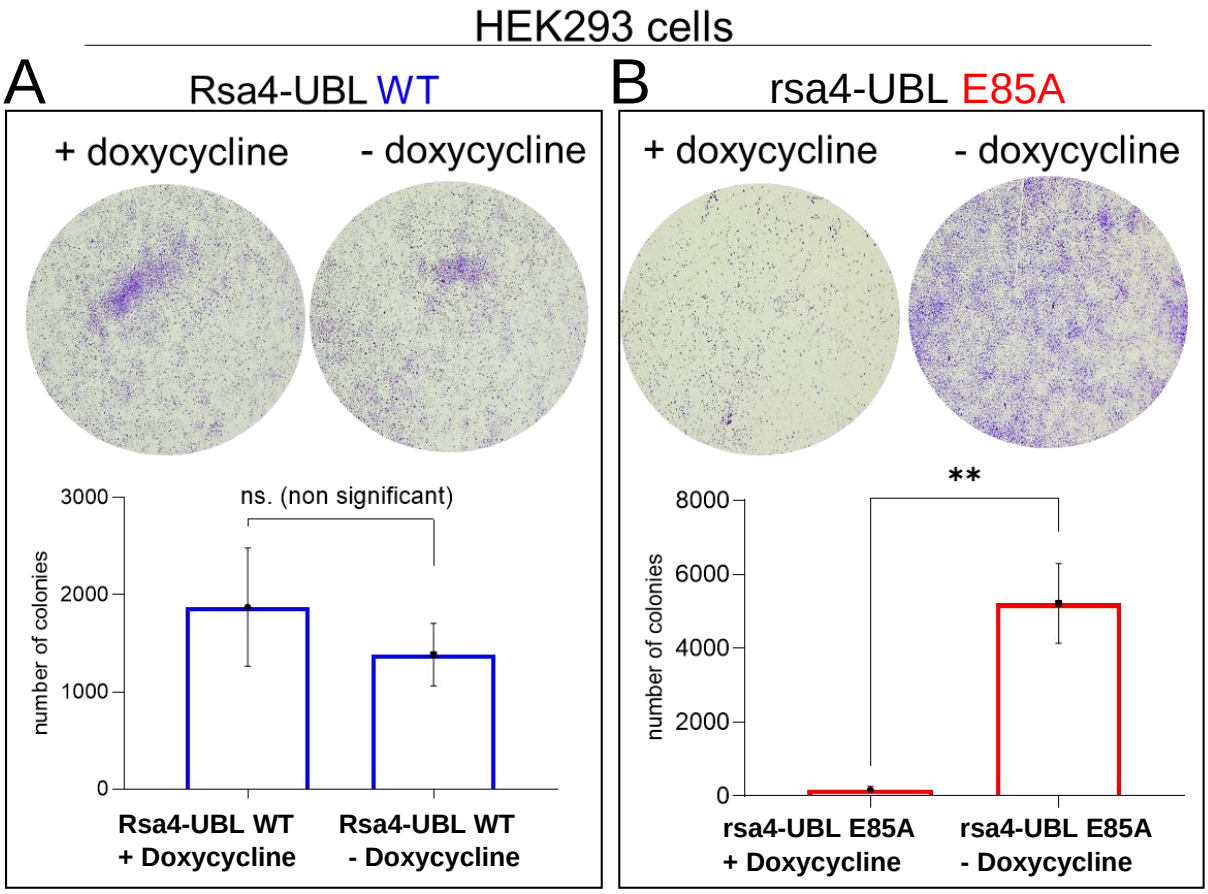

Figure 29. The rsa4-UBL dominant-negative mutant E85A inhibits HEK293 cell growth.
A) The colony formation assay performed on HEK293 Rsa4-UBL WT cells with and without doxycycline induction. Cell colonies were visualized by staining with crystal violet and the number of cells was quantified and then reported in the blue bar graph (bottom panel) as mean of three experiments. **B**) The colony formation assay was performed in HEK293 rsa4-UBL E85A cells with and without doxycycline induction. Cells overexpressing rsa4-UBL E85A show reduced cell number compared to uninduced cells. Cell colonies were visualized by staining with crystal violet and the number of cells was quantified and then reported in the red bar graph (bottom panel) as mean of three experiments. In both graphs, error bars represent standard deviation of three independent experiments. An unpaired *t* test was conducted to assess statistical significance (ns, not significant; *, $p < 0.05$).

3.7 Overexpression of rsa4-UBL E85A in human cells leads to cell cycle arrest and apoptosis

After demonstrating that the overexpression of rsa4-UBL E85A mutant reduced cell growth, I wanted to understand what caused it. Indeed, this phenotype could be due to a primary defect, namely the inhibition of pre-60S biogenesis, followed by secondary effects conveying on other signalling pathways. To understand that I performed a western blot analysis to test whether factors involved in the cell cycle and apoptosis were affected, thus explaining the reason behind the impairment of the cell growth. Therefore, I overexpressed Rsa4-UBL WT or E85A in HEK293 cells for 24, 48 and 72 hours upon doxycycline induction and evaluated the expression levels of the human

ribosome biogenesis regulator, c-Myc, the cell cycle regulator, cyclin-D1, and the pro-apoptotic protein, cleaved caspase-3. Upon 24 and 48 hours of rsa4-UBL E85A overexpression, non-significant change in the expression levels of c-Myc, cyclin-D1, and cleaved caspase-3 was detected (*data not shown*). However, the overexpression of rsa4-UBL E85A for 72 hours led to increased expression levels of the pro-apoptotic marker, cleaved caspase-3, and decreased expression levels of cyclin D1 and c-Myc compared to cells overexpressing Rsa4-UBL WT or uninduced cells **(Fig. 30A)**. These data indicate that upon rsa4-UBL E85A overexpression occurs the stop of the cell cycle, which could be explained by a reduction of the cyclin D1 and the oncogene c-Myc, and the initiation of the apoptotic cascade, which is suggested by the increase of the cleaved caspase-3. Next, I carried out a cell viability assay to further assess the viability of cells upon overexpression of rsa4-UBL E85A. To do so, I measured the viability of cells overexpressing Rsa4-UBL WT or E85A after 72 hours of doxycycline induction, using the CellTiter-Blue assay **(Fig. 30B)**. CellTiter-Blue, also called resazurin, is a redox indicator that gets metabolized by living cells into resorufin, a fluorescent product. While viable cells can reduce resazurin by generating a fluorescent signal, non-viable cells rapidly lose metabolic capacity and do not reduce resazurin. In agreement with the previously obtained data, the viability of cells overexpressing rsa4-UBL E85A was reduced by more than 50% compared to Rsa4-UBL WT cells and rsa4-UBL E85A uninduced cells. In conclusion, these data show that the rsa4-UBL E85A mutation has a potent effect on cell growth and cell viability, possibly due to impaired ribosome biogenesis.

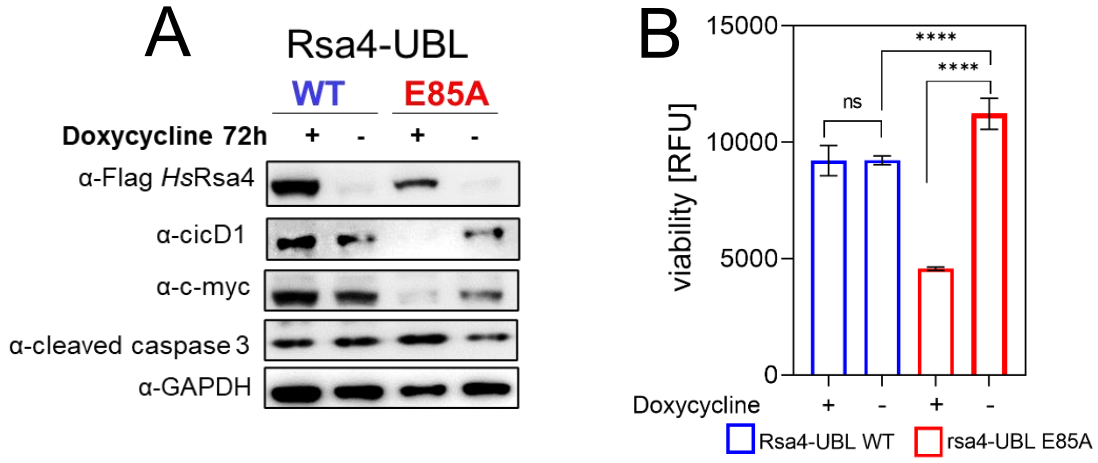

Figure 30. The impairment of the human Rea1-MIDAS-Rsa4-UBL complex triggers apoptosis and blocks cell cycle in HEK293 cells.
A) Western blot analysis at 72 hours of FLAG Rsa4-UBL, c-Myc, cyclin D1 and cleaved caspase-3 protein levels in doxycycline-induced or uninduced Rsa4-UBL WT and E85A cells. GAPDH was used as loading control. **B**) Viability assay based on CellTiter-Blue was used to evaluate the viability of Rsa4-UBL WT and E85A after 72 hours of induction with doxycycline. rsa4-UBL E85A induced cells viability was significantly reduced compared to the controls Rsa4-UBL WT and rsa4-UBL E85A uninduced cells. Error bars represent standard deviation of three independent experiments. An unpaired *t* test was conducted to assess statistical significance (ns, non-significant; ****, $p < 0.0001$).

3.8 The mutant rsa4-UBL E85A impairs 60S ribosome assembly in human cells

To determine whether the dominant-negative phenotype observed upon overproduction of rsa4-UBL E85A affects pre-ribosome maturation, I transiently transfected HEK293 cells overexpressing Rsa4-UBL WT or rsa4-UBL E85A the ribosomal reporter protein Rpl29, tagged with GFP (Wild et al., 2010), to analyze its subcellular localization by confocal microscopy. Indeed, Rpl29 is typically associated with the mature 60S subunit in the cytoplasm, with only marginal staining in the nucleoli but it accumulates in the nuclear compartment following defects in the pre-60S assembly pathway.

In agreement with that, in cells overexpressing Rsa4-UBL WT, Rpl29-GFP retained its normal distribution in the cytoplasm, with a less prominent localization in the nucleoli, indicating that a correct ribosomal export was occurring. Conversely, in cells overexpressing rsa4-UBL E85A, the signal of Rpl29-GFP strongly accumulated in the nucleus, while the cytoplasmic signal was largely reduced **(Fig. 31A-B)**. As a control, I also analyzed the localization of Rpl29-GFP in Rsa4-UBL WT and rsa4-UBL E85A cells without doxycycline induction, which, as expected, remained unaltered **(Fig. 31A-B)**. These data suggest that the dominant-negative rsa4-UBL E85A mutant blocks the progression of the nascent pre-60S subunit.

Next, to demonstrate that the E85A mutation within Rsa4-UBL specifically affects the 60S but not the 40S assembly pathway, I analyzed the localization of another ribosomal reporter protein, Rps2-YFP, via confocal microscopy (*Wild et al., 2010*). Rps2 is associated with the 40S subunit and localizes in the cytoplasm. However, it can accumulate in the nucleus upon inhibition of the 40S assembly pathway (*Zemp et al., 2009*).

Following transfection of Rps2-YFP in cells overexpressing Rsa4-UBL WT and E85A, the reporter protein Rps2-YFP always retained its normal cytoplasmatic localization, indicating that rsa4-UBL E85A mutation affects specifically the nuclear export of the pre-60S particles, but not the one of the pre-40S particles **(Fig. 31C).**

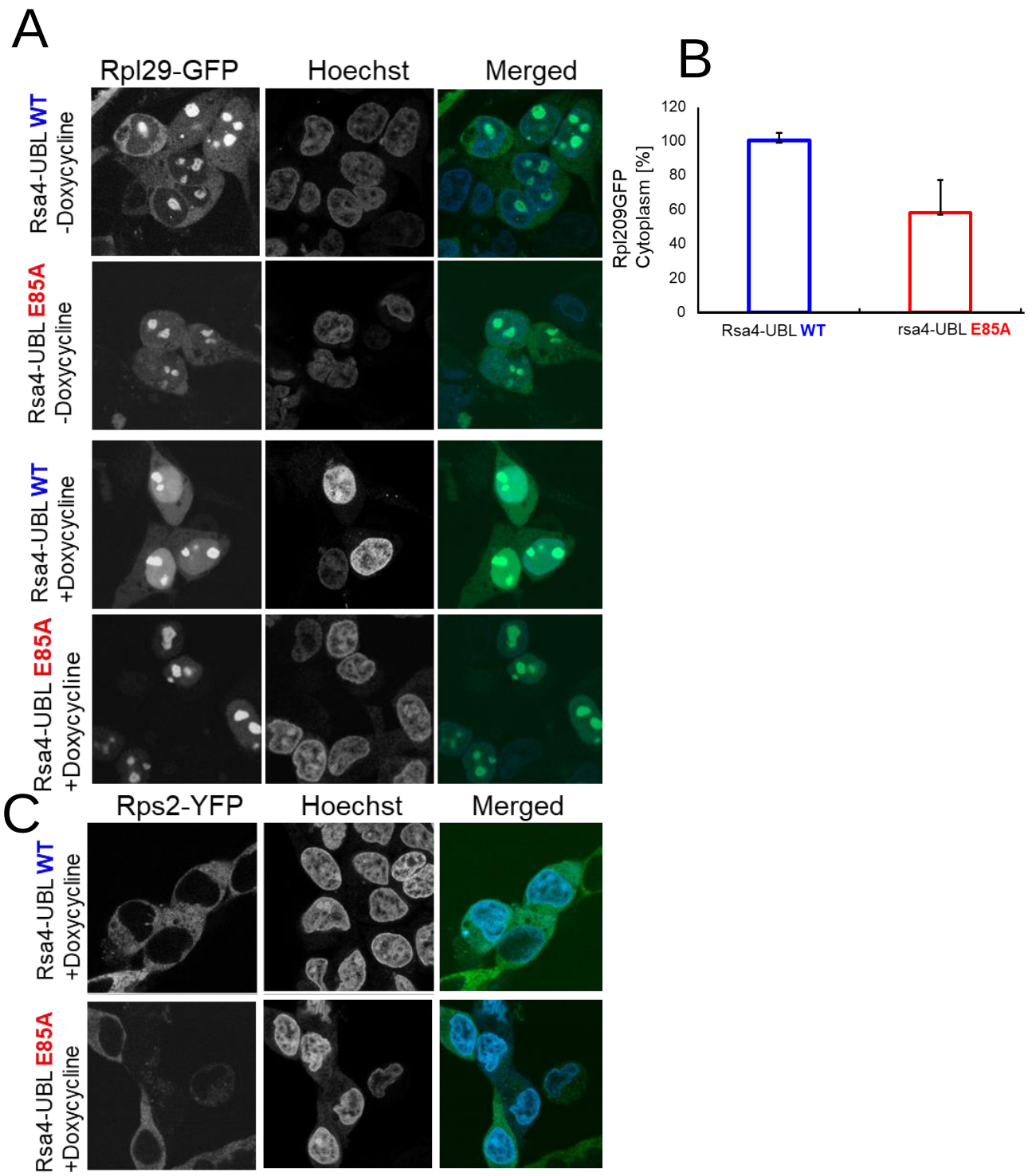

Figure 31. The mutant rsa4-UBL E85A impairs the nuclear export of the pre-60S ribosomal particle, while the export of the pre-40S is not affected.

A) Confocal microscopy monitoring the subcellular localization of Rpl29-GFP in Rsa4-UBL WT and E85A cells induced with doxycycline and uninduced. Nuclei are counterstained with Hoechst. Wild-type and mutant cells induced and uninduced are imaged according to the same setting: 800V, 1.5X zoom, 60x oil objective. **B**) Quantification of the GFP signal in the cytoplasm of cells overexpressing Rsa4-UBL WT versus cells overexpressing rsa4-UBL E85A. The plotted values are obtained from 15 different images of two independent experiment. **C**) Confocal microscopy monitoring the subcellular localization of Rps2-GFP in Rsa4-UBL WT and E85A cells induced with doxycycline and uninduced. Nuclei are counterstained with Hoechst. Wild-type and mutant cells are imaged according to the same setting: 900V, 1.5X zoom, 60x oil objective.

Next, to further demonstrate that the 60S biogenesis is inhibited upon overexpression of the dominant-negative rsa4-UBL E85A mutant, we performed sucrose gradient centrifugation with cell lysate to separate the 40S, 60S, 80S, and polysomes (in collaboration with Matthias Thoms, Beckmann Lab, Gene center Munich) **(Fig. 32)**. In the polysome analysis of Rsa4-UBL WT cell lysate, the mature 80S monosomes-representing peak is the most prominent portion of the profile, with the 40S and 60S-representing peaks having equal size. However, upon overexpression of rsa4-UBL E85A, we could assist in a reduction of the mature 60S-representing peak, accumulation of the 40S subunits-representing peak, and the appearance of half-mer polysomes in the cytoplasm. The accumulation of half-mer reflects a defect in during the coupling of the large 60S subunit with the small 40S subunit, occurring when the level of 60 S subunits is limiting. Therefore, the polysome analysis clearly suggests that the rsa4-UBL E85A mutant efficiently blocks the assembly of the pre-60S particles.

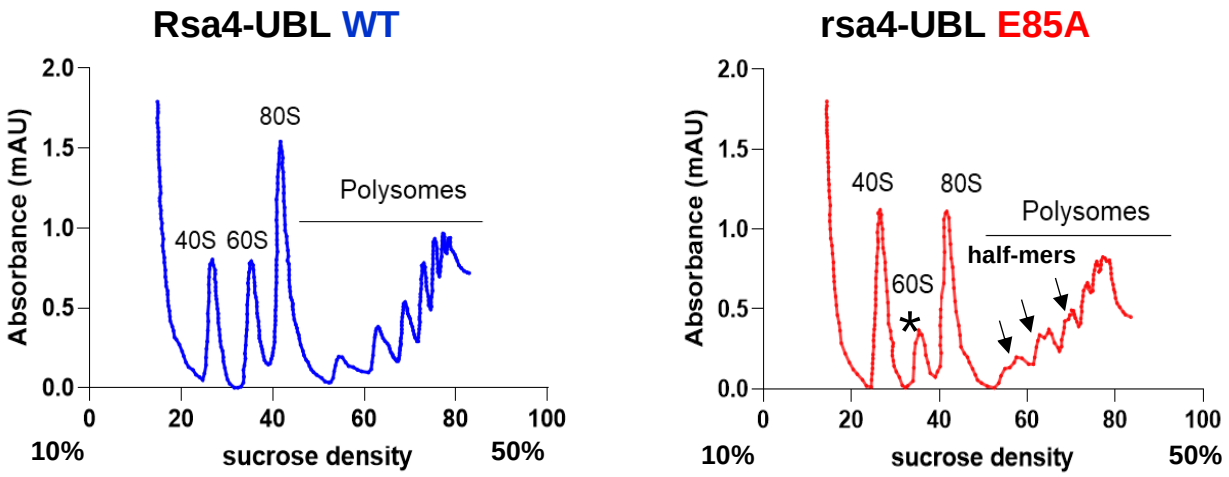

Figure 32. rsa4-UBL E85A mutant impairs the assembly of the 60S ribosomal subunit.
Polysome analysis of Rsa4-UBL WT and rsa4-UBL E85A cells induced for six hours with doxycycline. Whole cell lysates were separated by ultracentrifugation on a linear sucrose gradient (from 10% to 50% sucrose density) and the UV profile was recorded at 254 nm. The migration of the 40S, 60S and 80S is labelled accordingly. The 60S-representing peak, which in rsa4-UBL E85A is reduced, is labeled with an asterisk. Half-mers appearing in rsa4-UBL E85A are also labeled with black arrows.

3.9 Overexpression of rsa4-UBL E85A allows purification of a human nucleoplasmic pre-60S assembly intermediate

Since, in the rsa4-UBL E85A cells, both cell growth and the assembly of the 60S ribosome subunit were impaired, we wanted to test whether pre-60S particles could be purified from these cells. In the past, it was not possible to purify pre-60S particles from the nucleolus and nucleoplasm, respectively, for reasons which may have to do with the structure of the nuclei.

Therefore, I tried to use the inducible 3xFLAG-tagged rsa4-UBL E85A dominant-negative mutant to block the maturation of pre-60S ribosomal particles, thus allowing the affinity purification of pre-60S intermediates stalled in their nucleoplasmic maturation stage. I performed a single-step FLAG-purification using 3x FLAG-tagged Rsa4-UBL WT and E85A constructs overexpressed in human cells in either induced and uninduced conditions. After the purification, I analyzed the final FLAG eluates by SDS-PAGE followed by Coomassie staining **(Fig. 33A)** and the bait protein Rsa4 was identified by both mass-spectrometry and Western blot analysis. The purification did not reveal a significant enrichment of pre-60S assembly factors in the Coomassie-stained SDS-page gel, thus it prompted me to analyze the final FLAG eluates by the more sensitive semi-quantitative mass spectrometry (SQ-MS). Upon SQ-MS I could compare both preparations directly by normalizing the obtained LFQ (Label-free quantification) values of rsa4-UBL E85A versus Rsa4-UBL WT **(Fig. 33B)**. This quantification revelated that the FLAG-eluate of rsa4-UBL E85A was clearly enriched in typical pre-60S assembly factors, such as Sda1, Nsa2, Nog1 and 2, Nop2, IF6, rea1, the Rpf2 and Rrs1 heterodimer, Rpl5, and Rpl11, which are part of the 5S RNP, assembly factors being part of foot structure, such as Rpl7, Nop53 and NIFK (Nop15 in yeast).

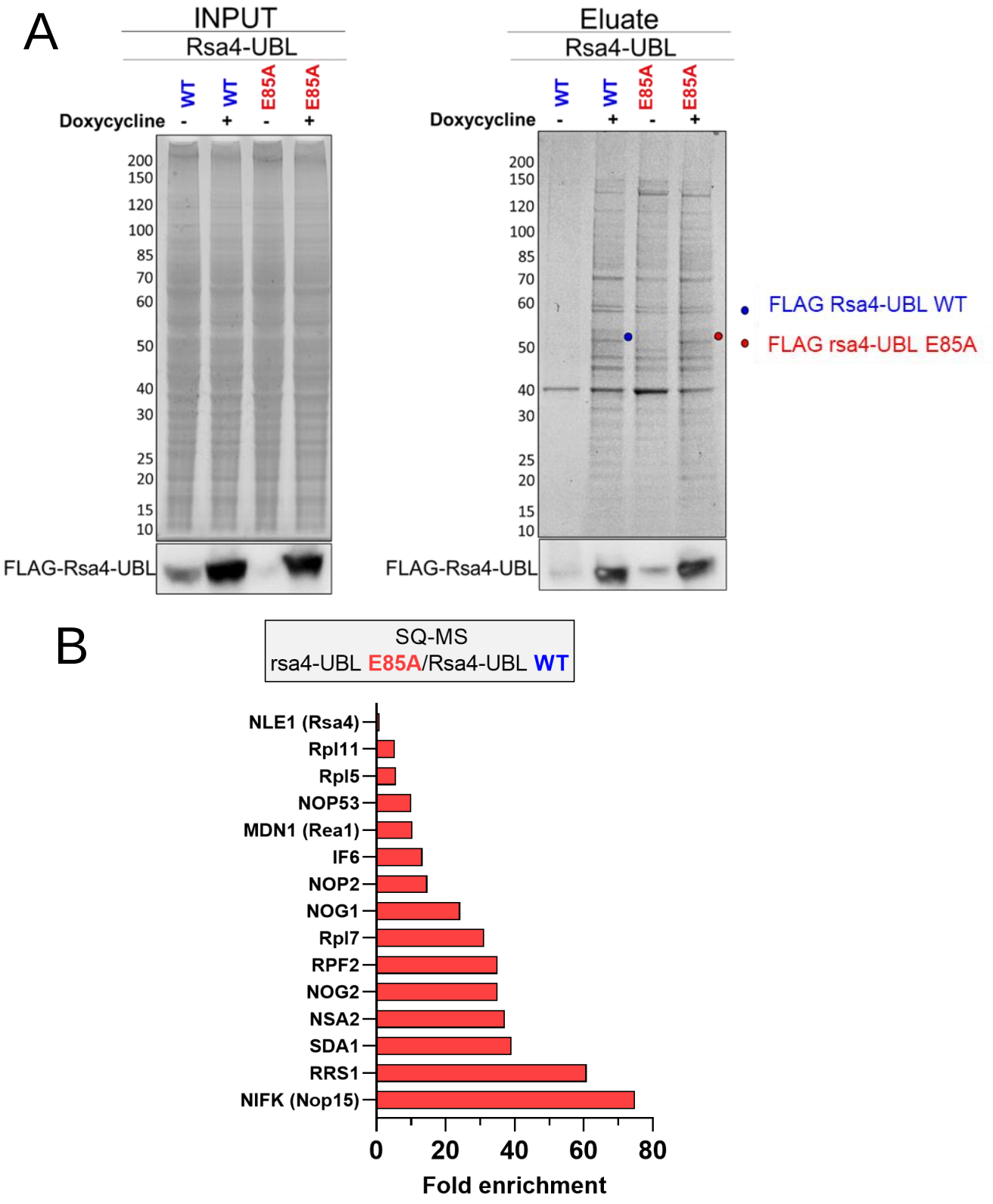

Figure 33. FLAG-purification of human nucleoplasmic pre-60S assembly intermediates from Rsa4-UBL WT and rsa4-UBL E85A mutant cells.
A) Input and FLAG eluate of FLAG-purification of Rsa4-UBL WT and rsa4-UBL E85A particles from HEK293 cells uninduced and induced with doxycycline for 24 hours. The input and Flag eluates were divided and separated by 4-12% gradient SDS-PAGE and stained with Coomassie blue (upper part) or analysed by Western blot analysis to monitor the overexpression of the bait protein. **B)** Semi-quantitative mass-spectrometry performed on the Flag eluates of Rsa4-UBL WT and E85A depicted in A. LFQ values from rsa4-UBL E85A (normalized to the bait Rsa4) were divided by the values from Rsa4-UBL WT to calculate the fold change.

To gain insights into the structure of the pre-60S particles that could be isolated from cells overexpressing rsa4-UBL E85A mutant, in collaboration with the Beckmann lab, we analysed the cryo-EM structure of these large subunit assembly solving the structure of the rsa4-UBL E85A pre-60S intermediate, shown in **Fig. 34A** and compared to yeast pre-60S particles **(Fig. 34B)**. By superimposing the human and yeast structures, I could observe that the structure of the nucleoplasmic pre-60S particles is overall conserved from human to yeast **(Fig. 34C)**. A high degree of similarity between the human and the yeast pre-60S particles can be observed in the densities of the unrotated 5S RNP, stabilized by the heterodimer Rpf2/Rrs1. Conversely, while in the major classes of rsa4-UBL E85A particles, the foot structure is not visible, there is a minor class of particles carrying a not well-resolved foot structure (*data not shown*). The reason behind the lack of foot in the major class of rsa4-UBL E85A pre-60S particles, might signify that the processing of the foot in human can still occur even when the Rea1-Rsa4 interaction and the 5S RNP maturation are blocked. An interesting feature that distinguishes the human pre-60S particles from the yeast ones is the lack of an additional density, corresponding to the protein Ebp1 (Arx1 in yeast). Ebp1 has been shown to assemble with the nascent human pre-60S at later stages of the biogenesis when the particles have already reached the cytoplasm. This peculiarity might signify that, as opposed to what happens during the yeast assembly of the large subunit with Arx1, Ebp1 it is not acting as an export factor, rather than as a ribosomal protein, binding to the 80S mature ribosome.

Taken together, all the previous data and the isolation of nucleoplasmic pre-60S particles, strongly prove that the impairment of the Rea1-MIDAS–Rsa4-UBL interaction represents a powerful tool to block ribosome biogenesis specifically. Nevertheless, to expand the utilization of this tool to a different type of cells and contexts, it might be necessary to find small chemical compounds able to mimic the effects obtained upon overexpression of rsa4-UBL E85A. Such compounds would significantly simplify the utilization of the Rea1-MIDAS – Rsa4-UBL loss of interaction both as a therapeutical and analytical tool in human cell.

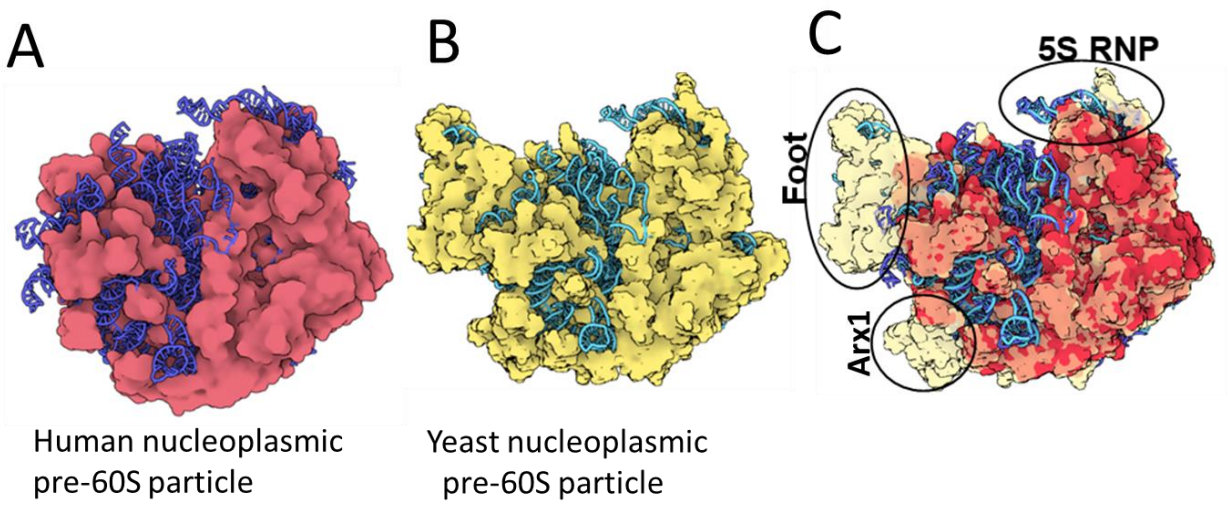

Figure 34. Human pre-60S particles isolated via rsa4-UBL E85A mutant and compared to yeast nucleoplasmic intermediates.
A) The Cryo-EM map of the major conformation identified upon isolation of pre-60S particles in rsa4-UBL E85A cells is displayed as surface representation. The ribosomal proteins and ribosomal factors are colored in red and the ribosomal RNA in blue. **B**) Cryo-EM map of the yeast pre-60S particles purified from epitope-tagged Nog2, displayed as surface representation. The ribosomal proteins and ribosomal factors are colored in yellow and the ribosomal RNA in light blue. PDB code: 3JCT. **C**) Human and yeast pre-60S particles are merged to display common features. Yellow surfaces represents structural features not conserved from yeast to human, such as: the foot structure and the Arx1 protein.

3.10 Search and screening of small compounds impairing the human Rea1-MIDAS–Rsa4-UBL interaction

Supported by the structural information of the human Rea1-MIDAS–Rsa4-UBL complex, we decided to start a collaboration with the Wolber Lab in Berlin to find small chemical compounds impairing this interaction. This approach aimed to find compounds capable of mimicking the interaction pattern shown by the *Hs*Rsa4-UBL domain with the MIDAS domain, and in particular with the Mg^{2+} ion, which was achieved via 3D pharmacophore-based virtual screening and subsequent computational filtering of hit compounds, carried out by Theresa Noonan (Wolber lab, Free University, Berlin). A pharmacophore is a group of criteria in terms of steric and electronic features that a potential drug has to fulfil to establish an interaction with the biological target and elicit its biological response. A comprehensive review of 3D pharmacophores and their use in virtual screening can be found here (*Schaller et al., 2020*). The pharmacophore features were generated by looking at the crystal structure

of the MIDAS-UBL complex and, in particular, at the interaction pattern between Rsa4-UBL and the MIDAS domain. The 3D pharmacophore shown in **Fig. 37A** was used as a template to filter a virtual database of several millions of commercially available compounds. The initial screening resulted in 25243 so-called 'hit' compounds capable of fulfilling the 3D pharmacophore features. Of these, 664 had a molecular weight of at least 450 g/mol and were selected for further filtering steps. The following filtering step consisted of molecular docking, in which compound conformations were filtered by how many of the 3D pharmacophore features they fulfilled and how well. After this step, several hits were left, and, among them, 208 were chosen based on the ability to create hydrophobic contacts with Rea1-MIDAS since hydrophobic contacts are critical players in stabilizing energetically favored ligands. The final 208 hit compounds were filtered by visual inspection according to the following criteria: at least one of the hydrophobic contacts had to be fulfilled, the compound was in a position enabling the binding to the Mg^{2+} ion; no phenyl rings were pointing into the solvent (due to the resulting entropic penalty), and the compound was not interacting with the β-hairpin loop, which is the element III of the Rea1-MIDAS that is formed after binding to Rsa4-UBL domain. This filtering resulted in the compounds selected for experimental testing **(Fig. 35)**.

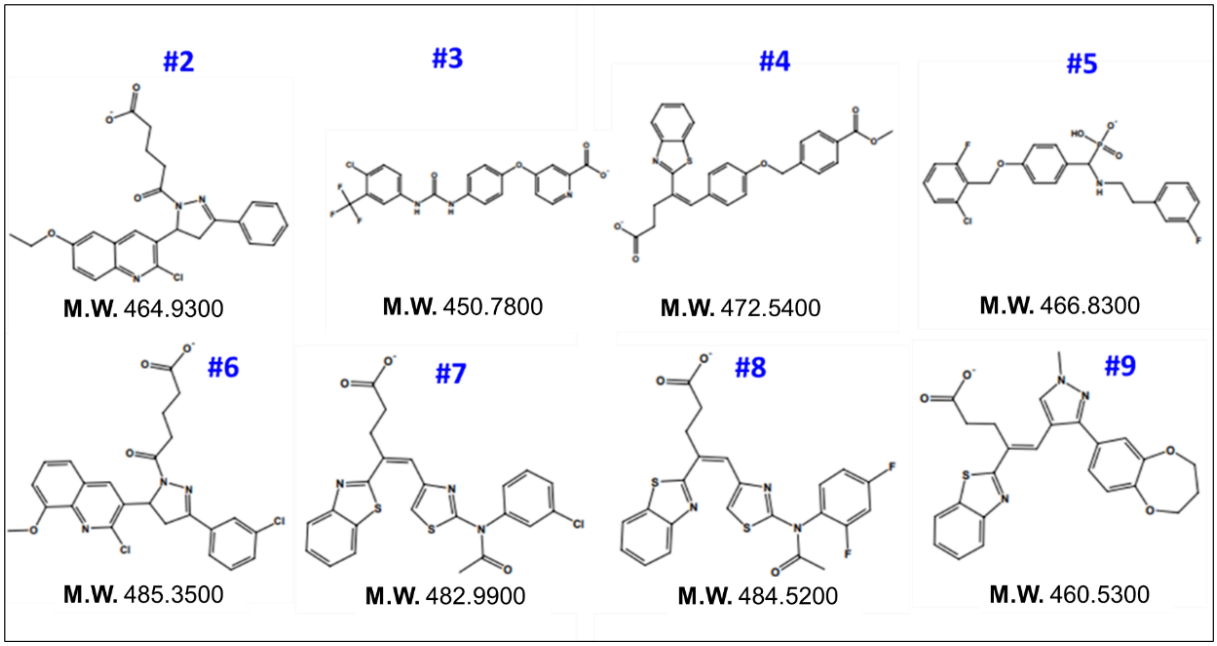

Figure 35. Molecular docking enables the *in-silico* identification of novel chemical compounds binding Rea1-MIDAS. Structure and molecular weight (M.W.) of compounds putatively able to impair the Rea1-MIDAS - Rsa4-UBL interaction, labelled using numbers from #2 to #9.

The selected compounds, showing the highest affinity to Rea1-MIDAS *in-silico,* were tested by binding assay to see whether they would impair the *Hs*Rea1-MIDAS–*Hs*Rsa4-UBL interaction *in vitro.* Hence, I performed the well-established GST pull-down assay, in which I pre-incubated *Hs*Rea1-MIDAS-$(His)_6$ with the small chemical compounds to allow the binding of the compounds to the MIDAS domain, and then I added the GST-*Hs*Rsa4-UBL binding partner to reconstitute the complex. In total, I repeated this assay 4 times. Next, I separated the eluates by SDS-PAGE followed by Coomassie-staining **(Fig. 36A)** to quantify and compare the amount of *Hs*Rea1-MIDAS-$(His)_6$ eluting with GST-*Hs*Rsa4-UBL between the treated samples and control DMSO **(Fig. 36B)**. Although none of the compounds did disrupt the Rea1-MIDAS–Rsa4-UBL complex formation entirely, I could observe a significant reduction of *Hs*Rea1-MIDAS-$(His)_6$ bound to GST-*Hs*Rsa4-UBL, (in the range of 60%) after incubation with compound #7 **(Fig. 37B)**, suggesting that compound #7 may be able to bind the MIDAS domain of Rea1.

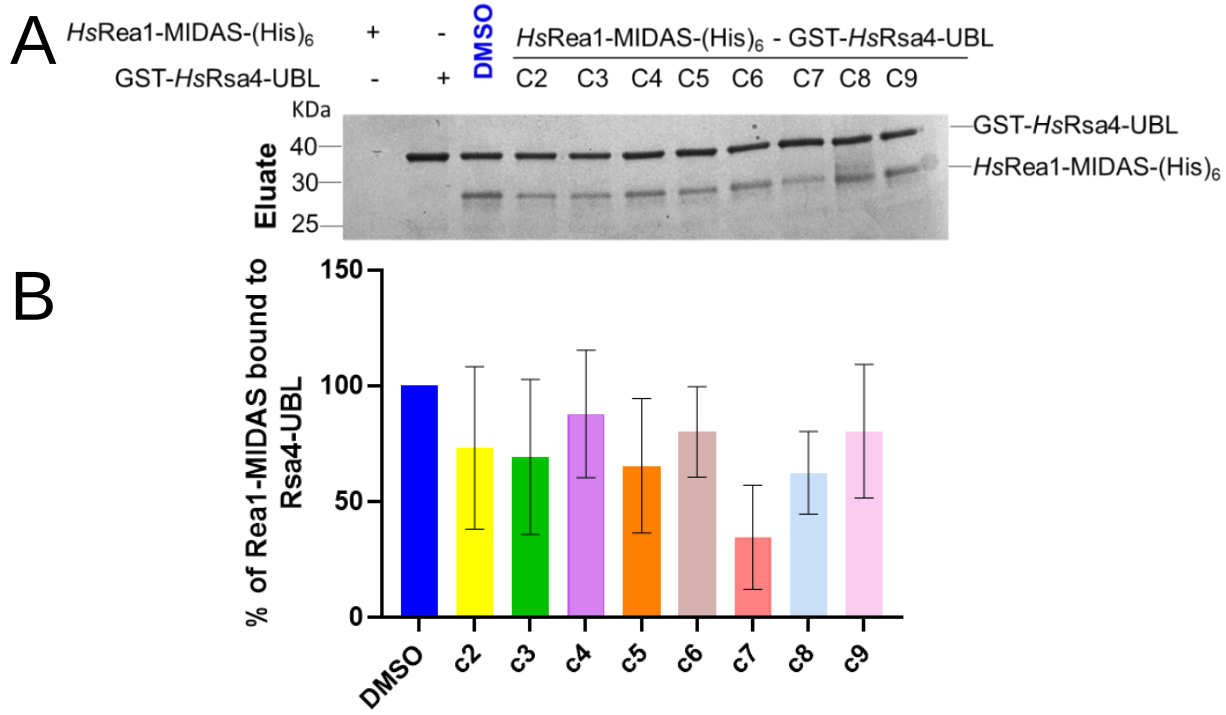

Figure 36. Identification of compound #7 inhibiting the Rea1-MIDAS–Rsa4-UBL complex formation *in vitro*. **A**) Coomassie stained SDS-PAGE of a GST pull-down assay in which 1 µM *of Hs*Rea1-MIDAS-$(His)_6$ was first pre-incubated (30 minutes at room temperature) with either 200µM small chemical compounds in 1% DMSO or control DMSO to allow the binding of the compounds to the MIDAS domain. Next, 1 µM of GST-*Hs*Rsa4-UBL was added and incubated (30 minutes) to allow the reconstitution of the *Hs*Rea1MIDAS-$(His)_6$–GST-*Hs*Rsa4-UBL complex. The SDS-PAGE of the eluate fractions shows that compound #7 inhibits the *Hs*Rea1MIDAS-$(His)_6$–GST-Rsa4-UBL interaction, compared to control DMSO. **B**) Quantification of the binding of *Hs*Rea1MIDAS-$(His)_6$ to GST-HsRsa4-UBL was performed with the software ImageJ (https://imagej.net/). The intensity of the *Hs*Rea1-MIDAS-$(His)_6$ bands and GST-*Hs*Rsa4-UBL were measured and *Hs*Rea1-MIDAS-$(His)_6$ values were normalized to GST-*Hs*Rsa4-UBLvalues and to DMSO.

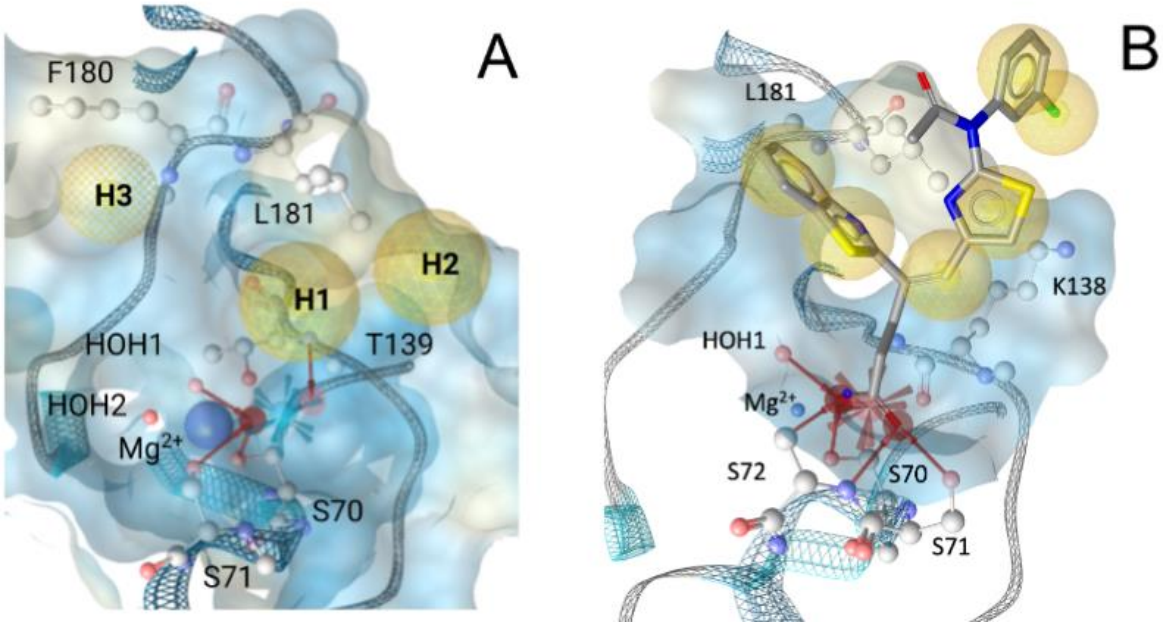

Figure 37. Compound 7 binds the MIDAS domain according to the pharmacophore-based model used as screening template. A) The original 3D pharmacophore used for the virtual screening. The pharmacophore was designed on the model of the Rsa4-UBL fragment interacting with the MIDAS domain. **B)** The structure of compound 7 bound to the MIDAS domain. Yellow spheres symbolize hydrophobic contacts. Red arrows symbolize hydrogen bond acceptors. Red bursts symbolize negative ionizable feature. Blue burst symbolize the Mg^{2+}-complexing. Yellow surfaces symbolize hydrophobic surfaces. Blue surfaces symbolize hydrophilic surfaces.

To determine whether the selected compounds, in particular number #7 affect ribosome assembly in human cells, I first performed a viability assay in HeLa cells, incubating cells with chemical compounds or DMSO, as control. Within 48 hours of treatment, cells incubated with compound #7, but not the others, displayed a robust dose-dependent reduction of viability **(Fig. 38A)**. To test whether small inhibitor #7 could also impair HeLa cells growth, I also performed an analysis of cell confluence and incubated HeLa cells with compound #7 or DMSO for 5 days. Next, I stained the cells by crystal violet, thus allowing their visualization by staining the nuclei a purple colour. In agreement with the viability assay above described compound #7 strongly reduced, in a dose-dependent manner, the growth of HeLa cells when compared to DMSO **(Fig. 38B)**.

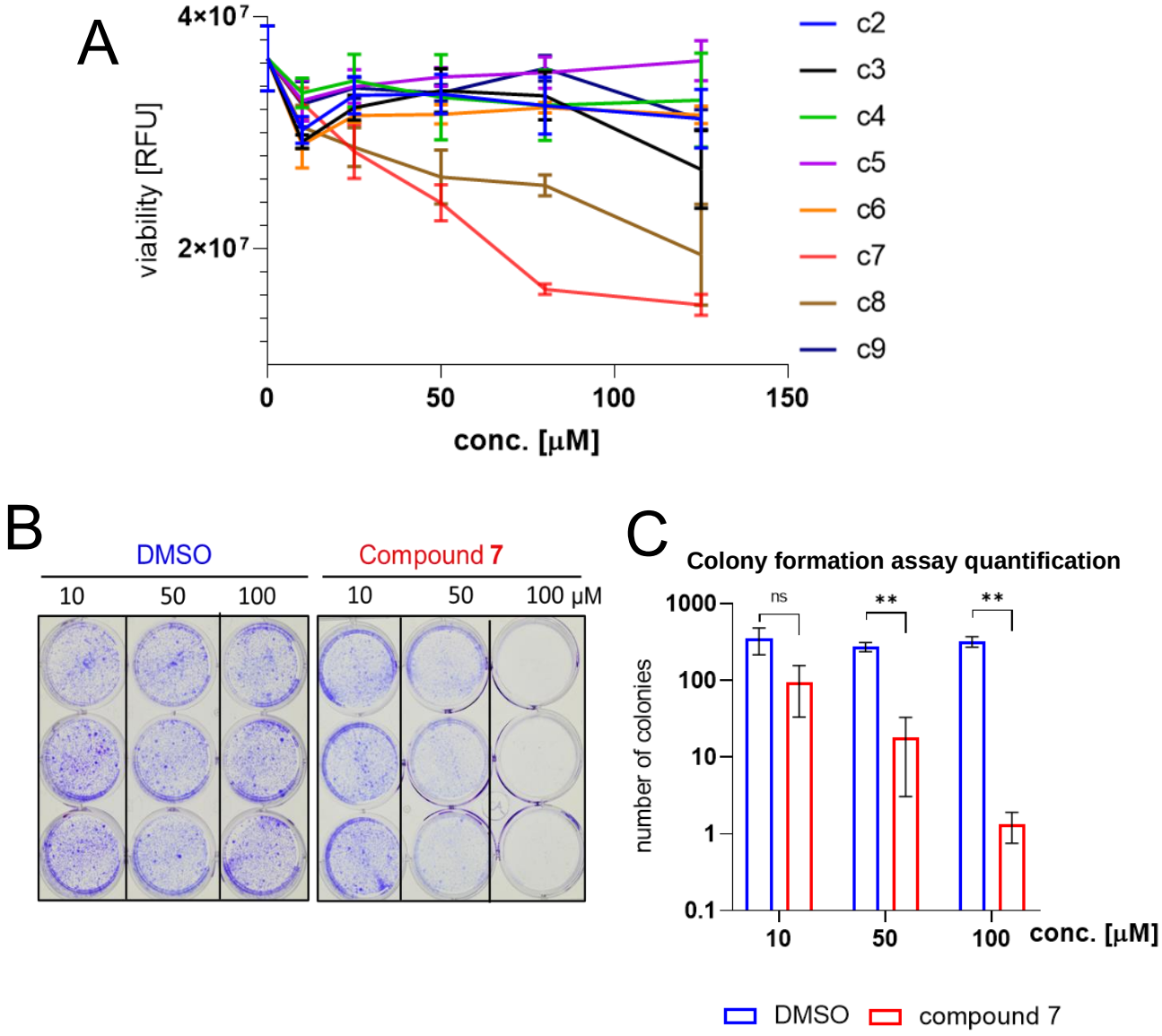

Figure 38. Compound 7 reduces HeLa cells viability and growth.
A) The inhibition of HeLa cells proliferation treated with DMSO (control) or compounds from #2 to #9 was analysed by cell titer blue assay. Cells were treated for 48 hours with increasing micromolar concentrations of drugs from 10 to 125 µM. As control cells were treated only with DMSO. The measure of the viability was performed in triplicates and error bars indicate the standard deviation of the three replicates. **B**) Images of a colony formation assay in which HeLa cells were treated with DMSO (control) or with compound #7 at 10, 50 and 100 µM final concentration. After 5 days cells were stained with crystal violet to allow their visualization and images were taken. **C**) Quantification of HeLa cells colonies formed during the treatment with DMSO and compound #7. Images of the different experimental points were analyzed with the software ImageJ to count cell colonies (number of colonies). The colony formation assay was performed in triplicate and error bars indicate the standard deviation of the three replicates.

To determine whether the phenotype observed in HeLa cells upon treatment with compound #7 was due to inhibition of the pre-60S assembly pathway, I transiently transfected, overexpressed, and evaluated the localization of the Rpl29-GFP (*Wild et al., 2010*), used as reporter, in HeLa cells treated with compound #7 or control DMSO for 5 hours at 100 µM, as previously described for rsa4-UBL E85A mutant. Rpl29-GFP is normally associated with the mature 60S subunit in the cytoplasm, with less accumulation in nucleoli. However, upon defects occurring during the ribosome assembly, Rpl29-GFP accumulates in the nuclear compartment. Accordingly, Rpl29-GFP retained its normal distribution in the cytoplasm, with a less prominent localization in the nucleoli, indicating a correct ribosomal export. Conversely, in cells incubated with compound #7, the signal of Rpl29-GFP accumulated in the nucleus, while the cytoplasmic signal was mostly gone. This data suggests that compound #7 may block progression of the nascent pre-60S subunit (**Fig. 38A**).

Next, to demonstrate that compound #7 mainly affects the 60S, but not 40S assembly pathway, I also analysed another ribosomal reporter protein, Rps2-YFP (Wild et al., 2010), normally associated with the 40S subunit in the cytoplasm, but accumulating in the nucleus upon inhibition of the 40S assembly pathway (*Zemp et al., 2009*). Upon transfection of Rps2-YFP in cells treated with either compound #7 or control DMSO, the reporter protein Rps2-YFP always retained its normal cytoplasmatic localization **(Fig. 38B).** Taken together, this analysis suggests that compound #7 affects specifically nuclear export of the pre-60S particles, but not pre-40S particles.

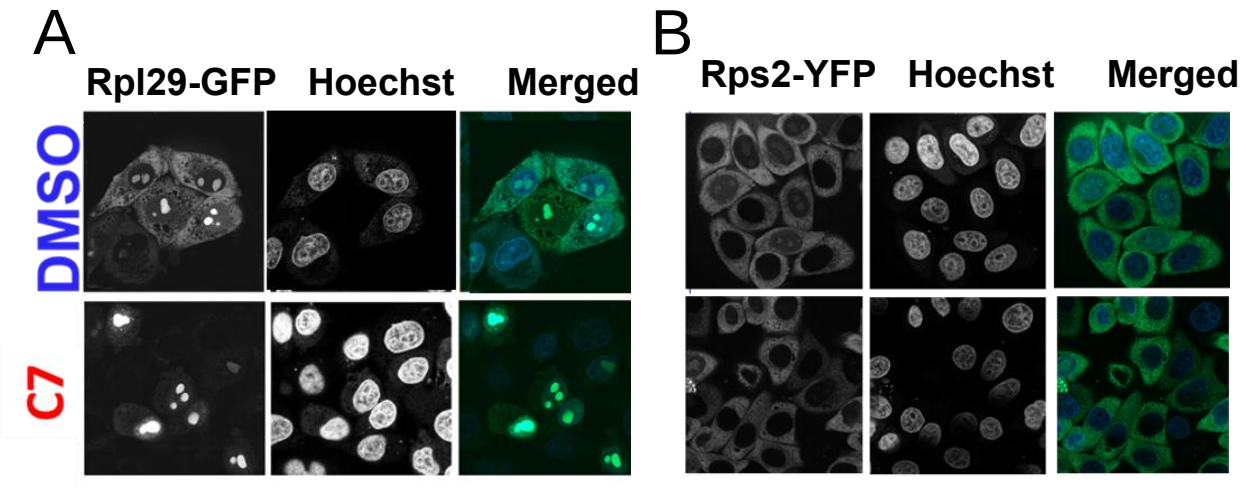

Figure 38. Analysis of nuclear export of 60S and 40S subunits in HeLa cells treated with compound 7 and DMSO

A) The confocal microscopy monitoring the subcellular localization of Rpl29-GFP in HeLa cells treated with compound #7 or DMSO (control) shows accumulation of Rpl29-GFP within the nuclear compartment and no cytoplasmic signal in HeLa cells upon treatment with compound #7 compared to the DMSO control. **B**) Confocal microscopy monitoring the subcellular localization of Rps2-YFP in HeLa cells treated with DMSO (control) compound #7 shows no alteration of the subcellular localization of Rps2-YFP in HeLa cells upon treatment with compound #7 compared to the DMSO control. In both experiments nuclei are counterstained with Hoechst and treated and control cells were imaged according to the same setting: 800V, 1.5X zoom, 60x oil objective.

4 Discussion

4.1 Rea1-MIDAS forms a high-affinity complex with Rsa4-UBL

The structural characterization of pre-ribosomal particles from yeast has provided deep insights into the mechanisms of ribosome biogenesis, but such an information for higher eukaryotes is still scarce. In my PhD-study, I could provide new data regarding the role of the Rea1-Rsa4 human complex for the ribosome assembly and revealed how the human Rea1 AAA^+ ATPase interacts with Rsa4 by carrying an extensive biochemical and structural study of their interacting domains. The reconstitution *in vitro* of the human Rea1-MIDAS-*Hs*Rsa4-UBL complex, which displays a 1:1 binding stoichiometry, was the starting point of my PhD work and allowed me to have a solid foundation to dig deeper into the further biochemical and functional evaluation of this interaction. Recently, using microscale thermophoresis, it was reported that the affinity of Rea1-MIDAS to the UBL domains of Rsa4 and Ytm1 in *Schizosaccharomyces pombe* is greater than 7µM, with a K_D in the micromolar range (*Mickolajczyk et al., 2022*), thus indicating a weak affinity in solution. This finding appears controversial to my data showing that the *Hs*Rea1-MIDAS–*Hs*Rsa4-UBL complex exhibit a high binding affinity in solution, with a K_D in low nM range of ca. 5 nM. Moreover, during my studies, I also observed that it is possible to displace the *Hs*Rea1-MIDAS–*Hs*Rsa4-UBL with the help of a high-affinity competitor, a result which was essential for my work, as it suggested that this interaction could have also been a potential target for newly discovered small molecule compounds, able to displace the complex or prevent the *de novo* interaction of both factors.

4.2 Impairing the human Rea1 and Rsa4 interaction as a potential tool for cancer therapy

The Rea1-MIDAS and Rsa4-UBL proteins do not play a key role only during the maturation of the pre-60S ribosome but are also part of an intricate network of interactors and effectors linked to cancer development. The protein Rsa4, Notchless homolog 1 in humans (NLE1), plays an essential role in cell proliferation, transcription and signal transduction (*Karimzadeh et al., 2017*). Rsa4 is also highly expressed in

many cancers, such as melanoma and breast cancer, in which it promotes a malignant phenotype through the activation of the PI3K/AKT signalling cascade *(Ren et al., 2021*). There is evidence that mutations affecting the function of Rsa4 cause a strong lethal phenotype and caspase-3-dependent apoptosis (*Lossie et al., 2012*); therefore, the inhibition of Rsa4 related functions could also impair cancer development.

Some studies have reported that the protein Rea1 (Mdn1 or Midasin in humans) is overexpressed in specific subtypes of breast cancer, especially those resistant to hormonal therapy. This information suggests an emerging role for the protein Rea1 as a cancer biomarker, and as a factor favouring the cancerogenic and malignant phenotype and drug resistance in breast cancer (*Gallegos et al., 2021*; *Walker et al., 2021*). In yeast, the protein Rea1 interacts with the Rix1 complex (Rix1-Ipi3-Ipi1) (*Baßler et al, 2001; Ulbrich et al., 2009; Baßler et al, 2010; Barrio-Garcia et al., 2016)*.

The mammalian counterpart of the Rix1 complex is composed of the proteins PELP1 (yeast Rix1), TEX10 (yeast Ipi3), and WDR18 (yeast Ipi1), forming the PELP1 complex, which is associated with pre-60S particles and is pivotal for 60S biogenesis (*Castle et al., 2012*). Notably, the protein PELP1 can be SUMOylated in a proline-rich region by the protein SUMO2 *(Finkbeiner et al., 2011)*. It is thought that this post-translational modification may be requested to enable the recruitment of the protein Rea1 on the nucleoplasmic pre-60S particle (*Raman et al., 2016*). Interestingly, the overexpression and deregulation of PELP1 has also been reported in cancers, such as ovarian cancer, triple-negative metastatic breast cancer *(Dang et al., 2015; Wang et al., 2019*), lung cancer and colon-rectal cancer (*Ning et al., 2014)*. In these tumours, PELP1 plays a key role in cancer metastasis (*Cortez et al., 2012; Gonugunta et al., 2014; Gallegos et al., 2021*), hence, there is a critical need for the development of therapeutic agents that interfere with PELP1 signalling pathways. As PELP1 lacks known enzymatic activity (*Sareddy and Vadlamudi, 2016*), finding small chemical compounds targeting downstream interactors of the PELP1 signalling pathway, such as the Rea1–Rsa4 complex formation, could be possible tool to stall ribosome biogenesis and impair the growth of PELP1-derived tumours.

In agreement with that, during my PhD studies, I demonstrated that the loss of the Rea1-MIDAS–Rsa4-UBL binding causes a dominant-negative phenotype in cultured human cells in terms of reduced cell growth and cell viability by decreasing the expression levels of oncogenic proteins such as the transcription factor c-Myc and

Cyclin D1 and by executing the apoptotic response via the cleavage of the caspase-3.

4.3 Differences and similarities between human and yeast nucleoplasmic pre-60S particles

During my PhD studies, in collaboration with the Beckmann lab (Matthias Thoms), we solved the structure of a nucleoplasmic intermediate of the human pre-60S assembly pathway from HEK293 rsa4-UBL E85A mutant cells. Comparison carried out between nucleoplasmic human and yeast pre-ribosomes showed a high degree of similarity between the particles, in agreement with the known conservation of the ribosome assembly pathway between human and yeast. As I mentioned in my introduction, the rotation of the 5S RNP and maturation of the central protuberance are critical structural remodelling events during the pre-60S assembly and are coupled with the action of the ATPase Rea1 inducing structural changes on pre-60S particles (*Barrio-Garcia et al., 2016*). As our particles are purified from rsa4-UBL E85A mutant cells, the Rea1-mediated removal of Rsa4 does not occur, and the 5S RNP remains in its unrotated conformation; hence the maturation of the central protuberance is also impaired. Moreover, comparing the human and yeast structures, I witnessed that the prominent foot structure is not visible in a major class of rsa4-UBL E85A particles, signifying that the processing of the foot may proceed uncoupled of the 5S RNP rotation. This data agrees with previous findings showing that the foot structure is missing when the 5S RNP rotation is inhibited in pre-60S particles upon depletion of the assembly factor Cgr1 (*Thoms et al., 2018*). Curiously, nucleoplasmic yeast particles, compared to human carry an extra density, corresponding to the nuclear export factor Arx1 (*Bradatsch et al., 2007; Hung, et al., 2008*). Indeed, in yeast, Arx1 is already bound to the pre-ribosomes before the nuclear export, it functions as export factor and then gets removed from the maturing pre-60S (*Bradatsch et al., 2007)*. However, the human protein Ebp1, yeast Arx1, is missing from the human nucleoplasmic pre-60S intermediate solved in this work. It has been observed that in human pre-ribosomes, Ebp1 binds directly after the nuclear export and therefore may not act as export factor but may have a role as regulator of co-translational modifications since it remains bound to the mature 80S ribosome and does not get removed during the assembly pathway (*Wild et al., 2020)*. What we observed in our nucleoplasmic pre-60S particles

is also confirmed by cryo-EM reconstructions of human NMD3-containing particles, in which were obtained pre-60S subunits right before and right after the nuclear export. In this study, the density corresponding to Ebp1 is missing in the stage right before nuclear export and can be observed only in cytoplasmic intermediates found right after the export *(Liang et al., 2020*).

4. Compound 7 may enable the use of the Rea1-MIDAS–Rsa4-UBL interaction as a therapeutical and analytical tool

To take advantage of the dominant-negative phenotype obtained upon loss of the Rea1-MIDAS–Rsa4-UBL interaction and to exploit it to impair cancer cell growth, we aimed at finding chemical inhibitor compounds which could impair the Rea1-MIDAS–Rsa4-UBL interaction and stall the ribosome biogenesis. At the beginning of this project, an atomic structure of the human Rea1-MIDAS–Rsa4-UBL was still unavailable; hence we aimed to find new chemical compounds impairing this complex by using the high throughput Alphascreen technology, working with the Chemical Biology Core Facility at EMBL -Heidelberg. The alpha screen is a beads-based, non-radioactive assay used to evaluate protein-protein interactions. During the assay, proteins are bound to either donor or acceptor beads, and when a biological interaction brings the proteins and the beads together, a cascade of chemical reactions produces an amplified signal. Initially, we carried out a pilot screen and a full high-throughput Alphascreen in which several thousand compounds were tested. From this assay, almost three hundred promising compounds were identified and one for each chemical cluster was reordered and tested again with a negative control. Unfortunately, none of the compounds identified resulted in a specific inhibition of the Rea1-MIDAS–Rsa4-UBL interaction since also the interaction between the large protein interface of the unrelated negative control (Titin/Carp) was impaired. For this reason, we stopped this attempt.

The availability of an atomic structure of the complex, with an excellent resolution, opened the possibility to virtually screen for chemical compounds in collaboration with Theresa Noonan, Wolber lab (Free University of Berlin). The Wolber lab screened virtual libraries to find compounds carrying distinct characteristics such as a negatively charged moiety competing with the glutamate of the UBL domain (E85) for the binding

to the Mg^{2+} of the MIDAS domain. When I tested the suggested compounds using biochemical and cell-culture based assays, I discovered that compound #7 could prevent the Rea1-MIDAS–Rsa4-UBL *in vitro* interaction, affect the viability of HeLa cancer cells and cause export defects of ribosomal proteins. When I inspected the chemical structure of compound #7 in detail, I learned that compound #7 belongs to a class of chemicals classified as benzothiazoles. Benzothiazoles and their derivates have an enormous significance in drug discovery and drug development processes since they are found in a broad spectrum of anti-cancer and anti-proliferative drugs, also as antagonists of integrins (*Carpenter et al., 2009; Irfan et al., 2020*). Interestingly, in addition to the benzothiazole group, compound 7 carries another chemical feature, a halogen element, in the form of chlorophenyl. Halogen elements in drugs have been extensively used for drug optimization. Because of their highly electronegative sites, halogens can function as electron nucleophiles, improving the binding affinity of some compounds to their targets (*Cavallo et al.; 2016*). It is known that heavy halogens like Br or Cl can form halogen bonds, while F cannot. This diversity could explain why compound #7, which carries an additional chlorophenyl, has a more robust potency than compound #8, also belonging to the benzothiazole derivates, but exerting a less robust effect in terms of inhibition of the MIDAS-UBL interaction *in vitro*.

5 Conclusion and outlook

The effect on cell growth and assembly of the large ribosomal subunit driven by the human Rsa4-UBL mutant is potent, suggesting that impairing the human Rea1-MIDAS–Rsa4-UBL interaction could be exploited as a therapeutical tool.

Using the solid data of the Rea1-MIDAS–Rsa4-UBL crystal structure, we found an active compound that could, supposedly, prevent the Rea1-MIDAS–Rsa4-UBL interaction, thus stalling the nucleoplasmic maturation of the large ribosomal subunit and provoking cell death. Many inhibitors of ribosome biogenesis targeting RNA polymerase I exist already; therefore, it might be interesting to explore more the human ribosome biogenesis in order to find new and better targets. Compound #7 may be one of them. However, the compound presented in this work is still in its primordial stage, and further experiments are needed to characterize it deeply. Besides the assessment of the *in vitro* ability of the compound to impair the Rea1-MIDAS–Rsa4-UBL interaction and the analysis of the antimitotic phenotype in human cells, a further evaluation of its specificity for the 60S biogenesis pathway has to be carried out. At last, the availability of a crystal structure may allow, in future, the further optimization of the compound by to increase its potency and the affinity and specificity to the MIDAS domain. Such a process may eventually enable the use of this molecule for more clinical and translational purposes

6 Material and methods

6.1 Cloning

Plasmids were constructed using standard recombinant DNA techniques. All plasmids used and constructed or purchased for this study are listed in Supplementary Tables (Chapter 7).

6.2 Polymerase chain reaction

Amplification of DNA fragments was performed by polymerase chain reaction (PCR) using Phusion™ High-Fidelity DNA Polymerase (2 U/µL) DNA Polymerase in thermocycler (Eppendorf). Primers were synthesized by Sigma Merck.
Primer annealing temperature and elongation time of the PCRs were adjusted based on the melting temperature of the primer and the desired product length, respectively.

6.3 Mutagenesis

pET GST-*Hs*Rsa4 E85K plasmid was obtained with one-step PCR-based mutagenesis technique. 1µL of 200 ng/µL of plasmid was added to a PCR reaction mix (18.5 µL H2O, 10 µL HF 10X Buffer, 1 µL Taq DNA ligase, 1 µl PCR Phusion Polymerase, 8 µL dNTPs, 10 µL 3,3 mg/ml fresh NADH, 2,5 µL 10 mM phosphorylated primer carrying the E->K mutation. Posphosphorylation mix was composed by 2 µL of 100 µM primer, 5 µL 10 mM ATP, 5 µL 10x T4 PN Kinase buffer (NEB), 37 µL water. The mix was incubated 30 minutes at 37°C, at 65°C for 15 minutes and directly used for the PCR reaction (1 minute at 95°C followed by 30 cycles of 95°C 1 minute, 55 °C 1 minute and 65°C 4 minutes).
PCR mixture was digested overnight with DpnI enzyme and transformed in *E.coli* DH5a after purification (GenElute™ PCR Clean-Up Kit, Sigma, cat. Number NA1020) in DH5a competent cells.

6.4 Transformation of *E.Coli* DH5a cells

100 ng DNA were added to 50 uL aliquot of *E.Coli* DH5a cells and left and incubated on ice. After 20 minutes, thermic shock was applied and cells were heat for 1 minute

at 42°C. 1 mL of LB media, without antibiotic was added to the cells to allow them to grow at 37°C for 20 minutes. Grown cells, were plated on LB agar petri dish supplemented with the appropriate antibiotic

6.5 Preparation of plasmid DNA

A single colony of E. coli DH5α was inoculated into 5 mL LB-medium supplemented with the appropriate antibiotics, grown at 37 °C overnight and harvested by centrifugation. Isolation of plasmid DNA was performed using the Sigma Aldrich Miniprep Kit following the manufacturer's instructions. The nucleotide concentration was determined spectroscopically by measuring the absorbance at 260 nm (A260 nm =1 ≙ 50 µg/µl) using NanoDrop ND-1000 spectrophotometer (NanoDrop Technologies). The nucleotide sequence was confirmed by Eurofins Genomics.

6.6 Transformation of *E.Coli* BL21 cells

For protein expression, electroporation was applied using 50 µL aliquot of competent cells thawed on ice and mixed with 1 µl plasmid DNA and 50 µL of water. Cells were directly transferred to a 2 mm electroporation cuvette (peQLAB) and subjected to a short electric pulse (~ 5 ms) using Bio-Rad gene Pulser X using a Voltage of 1.8 KV. Afterwards, the cells were mixed immediately with 0.5 ml LB-medium, transferred to a Eppendorf tube and incubated on a Thermomixer compact (Eppendorf) at 750 rpm and 37 °C. After 1 h, the mixture was plated on pre-warmed LB-agar plates supplemented with the appropriate selection antibiotics and incubated at 37 °C overnight.

6.7 Protein expression in E.Coli BL21 cells

Proteins were expressed in BL21 competent *E. coli* (as described above) in LB medium supplemented with chloramphenicol (34 µg/ml) and either kanamycin (30 µg/ml) or ampicillin (100 µg/ml). Cells were grown to an OD_{600} value of 0.6–0.9 at 37 °C and induced with IPTG 0.5 mM at 18°C overnight (*R*ea1-MIDAS) or 23°C for 3 hours (Rsa4-UBL). Cells were harvested by centrifugation, and the cell pellets frozen in liquid nitrogen and kept at -80°C.

6.8 Protein purification from E. coli of Rea1-MIDAS(His)$_6$ or GST-Rsa4-UBL

Cell pellet was thawed, and cells were resuspended in lysis buffer and lysed with Microfluidizer homogenizer (Microfluidics) at 0.8 MPa in Lysis Buffer with protease inhibitors and centrifuged for 20 min at 20,000 × *g* at 4 °C. The supernatant was incubated for 2 hours at 4°C with Ni-NTA beads for Rea1-MIDAS-(His)$_6$ or GSH-beads for GST-Rsa4-UBL, previously washed 3 times with 15 mL of lysis buffer. After incubation, Ni-NTA or GSH-beads were centrifuged for 1 minute at 1000 rpm at 4°C and the supernatant was collected as flow through. 2 mL beads were added to elution column and washed tree times with 15 ml of wash buffer and eluted with elution buffer. The Ni–NTA was concentrated, centrifuges and loaded into Superdex® 200 26/60 column equilibrated with SEC buffer (Gel filtration ÄKTA system). Peak fractions containing (his)$_6$Rea1-MIDAS were pooled, concentrated to 10–15 mg/ml, frozen in liquid nitrogen and stored at −80 °C. The GST-Rsa4-UBL eluate was applied to a Superdex® column 75 26/60 column, previously equilibrated with SEC buffer. Peaks fractions were pooled and concentrated up to 9-11mg/mL.

Buffers for (His)$_6$-tagged Rea1 purification

Lysis Buffer: 20 mM HEPES, pH 8, containing 30 mM Imidazole, 500 mM NaCl, 5mM MgCl2, protease inhibitors

Elution Buffer: 20 mM HEPES, pH 7.5, containing 400 mM Imidazole, 500 mM NaCl, 5mM $MgCl_2$.

Wash Buffer: 20 mM HEPES, pH 8, containing 30 mM Imidazole, 500 mM NaCl, 5mM $MgCl_2$.

SEC Buffer: 20 mM HEPES, pH 7.5, containing 150 mM NaCl, 5mM $MgCl_2$, 1mM DTT.

Buffers for GST-tagged Rsa4 purification

Lysis Buffer: 20 mM HEPES, pH 8, containing 150 mM NaCl, 5mM $MgCl_2$, protease inhibitors.

Elution Buffer: 20 mM HEPES, pH 7.5, containing 150 mM NaCl, 5mM $MgCl_2$,30 mM glutathione.

Wash Buffer: 20 mM HEPES, pH 8, containing 150 mM NaCl, 5mM $MgCl_2$.

SEC Buffer: 20 mM HEPES, pH 7.5, containing 150 mM NaCl, 5mM $MgCl_2$, 1mM DTT.

6.9 Protein purification from *E. coli* of (His)$_6$*Hs*Rea1-MIDAS-(His)$_6$-*Hs*Rsa4-UBL complex

For the reconstitution of the *Hs*Rea1-MIDAS(His)$_6$-(His)$_6$-*Hs*Rsa4-UBL complex used for the crystallization, a (His)$_6$N-terminal version of the *Hs*Rsa4-UBL domain was used. The protein domains were overexpressed and lysed separately, then pulled together and incubated on Ni-NTA beads for 2 hours at 4°C, thus allowing the reconstitution of the complex.
The purification was performed as previously described, and the final Ni–NTA eluate was applied to a Superdex® 200 26/60 column equilibrated with SEC buffer (20 mM HEPES, pH 7.5, containing 150 mM NaCl, 5mM mgCl2, 1mM DTT). Unicorn Peak fractions containing (His)$_6$*Hs*Rea1-MIDAS/ (His)$_6$*Hs*Rsa4-UBL complex were pooled, and the additional peak containing the excess of (His)$_6$*Hs*Rsa4-UBL was discarded. Fractions containing the complex were concentrated up to 9 mg/ml left overnight at 4C° and directly used for crystallization purposes.

6.10 Concentration of proteins using centrifugal concentrators

A centrifugal concentrator (A*micon® Ultra, Millipore)* is a tool for reducing the volume of a protein sample and thereby increasing its concentration or possibly change a buffer. For this work, concentrators were used for volumes of 4 and 15 mL, with a cut-off from 10kDa to 30KDa, to retain the proteins with the correct molecular weight. The Amicon® Ultra was equilibrated with SEC buffer before loading of the protein and centrifuged at 4000 x g, 10 min, 4 °C. After each round of centrifugation, the concentrate was pipetted up and down several times to avoid the formation of aggregates. The procedure was repeated until reaching the desired concentration and then instantly used or transferred in a new Eppendorf for storage.

6.11 Crystallization of the human Rea1-MIDAS – Rsa4-UBL complex

Crystals used to resolve the structure for this study were grown in a solution of 0.2 M Ammonium sulphate, 18.18% v/v Polyethylene glycol 300, 0.1 M Sodium Acetate, 3.5 M Ammonium Chloride using the sitting-drop vapor diffusion at 4°C. Crystals appear around the day number 9, growing for almost 30 days. Prior to data collection, crystals

were harvested in reservoir solution supplemented with 20% glycerol and flash-cooled with liquid nitrogen and sent to the EMBL Grenoble.

6.12 GST-pull down assay

For the *in vitro* binding assay of the human $(His)_6$*Hs*Rea1-MIDAS/GST-*Hs*Rsa4-UBL domains, the $(His)_6$*Hs*Rea1-MIDAS was incubated in binding buffer (20 mM HEPES, pH 7.5, 150 mM NaCl, 5mM mgCl2, 0,01% NP-40) in different conditions: with GST-*Hs*Rsa4-UBL WT alone, GST-*Hs*Rsa4-UBL E85K alone, with GST-*Hs*Rsa4-UBL WT plus increasing molar ratio of soluble untagged *Hs*Rsa4-UBL WT or small chemical compounds (100 µM). The assay was performed by incubating the proteins on a rotating wheel for 30 minutes at 4 °C or RT. Next, GST-tagged bait protein bound to the beads was pulled down by high-speed centrifugation for 1 minute, the supernatant was collected as flow-through, and beads were washed three times with gel filtration buffer (150 mM NaCl supplemented with 0,1% NP-40). For the elution step with SDS sample buffer, samples were boiled at 92°C degree for 5 minutes in Eppendorf compact at 750 rpm. Eluates were analysed using sodium dodecyl sulphate (SDS) polyacrylamide gel electrophoresis on 4–12% polyacrylamide gels (NuPAGE, Invitrogen) Coomassie staining.

6.13 SDS-polyacrylamide gel electrophoresis (SDS-PAGE)

SDS-PAGE was performed to separate a protein mixture. The protein sample was denatured by mixing with a reducing sample buffer containing sodium dodecyl sulphate (SDS) and loaded on the gel.
Mainly, gels NuPAGE a 4-12% gradient (Invitrogen) was used, and the electrophoresis was performed using vertical gel electrophoresis Invitrogen Novex mini-Cell (Invitrogen). Protein marker, Page ruler Protein ladder (Thermo Scientific) and denatured protein samples were applied into the gel pockets and a constant voltage of 160 V in the beginning and 180 V after a few minutes was applied. The electrophoresis was stopped once the blue loading dye running front had reached the bottom of the gel.

6.14 Coomassie staining

Coomassie staining 0.1 % (w/v) was used to visualize protein bands. The gels were covered with Coomassie staining and incubated at RT on a rocking platform for 1 hour. Distaining solution (30% EtOH, 10% Acetic Acid, H_2O) was then applied for 20 minutes, gels were covered with deionized H_2O and pictures were taken.

6.15 Adherent cell culture

Adherent 3xFLAG Rsa4-UBL WT and E85A HEK293 or HeLa cells were maintained in DMEM, supplemented with 10 % (v/v) FCS and 1 % (v/v) Penicillin/Streptomycin in a humidified atmosphere at 37 °C and 5 % CO2. For passaging, cells were washed once with PBS 1X, incubated for 5 min at 37 °C with trypsinization solution (1x Trypsin/EDTA solution in PBS) and detached by pipetting fresh media on the 10 cm dish. The desired number of resuspended cells was transferred to a new 10 cm dish and supplemented with additional fresh DMEM supplemented with 10 % (v/v) FCS and 1 % (v/v) Penicillin/Streptomycin up to 10 mL/dish.

6.16 Transient transfection

HeLa cells were transfected with pcDNA3.1(+)-N-GFP Rpl29 and pcDNA3.1(+)-N YFP Rps2. Transfection experiments were performed according to manufacturer's instructions using Lipofectamine 2000 (Thermo Fisher). Cells were transfected at 80% confluence. Plasmidic DNA was mixed with DMEM without FCS and antibiotic, 3 µL of Lipofectamine 2000 were used for each µg of DNA. DNA solution and Lipofectamine solution were mixed 1:1 and incubated for 20 minutes at RT. The transfection mix was added to the cells in a dropwise manner.

6.17 Human cells lysate

HEK293 cells or HeLa cells were collected and centrifuged at 10000 rpm for 1 minute. Media was aspirated and cells were washed with PBS 1X and centrifuged at 10000 rpm for additional 2 minutes. After the last wash, PBS 1X was discarded and RIPA

buffer (SERVA) complemented with Protease inhibitors (SIGMAFAST) was added to the cell pellets. Pellets were incubated on ice and vortexed every 5 minutes. After 30 minutes of incubation cells were centrifuged for 20 minutes at max speed (14000 rpm) at 4°C in Eppendorf centrifuge 5417 R. Following centrifugation, the supernatant was retained and stored as total cell lysate, while the pellet was discarded.

6.18 Western blot analysis

The total cell lysate was resolved by SDS-PAGE 180V/1 hour (NuPAGE, Invitrogen) followed by a transfer to a nitrocellulose membrane using a semi-dry blot 11V/45 minute. The membrane was stained by Ponceau S (SERVA) to check whether the transfer was successfully and blocked for 45 minutes in 5% PBS-milk solution complemented with 0,05% Tween. Primary antibodies were incubated overnight at 4°C. After incubation, the membrane was washed three times with PBS 1X supplemented with 0,05% Tween. The antibodies used for this work are the following: anti-Flag antibody (1:30,000, Sigma-Aldrich A8592), anti-GAPDH (Cell Signalling Technology 1:10,000 I4C10), anti-caspase 3 cleaved (Cell Signalling Technology 1:1000 5A1E, rabbit) anti-c-Myc (Cell Signalling Technology 1:1000 D84C) anti-CID1 (Cell Signalling Technology 1:1000). Detection of the HRP conjugated antibodies was done using solution Immobilon Western HRP Substrate (Millipore) and the machine and software Image Quant LAS 4000 (GE Healthcare).

6.19 Confocal microscopy

HEK293 Flag Rsa4-UBL WT and E85A were seeded on poly-lysine coated glass bottom petri dish at high confluence and allowed to attach overnight. One day after seeding, cells were transfected with Rpl29-GFP or Rps2-YFP reporter plasmid and incubated for 24h with 1 µg/ml doxycycline. After induction cells were washed with 1X PBS, fixed with 2% PFA for 15 minutes at RT and stained with Hoechst 1:1000 (Thermo Fisher). Cells were imaged with Zeiss confocal microscope and an average of 20 pictures were taken for each condition in several replicates.

6.20 Colony formation assay

HEK293 Flag Rsa4-UBL WT, E85A or HeLa cells were seeded on 6-well plates and incubated with 1 µg/ml doxycycline or increasing concentrations of small chemical compounds (10, 50 and 100 µM) After 5 days of induction or treatment, cells were carefully washed one time with PBS 1X, fixed with cold methanol 100% for 10 minutes and stained with crystal violet (Sigma) for 2 hours. After staining, the crystal violet was discarded according to safety procedures and 6-wells plates were carefully rinsed with tap water and photographed with Nikon camera. Images of the colonies were analysed with ImageJ. (8-bit<set background<measure particles). The experiment was performed in triplicates and the same background adjustment was applied to both control and target wells.

6.21 Viability assay

10.000 cells/well HEK293 Flag-Rsa4 WT, E85A or HeLa cells were seeded in 96-well and induced with doxycycline. After 72 hours of induction or treatment with increasing concentrations of small chemical compounds, cells were replaced with fresh medium and 20µL of CellTiter-Blue® Cell Viability Assay (Promega) was added and incubated for 2 hours at 37°C. After incubation, fluorescence was measured with a plate reader at $560_{Ex}/590_{Em}$

6.22 FLAG-Rsa4-UBL purification

3xFlag-Rsa4 WT and mut E85A HEK293 cells, were seeded in twenty 10 cm dish and induced for 24h with 1 µg/ml doxycycline. After induction, the same number of cells was collected and washed three times with PBS 1X Cell lysate was obtained by adding 1 mL of lysis buffer to the pellet, previously frozen in liquid nitrogen with 500 µL Zirconia beads and using beads beater (4 cycles). The obtained cell lysate was incubated in 2,5 mL mobicol (column for affinity purification) overnight with anti-Flag beads. After incubation, the flow through was collected, and beads were washed five times with wash buffer up to 20 mL of total volume. Flag elution was performed using 60 µl of

eluation buffer at 4°C. Samples of the whole cell lysate, flow through and eluate were collected for Western blot and eluate only was collected for Mass-spec analysis.

Cell lysis buffer: 150 mM NaCl, 50 mM K(OAc), 20 mM HEPES (pH 7,5), 2 mM Mg(OAc) 5% Glycerol, NP-40 0,1%, DTT 1mM, Protease inhibitor 1 ml/100ml, RiboLock 1µl/mL and DNase

Wash buffer: 150 mM NaCl, 50 mM K(OAc), 20 mM HEPES (pH 7,5), 2 mM Mg(OAc) 5% Glycerol, NP-40 0,1%, DTT 1mM

Elution buffer: 1X FLAG peptide DYKDDDDK (CASCO) 150 mM NaCl, 50 mM K(OAc), 20 mM HEPES (pH 7,5), 2 mM Mg(OAc) 5% Glycerol, NP-40 0,1%, DTT 1mM,

6.23 Isothermal Titration Calorimetry

Isothermal Titration Calorimetry assay was performed in buffer containing 20 mM HEPES, pH 7.5, 150 mM NaCl, 5mM $MgCl_2$ using protein concentration of 20µM in the cells and 200 µM in the syringe. A single ITC assay, performed at the constant temperature of 25°C, consisted of 1 injection of 0.4 µL and 18 injections of 2 µL each, with a total number of 19 injections of the titrant into the solution in the cell under constant stirring at 750 rpm. Both proteins were carefully dialyzed against the same buffer, before running the experiments. The assay was performed in triplicate.

7. Tables

Plasmids	
Name	**Source**
pET-15b $(His)_6$*Hs* MidasΔloop	this work
pET24d GST-TEV-*Hs* Rsa4-UBL WT 1-104	this work
pET24d GST-TEV-*Hs* Rsa4-UBL WT 11-104	this work
pET24d GST-TEV-*Hs* Rsa4-UBL E85K 1-104	this work
pET24d GST-TEV-*Hs* Rsa4-UBL E85K 11-104	this work
pET24d$(His)_6$Rsa4-UBL 11-104	this work
pcDNA5/FRT/TORpl29-EGFP	(Wild et al; Kutay 2010)
pcDNA5/FRT/TORps2-YFP	(Zemp et al; Kutay 2009)

Softwares	
Name	**website**
MaxQuant	https://www.maxquant.org
Serial cloner 2.6	http://serialbasics.free.fr/Serial_Cloner.html
Protein Imager	https://3dproteinimaging.com/about-us/
Graph Prism	https://www.graphpad.com/scientific-software/prism/
Fiji (ImageJ)	https://imagej.net/software/fiji/
JalView	https://www.jalview.org/
SnapGene	https://www.snapgene.com/
ZEN 3.0	https://www.zeiss.de
Octet Data Analysis HT Software	https://www.sartorius.com
MicroCal PEAQ-ITC family Analysis software	https://www.malvernpanalytical.com

Reagents	
Name	**Brand and code**
Flag peptide (DYKDDDDK)	CASLO
TEV protease	(Parks et al., 1994)
Protease inhibitors	SIGMAFAST Sigma–Aldrich S8830
RiboLock RNase inhibitor	Thermo Fisher Scientific EO0381
Restriction enzymes Thermo	Thermo Fisher Scientific and NEB
DNase I (RNase-free)	NEB M0303S
GenElute HP Plasmid Miniprep Kit	Sigma–Aldrich NA0160
GenElute PCR Clean-up Kit	Sigma–Aldrich NA1020
GenElute Gel Extraction Kit	Sigma–Aldrich NA1111
T4 DNA ligase	NEB M0202
T4 PNK	NEB M0201
Phusion high-Fidelity DNA Polymerase	Thermo Fisher Scientific F530L
IPTG-Dioxan Free	Formedium
Macherey-Nagel™ Protino™ Glutathion-Agarose 4B	Thermo Fisher Scientific 1410/001
Lipofectamine 2000	Thermo Fisher Scientific 11668027
Serva G DNA Staining	SERVA
Page ruler unstained protein ladder	Thermo Fisher Scientific 26614
Macherey-Nagel™ Protino™ Ni-NTA Agarose	Macherey-Nagel 12718702
Cell titer blue®	Promega G8080
Crystal violet	Sigma-Aldrich
Paraformaldehyde Solution 4% in PBS	Thermo Scientific™
Ponceau Red	SERVA SV-0034
Hoechst	Thermo Fisher Scientific
Immobilon™ Western	Merck millipore
Fetal Calf serum	Gibco
Dulbecco's Modified Eagle Medium (DMEM)	Gibco
Cell dissosiation buffer	Gibco
Roti Blue, coomassie® brilliant blue G250	Carl Roth

8. Bibliography

Ahmed, Y.L., Thoms, M., Mitterer, V., Sinning, I., and Hurt, E.J.N.c. (2019). Crystal structures of Rea1-MIDAS bound to its ribosome assembly factor ligands resembling integrin–ligand-type complexes. *10*, 1-14.

Ajore, R., Raiser, D., McConkey, M., Jöud, M., Boidol, B., Mar, B., Saksena, G., Weinstock, D.M., Armstrong, S., and Ellis, S.R.J.E.m.m. (2017). Deletion of ribosomal protein genes is a common vulnerability in human cancer, especially in concert with TP 53 mutations. *9*, 498-507.

Anger, A.M., Armache, J.P., Berninghausen, O., Habeck, M., Subklewe, M., Wilson, D.N., and Beckmann, R. (2013). Structures of the human and Drosophila 80S ribosome. Nature 497, 80–85.

Armache, J.-P., Jarasch, A., Anger, A.M., Villa, E., Becker, T., Bhushan, S., Jossinet, F., Habeck, M., Dindar, G., Franckenberg, S., et al. (2010). Cryo-EM structure and rRNA model of a translating eukaryotic 80S ribosome at 5.5-Å resolution. Proc. Natl. Acad. Sci. 107, 19748–19753.

Axt, K., French, S.L., Beyer, A.L., and Tollervey, D. (2014). Kinetic Analysis Demonstrates a Requirement for the Rat1 Exonuclease in Cotranscriptional Pre-rRNA Cleavage. PLoS One 9, e85703

Bachmann, M., Kukkurainen, S., Hytönen, V.P., and Wehrle-Haller, B.J.P.r. (2019). Cell adhesion by integrins. *99*, 1655-1699.

Ban, N., Nissen, P., Hansen, J., Moore, P.B., and Steitz, T.A.J.S. (2000). The complete atomic structure of the large ribosomal subunit at 2.4 Å resolution. *289*, 905-920.

Barandun, J., Hunziker, M., and Klinge, S.J.C.o.i.s.b. (2018). Assembly and structure of the SSU processome—a nucleolar precursor of the small ribosomal subunit. *49*, 85-93.

Barrio-Garcia, C., Thoms, M., Flemming, D., Kater, L., Berninghausen, O., Baßler, J., Beckmann, R., Hurt, E.J.N.s., and biology, m. (2016). Architecture of the Rix1–Rea1 checkpoint machinery during pre-60S-ribosome remodeling. *23*, 37-44.

Bashan, A., and Yonath, A. (2008). Correlating ribosome function with high-resolution structures. Trends in Microbiology *16*, 326-335.

Baßler, J., and Hurt, E.J.A.r.o.b. (2019). Eukaryotic ribosome assembly. *88*, 281-306.

Baßler, J., Grandi, P., Gadal, O., Leßmann, T., Petfalski, E., Tollervey, D., Lechner, J., and Hurt, E.J.M.c. (2001). Identification of a 60S preribosomal particle that is closely linked to nuclear export. *8*, 517-529.

Baßler, J., Kallas, M., Pertschy, B., Ulbrich, C., Thoms, M., and Hurt, E.J.M.c. (2010). The AAA-ATPase Rea1 drives removal of biogenesis factors during multiple stages of 60S ribosome assembly. *38*, 712-721.

Ben-Shem, A., Garreau de Loubresse, N., Melnikov, S., Jenner, L., Yusupova, G., and Yusupov, M.J.S. (2011). The structure of the eukaryotic ribosome at 3.0 Å resolution. *334*, 1524-1529.

Bradatsch, B., Katahira, J., Kowalinski, E., Bange, G., Yao, W., Sekimoto, T., Baumgärtel, V., Boese, G., Bassler, J., and Wild, K.J.M.c. (2007). Arx1 functions as an unorthodox nuclear export receptor for the 60S preribosomal subunit. *27*, 767-779.

Bradatsch, B., Leidig, C., Granneman, S., Gnädig, M., Tollervey, D., Böttcher, B., Beckmann, R., Hurt, E.J.N.s., and biology, m. (2012). Structure of the pre-60S ribosomal subunit with nuclear export factor Arx1 bound at the exit tunnel. *19*, 1234-1241.

Bruno, P.M., Lu, M., Dennis, K.A., Inam, H., Moore, C.J., Sheehe, J., Elledge, S.J., Hemann, M.T., and Pritchard, J.R.J.P.o.t.N.A.o.S. (2020). The primary mechanism of cytotoxicity of the chemotherapeutic agent CX-5461 is topoisomerase II poisoning. *117*, 4053-4060.

Burger, K., and Eick, D.J.B.C. (2013). Functional ribosome biogenesis is a prerequisite for p53 destabilization: impact of chemotherapy on nucleolar functions and RNA metabolism. *394*, 1133-1143.

Burger, K., Mühl, B., Harasim, T., Rohrmoser, M., Malamoussi, A., Orban, M., Kellner, M., Gruber-Eber, A., Kremmer, E., and Hölzel, M.J.J.o.B.C. (2010). Chemotherapeutic drugs inhibit ribosome biogenesis at various levels. *285*, 12416-12425.

Burroughs, L., Woolfrey, A., and Shimamura, A.J.H.o.c.o.N.A. (2009). Shwachman-Diamond syndrome: a review of the clinical presentation, molecular pathogenesis, diagnosis, and treatment. *23*, 233-248.

Bursać, S., Brdovčak, M.C., Pfannkuchen, M., Orsolić, I., Golomb, L., Zhu, Y., Katz, C., Daftuar, L., Grabušić, K., and Vukelić, I.J.P.o.t.N.A.o.S. (2012). Mutual protection of ribosomal proteins L5 and L11 from degradation is essential for p53 activation upon ribosomal biogenesis stress. *109*, 20467-20472.

Bussiere, C., Hashem, Y., Arora, S., Frank, J., and Johnson, A.W.J.J.o.C.B. (2012). Integrity of the P-site is probed during maturation of the 60S ribosomal subunit. *197*, 747-759.

Carpenter, R.D., Andrei, M., Aina, O.H., Lau, E.Y., Lightstone, F.C., Liu, R., Lam, K.S., and Kurth, M.J.J.J.o.m.c. (2009). Selectively targeting T-and B-cell lymphomas: a benzothiazole antagonist of α4β1 integrin. *52*, 14-19.

Castle, C.D., Cassimere, E.K., and Denicourt, C.J.M.b.o.t.c. (2012). LAS1L interacts with the mammalian Rix1 complex to regulate ribosome biogenesis. *23*, 716-728.

Catez, F., Dalla Venezia, N., Marcel, V., Zorbas, C., Lafontaine, D.L., and Diaz, J.-J.J.B.p. (2019). Ribosome biogenesis: An emerging druggable pathway for cancer therapeutics. *159*, 74-81.

Cavallo, G., Metrangolo, P., Milani, R., Pilati, T., Priimagi, A., Resnati, G., and Terraneo, G.J.C.r. (2016). The halogen bond. *116*, 2478-2601.

Chaker-Margot, M., Barandun, J., Hunziker, M., and Klinge, S.J.S. (2017). Architecture of the yeast small subunit processome. *355*, eaal1880.

Chaker-Margot, M., Hunziker, M., Barandun, J., Dill, B.D., Klinge, S.J.N.s., and biology, m. (2015). Stage-specific assembly events of the 6-MDa small-subunit processome initiate eukaryotic ribosome biogenesis. *22*, 920-923.

Chakraborty, A., Uechi, T., and Kenmochi, N.J.W.I.R.R. (2011). Guarding the 'translation apparatus': defective ribosome biogenesis and the p53 signaling pathway. *2*, 507-522.

Chen, J., Wu, X., Lin, J., Levine, A.J.J.M., and biology, c. (1996). mdm-2 inhibits the G1 arrest and apoptosis functions of the p53 tumor suppressor protein. *16*, 2445-2452.

Chen, K., and Chen, X.J.T. (2011). Integrin targeted delivery of chemotherapeutics. *1*, 189.

Chen, X., Ko, L.J., Jayaraman, L., Prives, C.J.G., and development (1996). p53 levels, functional domains, and DNA damage determine the extent of the apoptotic response of tumor cells. *10*, 2438-2451.

Chen, Z., Suzuki, H., Kobayashi, Y., Wang, A.C., DiMaio, F., Kawashima, S.A., Walz, T., and Kapoor, T.M.J.C. (2018). Structural insights into Mdn1, an essential AAA protein required for ribosome biogenesis. *175*, 822-834. e818.

Cheng, J., Lau, B., La Venuta, G., Ameismeier, M., Berninghausen, O., Hurt, E., and Beckmann, R. (2020). 90S pre-ribosome transformation into the primordial 40S subunit. Science (80-.). 369, 1470–1476.

Chu, S., Archer, R.H., Zengel, J.M., and Lindahl, L. (1994). The RNA of RNase MRP is required for normal processing of ribosomal RNA. Proc. Natl. Acad. Sci. U. S. A. 91, 659–663.

Colis, L., Peltonen, K., Sirajuddin, P., Liu, H., Sanders, S., Ernst, G., Barrow, J.C., and Laiho, M.J.O. (2014). DNA intercalator BMH-21 inhibits RNA polymerase I independent of DNA damage response. *5*, 4361.

Cortez, V., Mann, M., Tekmal, S., Suzuki, T., Miyata, N., Rodriguez-Aguayo, C., Lopez-Berestein, G., Sood, A.K., and Vadlamudi, R.K.J.B.C.R. (2012). Targeting the PELP1-KDM1 axis as a potential therapeutic strategy for breast cancer. *14*, 1-15.

Dang, D.N., Raj, G., Sarode, V., Molberg, K.H., Vadlamudi, R.K., and Peng, Y.J.H.p. (2015). Significantly increased PELP1 protein expression in primary and metastatic triple-negative breast carcinoma: comparison with GATA3 expression and PELP1's potential role in triple-negative breast carcinoma. *46*, 1829-1835.

De Keersmaecker, K., Sulima, S.O., and Dinman, J.D.J.B., The Journal of the American Society of Hematology (2015). Ribosomopathies and the paradox of cellular hypo-to hyperproliferation. *125*, 1377-1382.

de la Cruz, J., Karbstein, K., and Woolford Jr, J.L.J.A.r.o.b. (2015). Functions of ribosomal proteins in assembly of eukaryotic ribosomes in vivo. *84*, 93-129.

Debela, D.T., Muzazu, S.G., Heraro, K.D., Ndalama, M.T., Mesele, B.W., Haile, D.C., Kitui, S.K., and Manyazewal, T.J.S.O.M. (2021). New approaches and procedures for cancer treatment: Current perspectives. *9*, 20503121211034366.

Demoinet, E., Jacquier, A., Lutfalla, G., and Fromont-Racine, M. (2007). The Hsp40 chaperone Jjj1 is required for the nucleo-cytoplasmic recycling of preribosomal factors in Saccharomyces cerevisiae. RNA 13, 1570–1581

Derenzini, M., Montanaro, L., and Trere, D.J.A.h. (2017). Ribosome biogenesis and cancer. *119*, 190-197.

Diamond, M.S., Garcia-Aguilar, J., Bickford, J.K., Corbi, A.L., and Springer, T.A.J.T.J.o.c.b. (1993). The I domain is a major recognition site on the leukocyte integrin Mac-1 (CD11b/CD18) for four distinct adhesion ligands. *120*, 1031-1043.

Donati, G., Peddigari, S., Mercer, C.A., and Thomas, G.J.C.r. (2013). 5S ribosomal RNA is an essential component of a nascent ribosomal precursor complex that regulates the Hdm2-p53 checkpoint. *4*, 87-98.

Dragon, F., Gallagher, J.E., Compagnone-Post, P.A., Mitchell, B.M., Porwancher, K.A., Wehner, K.A., Wormsley, S., Settlage, R.E., Shabanowitz, J., and Osheim, Y.J.N.

(2002). A large nucleolar U3 ribonucleoprotein required for 18S ribosomal RNA biogenesis. *417*, 967-970.

Drygin, D., Lin, A., Bliesath, J., Ho, C.B., O'Brien, S.E., Proffitt, C., Omori, M., Haddach, M., Schwaebe, M.K., and Siddiqui-Jain, A.J.C.r. (2011). Targeting RNA polymerase I with an oral small molecule CX-5461 inhibits ribosomal RNA synthesis and solid tumor growth. *71*, 1418-1430.

Drygin, D., Siddiqui-Jain, A., O'Brien, S., Schwaebe, M., Lin, A., Bliesath, J., Ho, C.B., Proffitt, C., Trent, K., and Whitten, J.P.J.C.r. (2009). Anticancer activity of CX-3543: a direct inhibitor of rRNA biogenesis. *69*, 7653-7661.

Ellis, S.R., and Gleizes, P.-E. (2011). Diamond Blackfan anemia: ribosomal proteins going rogue. Paper presented at: Seminars in hematology (Elsevier).

Ferreira-Cerca, S., Pöll, G., Kühn, H., Neueder, A., Jakob, S., Tschochner, H., and Milkereit, P.J.M.c. (2007). Analysis of the in vivo assembly pathway of eukaryotic 40S ribosomal proteins. *28*, 446-457.

Finkbeiner, E., Haindl, M., and Muller, S.J.T.E.j. (2011). The SUMO system controls nucleolar partitioning of a novel mammalian ribosome biogenesis complex. *30*, 1067-1078.

French, S.L., lebaron, Y.N., Cioci, F., Nomura, M., Beyer, A.L.J.M., and biology, c. (2003). In exponentially growing Saccharomyces cerevisiae cells, rRNA synthesis is determined by the summed RNA polymerase I loading rate rather than by the number of active genes. *23*, 1558-1568.

Frey, S., Richter, R.P., and Görlich, D.J.S. (2006). FG-rich repeats of nuclear pore proteins form a three-dimensional meshwork with hydrogel-like properties. *314*, 815-817.

Fromm, L., Falk, S., Flemming, D., Schuller, J.M., Thoms, M., Conti, E., and Hurt, E.J.N.c. (2017). Reconstitution of the complete pathway of ITS2 processing at the pre-ribosome. *8*, 1-11.

Fromont-Racine, M., Senger, B., Saveanu, C., and Fasiolo, F.J.G. (2003). Ribosome assembly in eukaryotes. *313*, 17-42.

Gadal, O., Strauß, D., Kessl, J., Trumpower, B., Tollervey, D., Hurt, E.J.M., and biology, c. (2001). Nuclear export of 60s ribosomal subunits depends on Xpo1p and requires a nuclear export sequence-containing factor, Nmd3p, that associates with the large subunit protein Rpl10p. *21*, 3405-3415.

Galani, K., Nissan, T.A., Petfalski, E., Tollervey, D., and Hurt, E.J.J.o.B.C. (2004). Rea1, a dynein-related nuclear AAA-ATPase, is involved in late rRNA processing and nuclear export of 60 S subunits. *279*, 55411-55418.

Gallagher, J.E.G., Dunbar, D.A., Granneman, S., Mitchell, B.M., Osheim, Y., Beyer, A.L., and Baserga, S.J. (2004). RNA polymerase I transcription and pre-rRNA processing are linked by specific SSU processome components. Genes Dev. 18, 2506–2517.

Gallegos, K.M., Patel, J.R., Llopis, S.D., Walker, R.R., Davidson, A.M., Zhang, W., Zhang, K., and Tilghman, S.L.J.F.i.O. (2021). Quantitative proteomic profiling identifies a potential novel chaperone marker in resistant breast cancer. 69.

Garbarino, J.E., and Gibbons, I.J.B.g. (2002a). Expression and genomic analysis of midasin, a novel and highly conserved AAA protein distantly related to dynein. *3*, 18.

Gartmann, M., Blau, M., Armache, J.-P., Mielke, T., Topf, M., and Beckmann, R.J.J.o.B.C. (2010). Mechanism of eIF6-mediated inhibition of ribosomal subunit joining. *285*, 14848-14851.

Gasse, L., Flemming, D., and Hurt, E.J.M.c. (2015). Coordinated ribosomal ITS2 RNA processing by the Las1 complex integrating endonuclease, polynucleotide kinase, and exonuclease activities. *60*, 808-815.

Ghalei, H., Schaub, F.X., Doherty, J.R., Noguchi, Y., Roush, W.R., Cleveland, J.L., Elizabeth Stroupe, M., and Karbstein, K. (2015). Hrr25/CK1δ-directed release of Ltv1 from pre-40S ribosomes is necessary for ribosome assembly and cell growth. J. Cell Biol. 208, 745–759.

Goa, K.L., and Noble, S.J.D. (1999). Eptifibatide. *57*, 439-462.

Golomb, L., Volarevic, S., and Oren, M.J.F.l. (2014). p53 and ribosome biogenesis stress: the essentials. *588*, 2571-2579.

Gonugunta, V.K., Miao, L., Sareddy, G.R., Ravindranathan, P., Vadlamudi, R., and Raj, G.V.J.E.-r.c. (2014). The social network of PELP1 and its implications in breast and prostate cancers. *21*, T79-T86.

Grandi, P., Rybin, V., Baßler, J., Petfalski, E., Strauß, D., Marzioch, M., Schäfer, T., Kuster, B., Tschochner, H., and Tollervey, D.J.M.c. (2002). 90S pre-ribosomes include the 35S pre-rRNA, the U3 snoRNP, and 40S subunit processing factors but predominantly lack 60S synthesis factors. *10*, 105-115.

Greber, B.J., Boehringer, D., Montellese, C., Ban, N.J.N.s., and biology, m. (2012). Cryo-EM structures of Arx1 and maturation factors Rei1 and Jjj1 bound to the 60S ribosomal subunit. *19*, 1228-1233.

Gustavsson, P., Willig, T.-N., Haeringen, A.v., Tchernia, G., Dianzani, I., Donnér, M., Elinder, G., Renter, J.-I., Nilsson, P.-G., and Gordon, L.J.N.g. (1997). Diamond-Blackfan anaemia: genetic homogeneity for a gene on chromosome 19q13 restricted to 1.8 Mb. *16*, 368-371.

Haupt, Y.J.n. (1997). Maya r., Kazaz A., Oren M. *387*, 296-299.

Hedges, J., West, M., and Johnson, A.W.J.T.E.j. (2005). Release of the export adapter, Nmd3p, from the 60S ribosomal subunit requires Rpl10p and the cytoplasmic GTPase Lsg1p. *24*, 567-579.

Henras, A.K., Plisson-Chastang, C., O'Donohue, M.F., Chakraborty, A., and Gleizes, P.E.J.W.I.R.R. (2015). An overview of pre-ribosomal RNA processing in eukaryotes. *6*, 225-242.

Henras, A.K., Soudet, J., Gérus, M., Lebaron, S., Caizergues-Ferrer, M., Mougin, A., and Henry, Y. (2008). The post-transcriptional steps of eukaryotic ribosome biogenesis. Cell. Mol. Life Sci. 65, 2334–2359.

Henry, Y., Wood, H., Morrissey, J., Petfalski, E., Kearsey, S., and Tollervey, D.J.T.E.j. (1994). The 5′ end of yeast 5.8 S rRNA is generated by exonucleases from an upstream cleavage site. *13*, 2452-2463.

Hierlmeier, T., Merl, J., Sauert, M., Perez-Fernandez, J., Schultz, P., Bruckmann, A., Hamperl, S., Ohmayer, U., Rachel, R., and Jacob, A.J.N.a.r. (2013). Rrp5p, Noc1p and Noc2p form a protein module which is part of early large ribosomal subunit precursors in S. cerevisiae. *41*, 1191-1210.

Ho, J.H.-N., Kallstrom, G., and Johnson, A.W.J.T.J.o.c.b. (2000). Nmd3p is a Crm1p-dependent adapter protein for nuclear export of the large ribosomal subunit. *151*, 1057-1066.

Hock, A.K., and Vousden, K.H.J.B.e.B.A.-M.C.R. (2014). The role of ubiquitin modification in the regulation of p53. *1843*, 137-149.

Honda, R., Tanaka, H., and Yasuda, H.J.F.l. (1997). Oncoprotein MDM2 is a ubiquitin ligase E3 for tumor suppressor p53. *420*, 25-27.

Irfan, A., Batool, F., Zahra Naqvi, S.A., Islam, A., Osman, S.M., Nocentini, A., Alissa, S.A., Supuran, C.T.J.J.o.e.i., and chemistry, m. (2020). Benzothiazole derivatives as anticancer agents. *35*, 265-279.

Ismail, S., Flemming, D., Thoms, M., Gomes-Filho, J.V., Randau, L., Beckmann, R., and Hurt, E.J.C.R. (2022). Emergence of the primordial pre-60S from the 90S pre-ribosome. *39*, 110640.

Kampen, K.R., Sulima, S.O., Vereecke, S., and De Keersmaecker, K.J.N.a.r. (2020). Hallmarks of ribosomopathies. *48*, 1013-1028.

Karbstein, K.J.C.o.i.c.b. (2011). Inside the 40S ribosome assembly machinery. *15*, 657-663.

Karbstein, K.J.T.i.c.b. (2013). Quality control mechanisms during ribosome maturation. *23*, 242-250.

Kargas, V., Castro-Hartmann, P., Escudero-Urquijo, N., Dent, K., Hilcenko, C., Sailer, C., Zisser, G., Marques-Carvalho, M.J., Pellegrino, S., and Wawiórka, L.J.E. (2019). Mechanism of completion of peptidyltransferase centre assembly in eukaryotes. *8*, e44904.

Karimzadeh, F., Modarres Mousavi, S.M., Alipour, F., Hosseini Ravandi, H., Kovac, S., Gorji, A.J.B.S., and Function (2017). Developmental changes in Notch1 and NLE1 expression in a genetic model of absence epilepsy. *222*, 2773-2785.

Kater, L., Thoms, M., Barrio-Garcia, C., Cheng, J., Ismail, S., Ahmed, Y.L., Bange, G., Kressler, D., Berninghausen, O., and Sinning, I.J.C. (2017). Visualizing the assembly pathway of nucleolar pre-60S ribosomes. *171*, 1599-1610. e1514.

Kemmler, S., Occhipinti, L., Veisu, M., and Panse, V.G.J.J.o.C.B. (2009). Yvh1 is required for a late maturation step in the 60S biogenesis pathway. *186*, 863-880.

Khatter, H., Myasnikov, A.G., Natchiar, S.K., and Klaholz, B.P. (2015). Structure of the human 80S ribosome. Nature 520, 640–645

Khot, A., Brajanovski, N., Cameron, D.P., Hein, N., Maclachlan, K.H., Sanij, E., Lim, J., Soong, J., Link, E., and Blombery, P.J.C.d. (2019). First-in-human RNA polymerase I transcription inhibitor CX-5461 in patients with advanced hematologic cancers: results of a phase I dose-escalation study. *9*, 1036-1049.

Klingauf-Nerurkar, P., Gillet, L.C., Portugal-Calisto, D., Oborská-Oplová, M., Jäger, M., Schubert, O.T., Pisano, A., Peña, C., Rao, S., and Altvater, M.J.E. (2020). The GTPase Nog1 co-ordinates the assembly, maturation and quality control of distant ribosomal functional centers. *9*, e52474.

Klinge, S., and Woolford, J.L.J.N.r.M.c.b. (2019). Ribosome assembly coming into focus. *20*, 116-131.

Kornprobst, M., Turk, M., Kellner, N., Cheng, J., Flemming, D., Koš-Braun, I., Koš, M., Thoms, M., Berninghausen, O., and Beckmann, R.J.C. (2016). Architecture of the 90S pre-ribosome: a structural view on the birth of the eukaryotic ribosome. *166*, 380-393.

Koš, M., and Tollervey, D.J.M.c. (2010). Yeast pre-rRNA processing and modification occur cotranscriptionally. *37*, 809-820.

Kressler, D., Hurt, E., and Baßler, J.J.T.i.b.s. (2017). A puzzle of life: crafting ribosomal subunits. *42*, 640-654.

Kressler, D., Hurt, E., and Baβler, J.J.B.E.B.A.-M.C.R. (2010). Driving ribosome assembly. *1803*, 673-683.

Krogan, N.J., Peng, W.-T., Cagney, G., Robinson, M.D., Haw, R., Zhong, G., Guo, X., Zhang, X., Richards, D.P., and Beattie, B.K.J.M.c. (2004). High-definition macromolecular composition of yeast RNA-processing complexes. *13*, 225-239.

Lamanna, A.C., and Karbstein, K.J.P.o.t.N.A.o.S. (2009). Nob1 binds the single-stranded cleavage site D at the 3′-end of 18S rRNA with its PIN domain. *106*, 14259-14264.

Larson, R.S., Corbi, A.L., Berman, L., and Springer, T.J.T.J.o.c.b. (1989). Primary structure of the leukocyte function-associated molecule-1 alpha subunit: an integrin with an embedded domain defining a protein superfamily. *108*, 703-712.

Lau, B., Cheng, J., Flemming, D., La Venuta, G., Berninghausen, O., Beckmann, R., and Hurt, E.J.M.C. (2021). Structure of the maturing 90S pre-ribosome in association with the RNA exosome. *81*, 293-303. e294.

Lebaron, S., Segerstolpe, Å., French, S.L., Dudnakova, T., de Lima Alves, F., Granneman, S., Rappsilber, J., Beyer, A.L., Wieslander, L., and Tollervey, D.J.M.c. (2013). Rrp5 binding at multiple sites coordinates pre-rRNA processing and assembly. *52*, 707-719.

Lee, S.J., Baserga, S.J.J.M., and Biology, C. (1999). Imp3p and Imp4p, two specific components of the U3 small nucleolar ribonucleoprotein that are essential for pre-18S rRNA processing. *19*, 5441-5452.

Leidig, C., Thoms, M., Holdermann, I., Bradatsch, B., Berninghausen, O., Bange, G., Sinning, I., Hurt, E., and Beckmann, R.J.N.c. (2014). 60S ribosome biogenesis requires rotation of the 5S ribonucleoprotein particle. *5*, 1-8.

Li, Y., Zhou, Y., Li, B., Chen, F., Shen, W., Lu, Y., Zhong, C., Zhang, C., Xie, H., and Katanaev, V.L.J.O. (2020). WDR74 modulates melanoma tumorigenesis and metastasis through the RPL5–MDM2–p53 pathway. *39*, 2741-2755.

Liang, X., Zuo, M.-Q., Zhang, Y., Li, N., Ma, C., Dong, M.-Q., and Gao, N.J.N.c. (2020). Structural snapshots of human pre-60S ribosomal particles before and after nuclear export. *11*, 1-14.

Lindahl, L., Archer, R.H., and Zengel, J.M. (1992). A new rRNA processing mutant of Saccharomyces cerevisiae. Nucleic Acids Res. 20, 295–301.

Lindahl, L., Bommankanti, A., Li, X., Hayden, L., Jones, A., Khan, M., Oni, T., and Zengel, J.M.J.R. (2009). RNase MRP is required for entry of 35S precursor rRNA into the canonical processing pathway. *15*, 1407-1416.

Lo, K.-Y., Li, Z., Bussiere, C., Bresson, S., Marcotte, E.M., and Johnson, A.W.J.M.c. (2010). Defining the pathway of cytoplasmic maturation of the 60S ribosomal subunit. *39*, 196-208.

Lo, K.-Y., Li, Z., Wang, F., Marcotte, E.M., and Johnson, A.W.J.J.o.C.B. (2009). Ribosome stalk assembly requires the dual-specificity phosphatase Yvh1 for the exchange of Mrt4 with P0. *186*, 849-862.

Loibl, M., Klein, I., Prattes, M., Schmidt, C., Kappel, L., Zisser, G., Gungl, A., Krieger, E., Pertschy, B., and Bergler, H.J.J.o.B.C. (2014). The drug diazaborine blocks ribosome biogenesis by inhibiting the AAA-ATPase Drg1. *289*, 3913-3922.

Lossie, A.C., Lo, C.-L., Baumgarner, K.M., Cramer, M.J., Garner, J.P., and Justice, M.J.J.B.g. (2012). ENU mutagenesis reveals that Notchless homolog 1 (Drosophila) affects Cdkn1a and several members of the Wnt pathway during murine pre-implantation development. *13*, 1-16.

Luo, B.-H., Carman, C.V., and Springer, T.A.J.A.R.I. (2007). Structural basis of integrin regulation and signaling. *25*, 619-647.

Lygerou, Z., Allmang, C., Tollervey, D., and Séraphin, B.J.S. (1996). Accurate processing of a eukaryotic precursor ribosomal RNA by ribonuclease MRP in vitro. *272*, 268-270.

Ma, C., Wu, S., Li, N., Chen, Y., Yan, K., Li, Z., Zheng, L., Lei, J., Woolford, J.L., and Gao, N. (2017). Structural snapshot of cytoplasmic pre-60S ribosomal particles bound with Nmd3, Lsg1, Tif6 and Reh1. Nat. Struct. Mol. Biol. 24, 214–220

Maiorov, V.N., and Crippen, G.M.J.J.o.m.b. (1994). Significance of root-mean-square deviation in comparing three-dimensional structures of globular proteins. *235*, 625-634.

Matsui, K., Giri, N., Alter, B.P., and Pinto, L.A.J.B.j.o.h. (2013). Cytokine production by bone marrow mononuclear cells in inherited bone marrow failure syndromes. *163*, 81-92.

Matsuo, Y., Granneman, S., Thoms, M., Manikas, R.-G., Tollervey, D., and Hurt, E.J.N. (2014). Coupled GTPase and remodelling ATPase activities form a checkpoint for ribosome export. *505*, 112-116.

McClellan, K.J., and Goa, K.L.J.D. (1998). Tirofiban. *56*, 1067-1080.

Mélèse, T., and Xue, Z.J.C.o.i.c.b. (1995). The nucleolus: an organelle formed by the act of building a ribosome. *7*, 319-324.

Melnikov, S., Ben-Shem, A., De Loubresse, N.G., Jenner, L., Yusupova, G., Yusupov, M.J.N.s., and biology, m. (2012). One core, two shells: bacterial and eukaryotic ribosomes. *19*, 560-567.

Mezu-Ndubuisi, O.J., and Maheshwari, A.J.P.r. (2021). The role of integrins in inflammation and angiogenesis. *89*, 1619-1626.

Michishita, M., Videm, V., and Arnaout, M.A.J.C. (1993). A novel divalent cation-binding site in the A domain of the β2 integrin CR3 (CD11b/CD18) is essential for ligand binding. *72*, 857-867.

Mickolajczyk, K.J., Olinares, P.D.B., Chait, B.T., Liu, S., and Kapoor, T.M.J.e. (2022). The MIDAS domain of AAA mechanoenzyme Mdn1 forms catch bonds with two different substrates. *11*, e73534.

Miles, T.D., Jakovljevic, J., Horsey, E.W., Harnpicharnchai, P., Tang, L., Woolford Jr, J.L.J.M., and biology, c. (2005). Ytm1, Nop7, and Erb1 form a complex necessary for maturation of yeast 66S pre-ribosomes. *25*, 10419-10432.

Mills, E.W., and Green, R.J.S. (2017). Ribosomopathies: There's strength in numbers. *358*, eaan2755.

Mitchell, P., Petfalski, E., Shevchenko, A., Mann, M., and Tollervey, D. (1997). The exosome: A conserved eukaryotic RNA processing complex containing multiple 3'→5' exoribonucleases. Cell 91, 457–466.

Mitterer, V., Murat, G., Réty, S., Blaud, M., Delbos, L., Stanborough, T., Bergler, H., Leulliot, N., Kressler, D., and Pertschy, B.J.N.c. (2016). Sequential domain assembly of ribosomal protein S3 drives 40S subunit maturation. *7*, 1-15.

Moll, U.M., and Petrenko, O.J.M.c.r. (2003). The MDM2-p53 interaction. *1*, 1001-1008.

Momand, J., Zambetti, G.P., Olson, D.C., George, D., and Levine, A.J.J.c. (1992). The mdm-2 oncogene product forms a complex with the p53 protein and inhibits p53-mediated transactivation. *69*, 1237-1245.

Nerurkar, P., Altvater, M., Gerhardy, S., Schütz, S., Fischer, U., Weirich, C., Panse, V.G.J.I.r.o.c., and biology, m. (2015). Eukaryotic ribosome assembly and nuclear export. *319*, 107-140.

Ning, Z., Zhang, Y., Chen, H., Wu, J., Song, T., Wu, Q., Liu, F.J.O.m., and longevity, c. (2014). PELP1 suppression inhibits colorectal cancer through c-Src downregulation. *2014*.

Nissan, T.A., Baßler, J., Petfalski, E., Tollervey, D., and Hurt, E.J.T.E.j. (2002). 60S pre-ribosome formation viewed from assembly in the nucleolus until export to the cytoplasm. *21*, 5539-5547.

Nissan, T.A., Galani, K., Maco, B., Tollervey, D., Aebi, U., and Hurt, E.J.M.c. (2004). A pre-ribosome with a tadpole-like structure functions in ATP-dependent maturation of 60S subunits. *15*, 295-301.

Oeffinger, M., Zenklusen, D., Ferguson, A., Wei, K.E., El Hage, A., Tollervey, D., Chait, B.T., Singer, R.H., and Rout, M.P. (2009). Rrp17p Is a Eukaryotic Exonuclease Required for 5′ End Processing of Pre-60S Ribosomal RNA. Mol. Cell 36, 768–781.

Ogle, J.M., and Ramakrishnan, V.J.A.R.B. (2005). Structural insights into translational fidelity. *74*, 129-177.

Ogura, T., and Wilkinson, A.J.J.G.t.C. (2001). AAA+ superfamily ATPases: common structure–diverse function. *6*, 575-597.

Osheim, Y.N., French, S.L., Keck, K.M., Champion, E.A., Spasov, K., Dragon, F., Baserga, S.J., and Beyer, A.L. (2004). Pre-18S ribosomal RNA is structurally compacted into the SSU processome prior to being cleaved from nascent transcripts in Saccharomyces cerevisiae. Mol. Cell 16, 943–954.

Panse, V.G., and Johnson, A.W.J.T.i.b.s. (2010). Maturation of eukaryotic ribosomes: acquisition of functionality. *35*, 260-266.

Parker, J.J.M.r. (1989). Errors and alternatives in reading the universal genetic code. *53*, 273-298.

Patchett, S., Musalgaonkar, S., Malyutin, A.G., and Johnson, A.W.J.P.g. (2017). The T-cell leukemia related rpl10-R98S mutant traps the 60S export adapter Nmd3 in the ribosomal P site in yeast. *13*, e1006894.

Pelletier, J., Thomas, G., and Volarević, S.J.N.R.C. (2018). Ribosome biogenesis in cancer: new players and therapeutic avenues. *18*, 51-63.

Peltonen, K., Colis, L., Liu, H., Trivedi, R., Moubarek, M.S., Moore, H.M., Bai, B., Rudek, M.A., Bieberich, C.J., and Laiho, M.J.C.c. (2014). A targeting modality for destruction of RNA polymerase I that possesses anticancer activity. *25*, 77-90.

Penzo, M., Montanaro, L., Treré, D., and Derenzini, M.J.C. (2019). The ribosome biogenesis—cancer connection. *8*, 55.

Perez-Fernandez, J., Martín-Marcos, P., and Dosil, M.J.N.a.r. (2011). Elucidation of the assembly events required for the recruitment of Utp20, Imp4 and Bms1 onto nascent pre-ribosomes. *39*, 8105-8121.

Pertschy, B., Saveanu, C., Zisser, G., Lebreton, A., Tengg, M., Jacquier, A., Liebminger, E., Nobis, B., Kappel, L., Van der Klei, I.J.M.*, et al.* (2007). Cytoplasmic recycling of 60S preribosomal factors depends on the AAA protein Drg1. *27*, 6581-6592.

Pertschy, B., Schneider, C., Gnädig, M., Schäfer, T., Tollervey, D., and Hurt, E.J.J.o.B.C. (2009). RNA helicase Prp43 and its co-factor Pfa1 promote 20 to 18 S rRNA processing catalyzed by the endonuclease Nob1. *284*, 35079-35091.

Pertschy, B.J.M.C. (2017). When a ribosomal protein grows up-the ribosome assembly path of Rps3. *4*, 140.

Pöll, G., Li, S., Ohmayer, U., Hierlmeier, T., Milkereit, P., and Perez-Fernandez, J. (2014). In Vitro Reconstitution of Yeast tUTP/UTP A and UTP B Subcomplexes Provides New Insights into Their Modular Architecture. PLoS One 9, e114898.

Prattes, M., Lo, Y.-H., Bergler, H., and Stanley, R.E.J.B. (2019). Shaping the nascent ribosome: AAA-ATPases in eukaryotic ribosome biogenesis. *9*, 715.

Raman, N., Weir, E., and Müller, S.J.M.c. (2016). The AAA ATPase MDN1 acts as a SUMO-targeted regulator in mammalian pre-ribosome remodeling. *64*, 607-615.

Ren, Z., Ni, F., Zhang, T., Yuan, X., and Li, J.J.E.C.R. (2021). Knockdown of NLE1 inhibits development of malignant melanoma in vitro and in vivo NLE1 promotes development of malignant melanoma. *404*, 112636.

Romes, E.M., Sobhany, M., and Stanley, R.E.J.J.o.B.C. (2016). The crystal structure of the ubiquitin-like domain of ribosome assembly factor Ytm1 and characterization of its interaction with the AAA-ATPase midasin. *291*, 882-893.

Ruoslahti, E.J.A.r.o.c., and biology, d. (1996). RGD and other recognition sequences for integrins. *12*, 697-715.

Sanghai, Z.A., Miller, L., Molloy, K.R., Barandun, J., Hunziker, M., Chaker-Margot, M., Wang, J., Chait, B.T., and Klinge, S.J.N. (2018). Modular assembly of the nucleolar pre-60S ribosomal subunit. *556*, 126-129.

Sareddy, Gangadhara Reddy, and Ratna K. Vadlamudi. "PELP1: Structure, biological function and clinical significance." *Gene* 585.1 (2016): 128-134

Saveanu, C., Namane, A., Gleizes, P.-E., Lebreton, A., Rousselle, J.-C., Noaillac-Depeyre, J., Gas, N., Jacquier, A., Fromont-Racine, M.J.M., and biology, c. (2003). Sequential protein association with nascent 60S ribosomal particles. *23*, 4449-4460.

Schäfer, T., Maco, B., Petfalski, E., Tollervey, D., Böttcher, B., Aebi, U., and Hurt, E.J.N. (2006). Hrr25-dependent phosphorylation state regulates organization of the pre-40S subunit. *441*, 651-655.

Schäfer, T., Strauß, D., Petfalski, E., Tollervey, D., and Hurt, E. (2003). The path from nucleolar 90S to cytoplasmic 40S pre-ribosomes. EMBO J. 22, 1370–1380.

Schaller, D., Šribar, D., Noonan, T., Deng, L., Nguyen, T.N., Pach, S., Machalz, D., Bermudez, M., and Wolber, G.J.W.I.R.C.M.S. (2020). Next generation 3D pharmacophore modeling. *10*, e1468.

Schluenzen, F., Tocilj, A., Zarivach, R., Harms, J., Gluehmann, M., Janell, D., Bashan, A., Bartels, H., Agmon, I., and Franceschi, F.J.c. (2000). Structure of functionally activated small ribosomal subunit at 3.3 Å resolution. *102*, 615-623.

Schmitt, M.E., Clayton, D.A.J.M., and biology, c. (1993). Nuclear RNase MRP is required for correct processing of pre-5.8 S rRNA in Saccharomyces cerevisiae. *13*, 7935-7941.

Schuller, J.M., Falk, S., Fromm, L., Hurt, E., and Conti, E. (2018). Structure of the nuclear exosome captured on a maturing preribosome. Science (80-.). 360, 219–222.

Shimaoka, M., Xiao, T., Liu, J.-H., Yang, Y., Dong, Y., Jun, C.-D., McCormack, A., Zhang, R., Joachimiak, A., and Takagi, J.J.C. (2003). Structures of the αL I domain and its complex with ICAM-1 reveal a shape-shifting pathway for integrin regulation. *112*, 99-111.

Slack, R., Macdonald, S., Roper, J., Jenkins, R., and Hatley, R.J.N.R.D.D. (2021). Emerging therapeutic opportunities for integrin inhibitors. 1-19.

Smith, C.E.P., and Prasad, V.J.A.F.P. (2021). Targeted Cancer Therapies. *103*, 155-163.

Sökeland, G., and Schumacher, U.J.M.C. (2019). The functional role of integrins during intra-and extravasation within the metastatic cascade. *18*, 1-19.

Song, G., Yang, Y., Liu, J.-h., Casasnovas, J.M., Shimaoka, M., Springer, T.A., and Wang, J.-h.J.P.o.t.N.A.o.S. (2005). An atomic resolution view of ICAM recognition in a complex between the binding domains of ICAM-3 and integrin αLβ2. *102*, 3366-3371.

Sosnowski, P., Urnavicius, L., Boland, A., Fagiewicz, R., Busselez, J., Papai, G., and Schmidt, H.J.E. (2018). The CryoEM structure of the Saccharomyces cerevisiae ribosome maturation factor Rea1. *7*, e39163.

Strunk, B.S., and Karbstein, K.J.R. (2009). Powering through ribosome assembly. *15*, 2083-2104.

Strunk, B.S., Loucks, C.R., Su, M., Vashisth, H., Cheng, S., Schilling, J., Brooks III, C.L., Karbstein, K., and Skiniotis, G.J.S. (2011). Ribosome assembly factors prevent premature translation initiation by 40 S assembly intermediates. 333, 1449-1453.

Strunk, B.S., Novak, M.N., Young, C.L., and Karbstein, K.J.C. (2012). A translation-like cycle is a quality control checkpoint for maturing 40S ribosome subunits. *150*, 111-121.

Sulima, S.O., Patchett, S., Advani, V.M., De Keersmaecker, K., Johnson, A.W., and Dinman, J.D.J.P.o.t.N.A.o.S. (2014). Bypass of the pre-60S ribosomal quality control as a pathway to oncogenesis. *111*, 5640-5645.

Sun, Q., Zhu, X., Qi, J., An, W., Lan, P., Tan, D., Chen, R., Wang, B., Zheng, S., Zhang, C., et al. (2017). Molecular architecture of the 90S small subunit pre-ribosome. Elife 6.

Swift, L.H., and Golsteyn, R.M.J.I.j.o.m.s. (2014). Genotoxic anti-cancer agents and their relationship to DNA damage, mitosis, and checkpoint adaptation in proliferating cancer cells. *15*, 3403-3431.

Takada, Y., Ye, X., and Simon, S.J.G.b. (2007). The integrins. *8*, 1-9.

Thoms, M., Ahmed, Y.L., Maddi, K., Hurt, E., and Sinning, I.J.N.a.r. (2016). Concerted removal of the Erb1–Ytm1 complex in ribosome biogenesis relies on an elaborate interface. *44*, 926-939.

Thoms, M., Mitterer, V., Kater, L., Falquet, L., Beckmann, R., Kressler, D., and Hurt, E.J.N.c. (2018). Suppressor mutations in Rpf2–Rrs1 or Rpl5 bypass the Cgr1 function for pre-ribosomal 5S RNP-rotation. *9*, 1-13.

Thoms, M., Thomson, E., Baßler, J., Gnädig, M., Griesel, S., and Hurt, E.J.C. (2015). The exosome is recruited to RNA substrates through specific adaptor proteins. *162*, 1029-1038.

Thomson, E., Tollervey, D.J.M., and biology, c. (2010). The final step in 5.8 S rRNA processing is cytoplasmic in Saccharomyces cerevisiae. *30*, 976-984.

Tomecki, R., Sikorski, P.J., and Zakrzewska-Placzek, M.J.F.l. (2017). Comparison of preribosomal RNA processing pathways in yeast, plant and human cells–focus on coordinated action of endo-and exoribonucleases. *591*, 1801-1850.

Tozer, E.C., Liddington, R.C., Sutcliffe, M.J., Smeeton, A.H., and Loftus, J.C.J.J.o.B.C. (1996). Ligand binding to integrin αIIbβ3 is dependent on a MIDAS-like domain in the β3 subunit. *271*, 21978-21984.

Turi, Z., Lacey, M., Mistrik, M., and Moudry, P.J.A. (2019). Impaired ribosome biogenesis: mechanisms and relevance to cancer and aging. *11*, 2512.

Turowski, T.W., Lebaron, S., Zhang, E., Peil, L., Dudnakova, T., Petfalski, E., Granneman, S., Rappsilber, J., and Tollervey, D.J.N.a.r. (2014). Rio1 mediates ATP-dependent final maturation of 40S ribosomal subunits. *42*, 12189-12199.

Udem, S.A., and Warner, J.R.J.J.o.m.b. (1972). Ribosomal RNA synthesis in Saccharomyces cerevisiae. *65*, 227-242.

Ulbrich, C., Diepholz, M., Baßler, J., Kressler, D., Pertschy, B., Galani, K., Böttcher, B., and Hurt, E.J.C. (2009). Mechanochemical removal of ribosome biogenesis factors from nascent 60S ribosomal subunits. *138*, 911-922.

Velculescu, V.E., Zhang, L., Zhou, W., Vogelstein, J., Basrai, M.A., Bassett Jr, D.E., Hieter, P., Vogelstein, B., and Kinzler, K.W.J.C. (1997). Characterization of the yeast transcriptome. *88*, 243-251.

Venturi, G., and Montanaro, L.J.C. (2020). How altered ribosome production can cause or contribute to human disease: the spectrum of ribosomopathies. *9*, 2300.

Walker, R.R., Gallegos, K.M., Bratton, M.R., Lemieux, K.P., Zhang, K., Wang, G., Davidson, A.M., and Tilghman, S.L.J.A.r. (2021). Acquisition of Letrozole Resistance Through Activation of the p38/MAPK Signaling Cascade. *41*, 583-599.

Wang, X., Tsang, J.Y., Lee, M.A., Ni, Y.-B., Tong, J.H., Chan, S.-K., Cheung, S.-Y., To, K.F., Tse, G.M.J.C.R., and Association, T.O.J.o.K.C. (2019). The clinical value of PELP1 for breast cancer: a comparison with multiple cancers and analysis in breast cancer subtypes. *51*, 706.

Warner, J.R.J.T.i.b.s. (1999). The economics of ribosome biosynthesis in yeast. *24*, 437-440.

Wells, G.R., Weichmann, F., Colvin, D., Sloan, K.E., Kudla, G., Tollervey, D., Watkins, N.J., and Schneider, C.J.N.a.r. (2016). The PIN domain endonuclease Utp24 cleaves pre-ribosomal RNA at two coupled sites in yeast and humans. *44*, 5399-5409.

Wermelinger, L.S., Geraldo, R.B., Frattani, F.S., Rodrigues, C.R., Juliano, M.A., Castro, H.C., Zingali, R.B.J.A.o.b., and biophysics (2009). Integrin inhibitors from

snake venom: Exploring the relationship between the structure and activity of RGD-peptides. *482*, 25-32.

West, M., Hedges, J.B., Chen, A., Johnson, A.W.J.M., and biology, c. (2005). Defining the order in which Nmd3p and Rpl10p load onto nascent 60S ribosomal subunits. *25*, 3802-3813.

Wild, K., Aleksić, M., Lapouge, K., Juaire, K.D., Flemming, D., Pfeffer, S., and Sinning, I.J.N.c. (2020). MetAP-like Ebp1 occupies the human ribosomal tunnel exit and recruits flexible rRNA expansion segments. *11*, 1-10

Wild, T., Horvath, P., Wyler, E., Widmann, B., Badertscher, L., Zemp, I., Kozak, K., Csucs, G., Lund, E., and Kutay, U.J.P.b. (2010). A protein inventory of human ribosome biogenesis reveals an essential function of exportin 5 in 60S subunit export. *8*, e1000522.

Wimberly, B.T., Brodersen, D.E., Clemons, W.M., Morgan-Warren, R.J., Carter, A.P., Vonrhein, C., Hartsch, T., and Ramakrishnan, V.J.N. (2000). Structure of the 30S ribosomal subunit. *407*, 327-339.

Wu, S., Tutuncuoglu, B., Yan, K., Brown, H., Zhang, Y., Tan, D., Gamalinda, M., Yuan, Y., Li, Z., and Jakovljevic, J.J.N. (2016). Diverse roles of assembly factors revealed by structures of late nuclear pre-60S ribosomes. *534*, 133-137.

Yao, W., Roser, D., Köhler, A., Bradatsch, B., Baßler, J., and Hurt, E.J.M.c. (2007). Nuclear export of ribosomal 60S subunits by the general mRNA export receptor Mex67-Mtr2. *26*, 51-62.

Yusupov, M.M., Yusupova, G.Z., Baucom, A., Lieberman, K., Earnest, T.N., Cate, J.H.D., and Noller, H.F. (2001). Crystal Structure of the Ribosome at 5.5 Å Resolution. Science (80-.). 292, 883–896

Yusupova, G., and Yusupov, M.J.A.r.o.b. (2014). High-resolution structure of the eukaryotic 80S ribosome. *83*, 467-486.

Zemp, I., Wild, T., O'Donohue, M.-F., Wandrey, F., Widmann, B., Gleizes, P.-E., and Kutay, U.J.J.o.C.B. (2009). Distinct cytoplasmic maturation steps of 40S ribosomal subunit precursors require hRio2. *185*, 1167-1180.

Zhang, J., Harnpicharnchai, P., Jakovljevic, J., Tang, L., Guo, Y., Oeffinger, M., Rout,

Zheng, J., Lang, Y., Zhang, Q., Cui, D., Sun, H., Jiang, L., Chen, Z., Zhang, R., Gao, Y., Tian, W.J.G*., et al.* (2015). Structure of human MDM2 complexed with RPL11 reveals the molecular basis of p53 activation. *29*, 1524-1534.

Zhou, D., Zhu, X., Zheng, S., Tan, D., Dong, M.-Q., Ye, K.J.P., and cell (2019). Cryo-EM structure of an early precursor of large ribosomal subunit reveals a half-assembled intermediate. *10*, 120-130.

Zhang, J., Harnpicharnchai, P., Jakovljevic, J., Tang, L., Guo, Y., Oeffinger, M., Rout, M.P., Hiley, S.L., Hughes, T., Woolford, J.L.J.G*., et al.* (2007). Assembly factors Rpf2 and Rrs1 recruit 5S rRNA and ribosomal proteins rpL5 and rpL11 into nascent ribosomes. *21*, 2580-2592.

Zhang, L., Wu, C., Cai, G., Chen, S., Ye, K.J.G., and development (2016). Stepwise and dynamic assembly of the earliest precursors of small ribosomal subunits in yeast. *30*, 718-732.

Zhou, D., Zhu, X., Zheng, S., Tan, D., Dong, M.-Q., Ye, K.J.P., and cell (2019a). Cryo-EM structure of an early precursor of large ribosomal subunit reveals a half-assembled intermediate. *10*, 120-130.

Zhou, Y., Musalgaonkar, S., Johnson, A.W., and Taylor, D.W.J.N.c. (2019b). Tightly-orchestrated rearrangements govern catalytic center assembly of the ribosome. *10*, 1-11.

Zisi, A., Bartek, J., and Lindström, M.S.J.C. (2022). Targeting Ribosome Biogenesis in Cancer: Lessons Learned and Way Forward. *14*, 2126.

Zisser, G., Ohmayer, U., Mauerhofer, C., Mitterer, V., Klein, I., Rechberger, G.N., Wolinski, H., Prattes, M., Pertschy, B., and Milkereit, P.J.N.A.R. (2018). Viewing pre-60S maturation at a minute's timescale. *46*, 3140-3151.

Acknowledgements

At the end of this journey, I would like to thank all the people who supported, helped, and chaperoned me during these last 4 years and half.
As first, Prof. Dr. Ed Hurt, of course, because when I applied to the lab I was not even done with my master thesis and my English was not the best, but you still you gave me the possibility to join the lab, learn, grow day by day and becoming a much expert scientist. Thank you very, very much.
Thank you to my PhD examination committee: Prof. Dr Irmi Sinning, Dr. Christoph Müller, and Dr. Mandy Jeske, for all the availability. Thank you very much Klemens, you were always nice and encouraging to me and always there to help and explain me things. Thank you to the Beckmann lab and Matthias Thoms and Wolber lab and Theresa Noonan for their contribution to this project.
I would like to thank all the Hurties, and all the people were always available there for me for a scientific advice, technical support or only to share a coffee or a lunch. Thank you very much Sabine, Ruth, and Martina, I really loved working with you, you are very bright people, and I could not make it without your help. Thank so much Andrea, you were there every time I needed, and your smile, positivity, efficiency, and support helped me so much during these years! Grazie di cuore (San) Giuseppe for helping me not to give up and thank you for being the best teacher of the world; Valentin, Ingo, thank you very much for all the advice and the help. You were always there for me, suggesting nice ideas, answering my questions and helping me every time I needed. Thank you, Nestor, for believing in my “cell culture skills”, I was very happy to be part of your PhD journey and thesis! Thank you Jochen for all the advice and the support. During the last year I felt that you were really believing in my scientific skills, and this made me feel understood and gratified. Thank you very much!
Thank you, Matthias, you made me work super hard already the first day I started the PhD and this helped me a lot in the long term. The support you gave me in 3-4 months helped me making it until the end. The help you are giving me now, as collaborator, is helping me even more. Olga, thank you very much because with your smile and positivity, you made me feel much better most of the times I felt down. You are a great person and a great scientist!. Para ti, Selene, minha professora de português. Muito obrigada por toda a ajuda, pelas risadas e pela boa conversa que tivemos juntos. Foi um prazer conhecer e trabalhar juntos. Ficas sempre assim, não mude nunca!
To my amazing friends, Sven and Sherif! I love you so much! I could not make it without you, our lunches, coffee breaks, and laughs together. I wish you all the best for your future and to

realize all your dreams! Ricardo, who in the last four years was the one always seeing me at my worst and trying to make me feel better everytime I felt overwhelmed. Thank you for the patience you had in the last 4 months of my thesis, in which I was always in a bad mood at home and especially thank you for being in my life. I love you. Thank you to the Jeske group and Mandy, Jana and everyone else for being always welcoming with us and for creating a great environment on the 4th floor. Harpreet, love you! Your chai made most of my days, I loved becoming your friend and spending time with you! Thank you, Anna and Fidel, for your great friendship and all the time spent together. It was really precious for me. Al lab Costanzo, la prof, Elena, Gaetano e Giancarlo, se sono qui oggi è grazie a voi. Il lab Costanzo è dove tutto è iniziato ed è stato e sempre sarà il motivo per cui amo la scienza. Ai miei genitori e nonna al loro immenso coraggio nel lasciarmi andare 4 anni e mezzo fa. To Flora, thanks for doing this journey together with me, for the advice and support and especially for dealing with my unsustainable negative thoughts. We started and finished together, and I could not be happier for us.

To Clorinda and Marika, friends for more than 20 years. Many Km separates us, but we are always us, and I love it. To Chiara, I learned so many things from you, you helped me starting a whole new life here and supported me during the adaptation time, I will never forget all the beautiful moments together, the complaints, the laughs, and the stupid things done at home. Mario, thanks for making my life lighter and brighter with your amazing dishes and with Ana Mena and Baby-K feat Chiara Ferragni songs. To Ale, thank you for helping me understanding that Calcutta was better than Coez and for all the fun and discussion about music and videogames. Love the time spent together with you and Kaie. Thank you kaie for taking part to this adventure.

To Roberto, my cell culture friend. How many cells we split together and if the cell culture room could speak would say that we complain a little bit too much. I wish you all the best! To the Dr. Nickel and his group, Sabine, Hans-Michael and all the others thank you for being always so nice to me and making me feel like I was a group member.

Thank you very much to all of you!